Dissertation
submitted to the
Combined Faculties for the Natural Sciences and for Mathematics
of the Ruperto-Carola University of Heidelberg, Germany
for the degree of
Doctor of Natural Sciences

presented by
Diplom-Physiker Heinz Tilsner
born in Mosbach

Oral examination: 12.06.2002

Two-Particle Correlations at 40, 80, and 158 *A*GeV Pb-Au Collisions

Referees: Prof. Dr. Johanna Stachel
Prof. Dr. Karl-Tasso Knöpfle

Two-Particle Correlations at 40, 80, and 158 *A*GeV Pb-Au Collisions

In this thesis, a centrality dependent study of two-particle momentum correlations of like-sign pions (HBT interferometry) from Pb-Au collisions at beam energies of 40, 80, and 158 *A*GeV is presented. The three-dimensional correlation function C_2, depending on the relative momentum components of the particle pair, was parameterized using a three-dimensional Gaussian, modified to consider the final state Coulomb repulsion. The parameterization was done in the Cartesian *out-side-long* system as proposed by G. Bertsch and S. Pratt. A differential analysis of the HBT radius parameters as a function of the mean transverse pair momentum $k_\perp$ allowed to determine transverse geometrical source sizes of about 5.5 fm to 7 fm, increasing with energy and centrality. The mean transverse flow velocity $\langle v_\perp \rangle$ was found to be of the order 0.5–0.6c. For the freeze-out time τ_f values between 6 and 8 fm/c were obtained with a duration of particle emission compatible with zero. The beam energy dependence of the HBT radii provide evidence for a universal pion freeze-out condition.
The analyzed data have been recorded with the CERES spectrometer at the Super Proton Synchrotron (SPS) accelerator at CERN. In 1998 the spectrometer was upgraded by a cylindrical Time Projection Chamber (TPC) which improved substantially the hadron detection capability of the spectrometer and allowed for a systematic investigation of hadronic observables at midrapidity. The first part of this thesis describes the readout system of the TPC and its modification for the beam time in 2000.

Zwei-Teilchen Korrelationen bei 40, 80 und 158 *A*GeV Pb-Au Kollisionen

In der vorliegenden Arbeit wird eine zentralitätsabhängige Untersuchung von Zwei-Teilchen Korrelationen gleichgeladener Pionen (HBT Interferometrie) in Pb-Au Kollisionen bei Energien von 40, 80 und 158 *A*GeV vorgestellt. Die dreidimensionale Korrelationsfunktion C_2, die von den Komponenten des Relativimpulses beider Teilchen abhängt, wurde mit Hilfe einer dreidimensionalen modifizierten Gauss-Funktion parametrisiert. Die Modifikation berücksichtigt die Coulomb-Wechselwirkung im Endzustand. Die Parametrisierung der Korrelationsfunktion erfolgte im *out-side-long*-System, welches von G. Bertsch und S. Pratt vorgeschlagen wurde. Eine differentielle Analyse der HBT Radiusparameter als Funktion des mittleren transversalen Paarimpulses $k_\perp$ liefert transversale geometrische Quellgrößen von 5.5 bis 7 fm. Als mittlere transversale Flußgeschwindigkeit $\langle v_\perp \rangle$ wurden Werte zwischen 0.5–0.6c bestimmt. Für die Ausfrierzeit τ_f wurden Werte zwischen 6 und 8 fm/c ermittelt, mit einer mit Null verträglichen Dauer der Teilchenemission. Die beobachtete Abhängigkeit der HBT Radien von der Strahlenergie liefert Hinweise auf eine universelle Ausfrierbedingung für Pionen.
Die analysierten Daten wurden mit Hilfe des CERES Spektrometers am Super Proton Synchrotron (SPS) am CERN aufgezeichnet. 1998 wurde das bestehende Spektrometer um eine zylindrische Spurendriftkammer (TPC) ergänzt, welche die Sensitivität für Hadronen wesentlich verbesserte und eine systematische Untersuchung hadronischer Observablen bei Midrapidität ermmöglicht. Im ersten Teil der Arbeit wird das Auslesesystem der TPC sowie die für die Strahlzeit des Jahres 2000 durchgeführten Änderungen beschrieben.

Contents

List of Figures

List of Tables

1 Ultrarelativistic Heavy Ion Collisions

The aim of colliding heavy ions at ultrarelativistic energies is the examination of properties of strongly interacting matter at high energy densities. If nuclear matter is heated and compressed, resulting in high energy densities ε, lattice quantum chromodynamic (QCD) calculations predict a phase transition from hadronic matter to a new state of matter: the Quark Gluon Plasma (QGP). In the quark gluon plasma the confinement of quarks and gluons is repealed, leading to *quasi-free* particles. In February 2000, CERN[1] announced officially the formation of a new state of matter [1], resembling in many ways the expected QGP. In the light of thermodynamics, beyond the phase transition the hadronic degrees of freedom of the system are replaced by those of quarks and gluons (which are many more in the latter compared to the hadronic system), leading to a characteristic strong increase in the energy density of the system within a small interval around the critical temperature T_c. Key questions of these studies are the restoration of chiral symmetry which is spontaneously broken in the QCD ground state, the dynamical evolution of the phase transition, or of which order the transition is.

The study of the quark gluon plasma also has impact on astrophysics and cosmology. The conditions of a heavy ion collision at ultrarelativistic energies are in some aspects very similar to those of the universe at a very early stage, where up to a few tens of microseconds after the *Big Bang* a transient phase of strongly interacting matter existed at temperatures above 10^{12} K and low net-baryon density. Collisions of atomic nuclei at energies up to a few tens of MeV per nucleon lead to the other extreme of low temperatures and high baryon densities. These conditions are closer to those occuring in the interior of neutron stars [2, 3, 4], where mass densities are likely to exceed 10^{18} kg/m^3 which is about four times the density of nuclei.

1.1 Hot and Dense Nuclear Matter

In 1964, Gell-Mann and Zweig introduced the quark model to explain the regularities among the hundreds of baryon and meson states known at that time. They assumed that all hadrons were built from u, d, and s quarks. In this model, mesons are composed of a quark and an anti-quark ($q\bar{q}$) while baryons are built up of three quarks (qqq). The physics of strong interaction, responsible for the binding of quarks into hadrons, is described by the theory of quantum chromodynamics.

Quarks are fermions (spin $1/2$), characterized by their *flavor*. These are u (up), d (down), c (charm), s (strange), b (bottom), and t (top). The interaction between quarks depends on the so-called *color* of the quarks which is the QCD analog to the electric charge. There are three different colors a quark can carry: *red*, *blue*, and *green*. The interaction between quarks is mediated by the exchange of *gluons*. The gluons are the field quanta of the strong interaction and carry also color

[1] European Organization for Nuclear Research

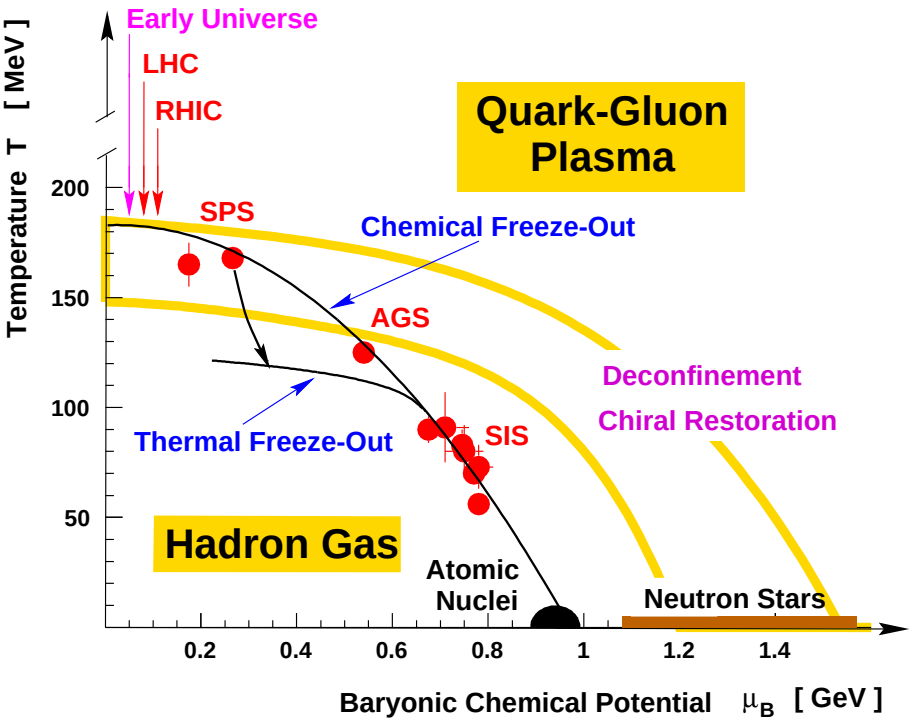

Figure 1.1: QCD phase diagram of hadronic matter [5].

charge. All experimentally observable hadrons are so-called *color-singlets*, objects with the color *white*. These white objects can be constructed by either combining three different colors or a color with its anti-color. For the same reason, color carrying single quarks can not be observed as free particles. The coupling constant α_s of QCD, describing the strength of the interaction, depends on the distance[2] between two quarks. At very small distance (large Q^2) between the quarks the coupling constant is small, approaching zero for $Q^2 \to \infty$ (*asymptotic freedom*). At large distances, the coupling constant strongly increases. With the attempt to separate two quarks the potential between them increases, leading to the creation of additional quarks and gluons which combine to hadrons (*confinement*).

The phase diagram of strongly interacting matter is shown in Figure 1.1 [5, 6, 7]. It shows a transition from a gas of hadronic resonances at low energy densities to a quark gluon plasma (QGP) at high energy densities. The critical energy density ε_c is of the order of 1 GeV/fm^3 and was derived by lattice QCD calculations. The critical energy density can be reached either by creating matter with zero net-baryon density and a temperature of about $T_c \approx 170$ MeV [8], or by compressing cold nuclear matter to baryon densities of about $\rho_c \approx 3-10\,\rho_0$, where $\rho_0 = 0.15\,\text{fm}^{-3}$ is the ground state density of nuclear matter. In heavy ion collisions a combination of heating and compressing is employed in order to reach the critical energy density. Depending on the energy of the colliding nuclei different regions of the phase diagram can be explored. At lower beam energies (e. g. SIS[3] with beam kinetic energies in the vicinity of ≈ 1 *A*GeV), the nuclei

[2] To be more precise, α_s depends on the invariant 4-momentum transfer Q^2 between two quarks.
[3] **S**chwer**I**onen **S**ynchrotron at GSI, Darmstadt

are stopped, leading to baryon rich matter in the collision region. The nuclear matter is only moderately heated and compressed. At higher beam energies the temperatures reached are much higher and the collisions become more transparent, resulting in a baryon free QGP. An overview of the experimental mapping of the QCD phase diagram can be found in [6, 7].

The knowledge about the QCD phase diagram along the temperature axis at $\mu_B = 0$ is based on lattice QCD calculations [9, 10, 11]. For two quark flavors they predict a critical temperature $T_c = (171 \pm 4)$ MeV [8]. For non-zero baryon density, results are based on models which interpolate between low-density hadronic matter and high density quark gluon plasma. Near T_c, the energy density in units of T^4 changes significantly within a narrow temperature interval (see Figure 1.2). The values according to the law of Stefan-Boltzmann for an ideal gas of non-interacting quarks and gluons are indicated at the right edge of the figure. Around T_c the formation of the

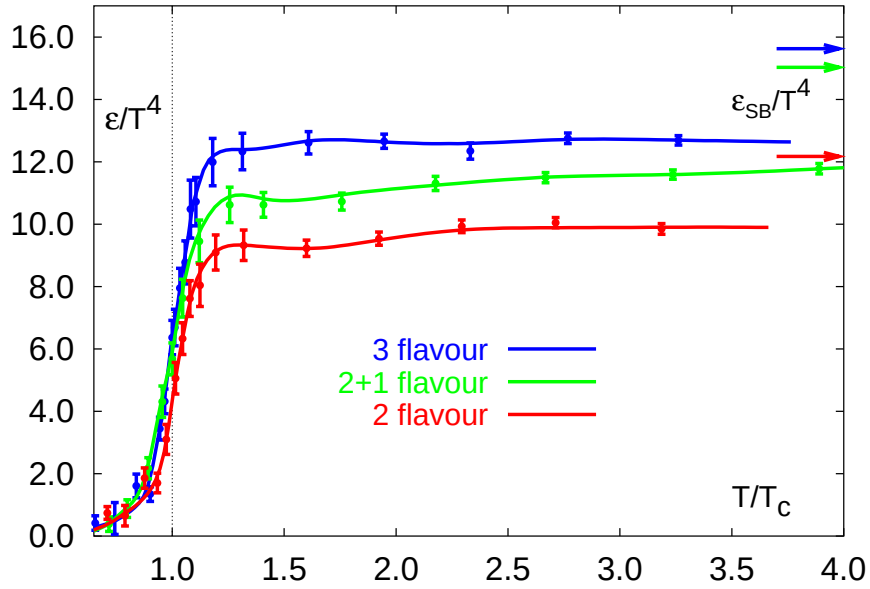

Figure 1.2: Result of lattice QCD calculations for the energy density ε (in units of T^4) as a function of the temperature T (in units of the critical temperature T_c). Here ε is shown for different numbers of quark flavors where $2+1$ means two light and one heavy flavors (Figure from [11]).

QGP happens. The confinement of quarks and gluons into hadrons is broken, and the approximate chiral symmetry of QCD, which is spontaneously broken at low temperatures and densities, is expected to be restored. This is found in lattice QCD calculations by inspecting the order parameter $\langle\bar{\Psi}\Psi\rangle$, the expectation value of the so-called chiral condensate. This order parameter characterizes the chiral phase transition and vanishes in the chiral symmetric phase but becomes finite in the asymmetric phase corresponding to a mixing of left- and right-handed quarks in the ground state. Chiral symmetry is a consequence of the standard model which postulates left and right handed degenerated doublets of particles. The small current quark masses lead to a small breaking of this symmetry. This approximate symmetry is broken spontaneously in a mechanism giving large masses (constituent masses) to the quarks. The (approximate) restoration of chiral symmetry

in the QGP means that the constituent masses of quarks are significantly reduced to the scale of the current quark masses.

The search for the QGP is complicated by the very short lifetime of the fireball of heated and compressed matter, created in the collision. Apart from measurements of photons and leptons, all experimental results characterize only the hadronic state at the end of the dynamical evolution (at *freeze-out*) of the collision system. Therefore, only a combination of many experimental signatures allows for a conclusion whether the QGP was created or not.

1.2 Space-Time Evolution of a Heavy Ion Collision

The space-time evolution of a heavy ion collision depends on the initial conditions of the reaction, e. g. the energy density deposited in the reaction zone. With the assumption of local thermal equilibrium the expansion of the fireball can be calculated using hydrodynamical models. In the hydrodynamical description, the complete dynamics of the system is described by the energy density ε, the pressure field p, the temperature field T, and the 4-velocity field $u^\mu = \mathrm{d}x/\mathrm{d}\tau$ at different space-time points as the system evolves. The energy density, the pressure, and the temperature are related by the equation of state $\varepsilon = \varepsilon(p,T)$. The pressure inside the hot and dense medium leads to an expansion of the system while its density and temperature are decreasing. Having reached a certain density/temperature[4], first all inelastic interactions between the system's constituents cease and the abundancies of hadrons are fixed (*chemical freeze-out*). With further decreasing density/temperature also the elastic interactions vanish and the *thermal freeze-out* happens. At this time, the phase space population of the final state is determined.

Another condition which determines the space-time evolution of the system is the fraction of longitudinal energy still present in the final state after the collision. At collision energies in the AGS[5] domain the *nuclear stopping power* is quite large. This term, introduced in high-energy nucleus-nucleus collisions by Busza and Goldhaber [12], describes the degree of stopping an incident nucleon suffers when it impinges on the nuclear matter of another nucleus. In collision systems created by the complete stopping of the nuclei the collective expansion is determined by the pressure and the energy density only (Landau picture). On the other hand, at typical SPS[6] energies of about $\sqrt{s} \approx 20$ GeV per nucleon pair, the collision of two nuclei is significantly transparent and about half of the initially longitudinal motion is preserved after the collision. Compared to collisions with full stopping, this inherent longitudinal expansion influences the system's evolution and must be considered in the calculations. This scenario of colliding nuclei with ultrarelativistic energies was first described by Bjorken [13] and is depicted in Figure 1.3. In the center of mass system, nucleus A approaches from $z = -\infty$ with a velocity close to the speed of light and meets nucleus B which comes from $z = +\infty$, also with a velocity close to the speed of light. At the point $(z,t) = (0,0)$ they meet and collisions between the nucleons of both nuclei take place. Due to the Lorentz contraction in longitudinal direction the nuclei are represented as thin discs.

The dynamics of this process is pictured in Figure 1.4, showing a space-time diagram with the longitudinal coordinate z and the time coordinate t. Due to the transparency of the collision, the

[4] A priori it is not obvious what the freeze-out condition is. In hydrodynamical calculations usually a freeze-out temperature T_f is imposed by hand.

[5] **A**lternating **G**radient **S**ynchrotron, a heavy ion accelerator at the Brookhaven National Laboratory

[6] **S**uper **P**roton **S**ynchrotron at CERN

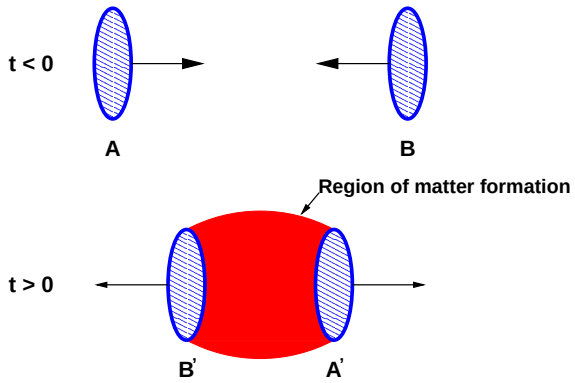

Figure 1.3: Schematic representation of an ultrarelativistic nucleus-nucleus collision in Bjorken's description. Due to the Lorentz contraction in longitudinal direction the colliding nuclei are reduced to thin disks.

two nuclei move away from the collision region, depositing a large amount of energy in a small region around $z = 0$ in a short duration of time. Even though the energy density of the created matter is very high, its net-baryon content is small. Shortly after the collision at $(z,t) = (0,0)$, the energy density of the system may be high enough to form the quark gluon plasma in the central collision region. Although the plasma may initially not be in thermal equilibrium, it will be equilibrated at proper time τ_0. The type of quark gluon plasma which may be created in such a reaction is comparable to the one which was created in the *Big Bang*, albeit of much smaller energy content and therefore lifetime, and hence of special astrophysical interest [13, 14]. From there on the plasma evolves according to the laws of hydrodynamics. During the expansion of the plasma its temperature drops and hadronization will take place. The hadrons stream out of the collision region and at time τ_f the *freeze-out* happens.

The hadronic final state of the evolving system is accessible by experiments. It is characterized by the abundancies and the momentum distributions of the detected particles. Because the momentum distribution of the created particles is considered to be symmetric in ϕ (which is actually only true for central collisions with impact parameter $\vec{b} = 0$) it is customary to divide the momentum into a component p_{long} parallel to the beam axis (z-axis) and a component perpendicular to it:

$$p_{\text{long}} = p_z, \tag{1.1}$$

$$p_\perp = \sqrt{p_x^2 + p_y^2}. \tag{1.2}$$

Another useful variable commonly used to describe the kinematics of a particle is the rapidity y which is defined in terms of its energy and momentum components by

$$y = \frac{1}{2}\ln\left(\frac{E + p_z}{E - p_z}\right). \tag{1.3}$$

In the nonrelativistic limit, the rapidity of a particle traveling in longitudinal direction is equal to the velocity of the particle in units of the speed of light. The 4-momentum of a free particle which is on the mass shell has only three degrees of freedom, thus can be represented by $(y, p_\perp)$. The

transformation between $(E, \vec{p})$ and $(y, \vec{p}_\perp)$ is given by

$$E = m_\perp \cosh(y), \tag{1.4}$$
$$p_z = m_\perp \sinh(y), \tag{1.5}$$

with $m_\perp$ being the transverse mass of the particle:

$$m_\perp = \sqrt{m_0^2 + p_\perp^2}, \qquad p_\perp^2 = p_x^2 + p_y^2. \tag{1.6}$$

Additional information about the reaction can be gathered from two-particle correlations, the main topic of this thesis. Suitable observables to characterize the dynamics of a pair of particles are the pair rapidity $y_{\pi\pi}$ and the mean transverse momentum $\vec{k}_\perp$. They are defined by

$$y_{\pi\pi} = \frac{1}{2} \ln\left(\frac{E_1 + E_2 + p_{1,z} + p_{2,z}}{E_1 + E_2 - p_{1,z} - p_{2,z}} \right) \tag{1.7}$$

and

$$\vec{k}_\perp = \frac{1}{2}\left(\vec{p}_{1,\perp} + \vec{p}_{2,\perp}\right). \tag{1.8}$$

Another important value is the Lorentz invariant 4-momentum difference of the particles

$$q_{\text{inv}} = \sqrt{(\mathbf{p}_1 - \mathbf{p}_2)^2} = \sqrt{(E_1 - E_2)^2 - (\vec{p}_1 - \vec{p}_2)^2}, \tag{1.9}$$

which is the relative momentum of the particle pair in its center of mass system. Here and in the following 4-vectors are denoted by bold symbols.

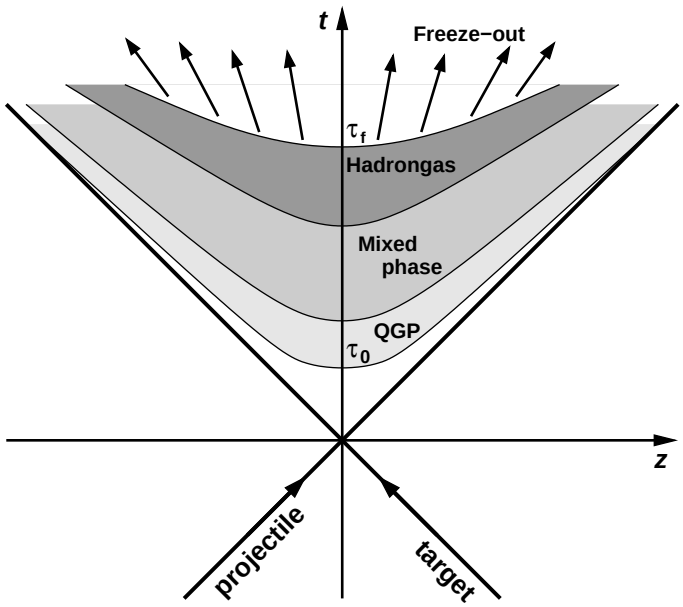

Figure 1.4: Evolution of a heavy ion collisions in Minkowski's representation of space-time.

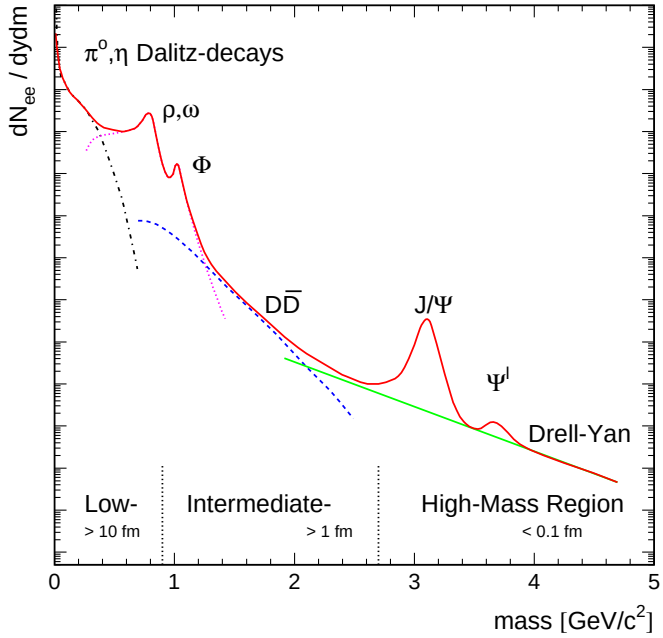

Figure 1.5: Schematic dilepton mass spectrum.

1.3 Physics Program of CERES

CERES is a dilepton experiment at the CERN SPS, devoted chiefly to the systematic study of low mass e^+e^- pairs ($0.1 < m_{e^+e^-} < 1.5$ GeV$/c^2$) produced in nucleon-nucleon, nucleon-nucleus, and nucleus-nucleus collisions. Dileptons are a particularly attractive observable. In contrast to hadrons they interact with other particles in the collision zone only through the electromagnetic interaction. They are produced in all stages of the collision and emitted instantaneously after creation without significant further interaction. Due to the negligible final state interactions of leptons they carry information about the complete evolution of the fireball essentially unaffected to the detectors. In this way, they probe even the innermost zones of the fireball which are formed in the early stages of the collision.

The production rate and the momentum distribution of the produced leptons depend on the momentum distribution of the quarks and anti-quarks in the plasma, which is given by the thermodynamic condition in the plasma, and on decays of produced hadrons. Thus, lepton pairs carry information about the thermodynamic state of the medium at the moment of their production. The schematic dilepton mass spectrum shown in Figure 1.5 indicates the major dilepton sources in ultrarelativistic heavy ion collisions. In the low-mass region the dilepton spectrum is dominated by the decays of light vector mesons ρ, ω and ϕ. The ρ is of particular interest because of its lifetime of 1.3 fm/c, which is short compared to the lifetime of the fireball. Its decay samples the hot and dense medium and the fireball's evolution as a function of time. Its in-medium behavior around the critical temperature T_c for deconfinement could therefore reflect the associated restoration of chiral symmetry. For a discussion about how this restoration of chiral symmetry is linked to the

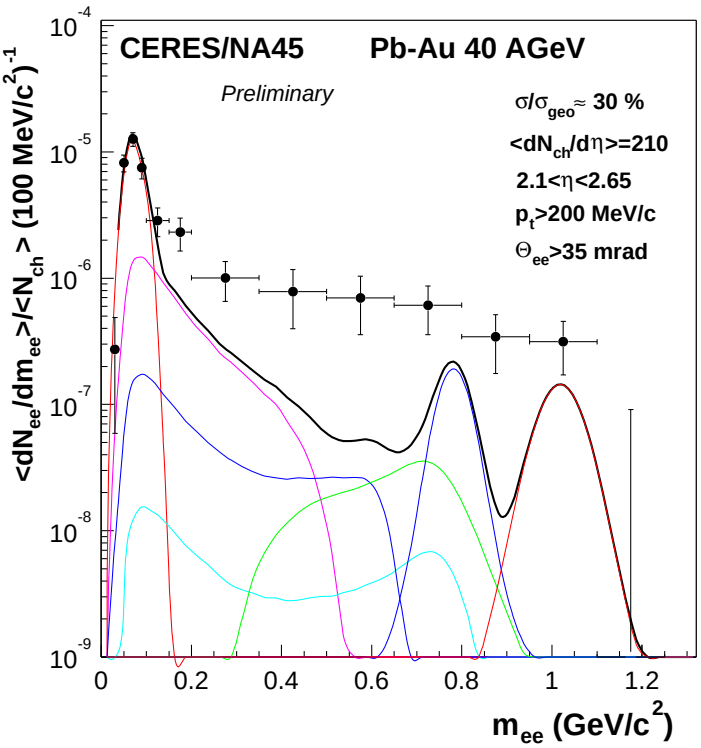

Figure 1.6: Invariant mass spectrum of e^+e^- pairs recorded in central Pb-Au collisions at 40 *A*GeV.

masses of vector mesons see e. g. [15, 16, 17].

CERES observed an enhanced production of low-mass dielectron pairs in S-Au and Pb-Au collisions at full SPS energies of 200 and 158 *A*GeV respectively [18, 19, 20]. The observed dielectron yield significantly exceeds the expectations extrapolated from p-nucleon and p-nucleus collisions. There, the measured electron pair distribution agreed well with the one expected from hadron decays in vacuum [21]. The simulation of the dielectron contribution from hadron decays, the so-called *hadronic cocktail*, is based on the knowledge of the branching ratios of all relevant leptonic and semi-leptonic decays and the total production cross section of neutral mesons measured in p-nucleon collisions. Figure 1.6 shows the most recent dielectron spectrum, measured at 40 *A*GeV Pb-Au collisions in 1999 [22]. While the $\pi^0 \rightarrow e^+e^-\gamma$ Dalitz peak is well reproduced by the hadronic cocktail, the data show a strong enhancement by a factor of 5.1 ± 1.3 at $m_{ee} > 0.2$ GeV/c^2. Theoretical explanations of the observed enhancement refers to direct radiation from the fireball, dominated by pion annihilation $\pi^+\pi^- \rightarrow \rho \rightarrow e^+e^-$. However, the shape of the enhancement is not consistent with the spectral shape of the ρ meson. To describe the data, a strong medium modification of the intermediate ρ is necessary. The two most prominent theoretical approaches predict a shift of the ρ peak to lower masses (Brown-Rho scaling [23]) or a calculation of the ρ spectral density within the dense hadronic medium [17, 24] resulting in a broadened peak. Alternatively, the experimental spectrum can be described equally well in terms

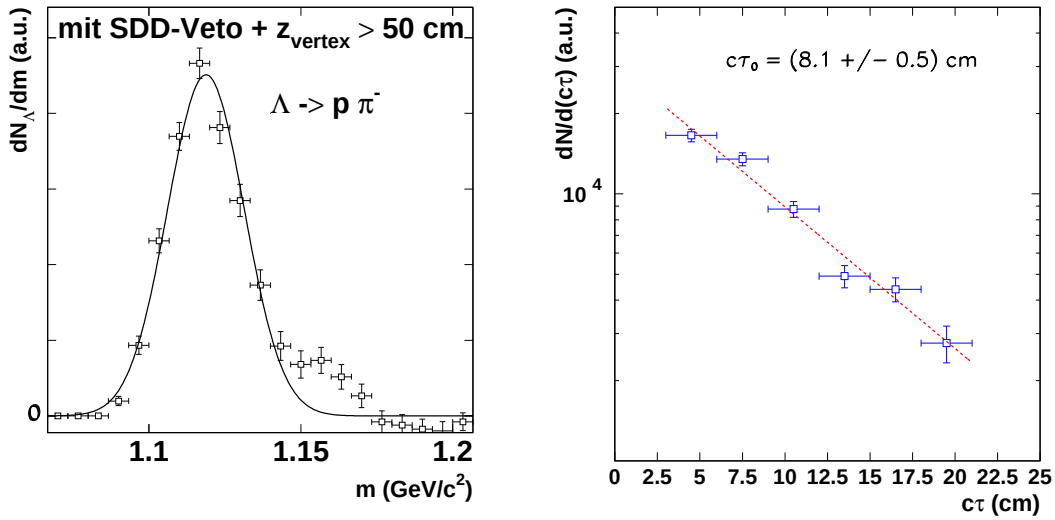

Figure 1.7: The reconstructed mass and lifetime of the Λ hyperon at a beam energy of 40 *A*GeV. Figures are from [25].

of partonic degrees of freedom, i. e. in-medium $q\bar{q}$ annihilation [17].

With the installation of the TPC (**T**ime **P**rojection **C**hamber) during the year 1998 the physics capabilities of CERES were also largely expanded for the analysis of hadrons. The primary goal of this upgrade was to improve the mass resolution to $\Delta m/m \approx 2\%$ in the $\rho/\omega/\phi$-mass region. With this resolution possible mass shifts or changes in width of the vector mesons ρ, ω, and ϕ can be observed directly along with a simultaneous measurement of the continuum. Using the data recorded during the beam time in 1999 at a beam energy of 40 *A*GeV, the reconstruction of strange particles (Λ, $\bar{\Lambda}$, and K^0_s) was possible [25]. By combining positive with negative charge tracks and assuming for them to be protons respectively π^-, decays of the electrical neutral Λ hyperon have been reconstructed. The reconstructed mass and lifetime are shown in Figure 1.7. They agree with the values given in [26]. However, the width of the mass peak is larger compared to results from Monte-Carlo simulations of the detector. The reason for this is the by that time unfinished calibration of the TPC. Details about the analysis can be found in [25].

The topic of this thesis are Bose-Einstein correlations of identical pions. This method, also called HBT-interferometry after Hanbury-Brown and Twiss who invented it in the early fifties of the last century [27, 28, 29], provides direct information about the space-time structure of the particle emitting source, created in heavy ion collisions, analyzing the relative momentum distribution of emitted particle pairs. A differential HBT analysis in terms of transverse momentum components of the particle pair reveals insight into the dynamical properties of the source at freeze-out, providing for example information about the life-time, the duration of particle emission, or the transverse expansion velocity of the source. This information is necessary, for example, for models which try to simulate the dilepton spectra measured by CERES. For these calculations the knowledge of the full space-time evolution is crucial and the HBT results can be used to tune these models.

2 Intensity Interferometry

2.1 Introduction

The goal of ultra-relativistic nucleus-nucleus collisions is the creation and characterization of the quark-gluon plasma. But the question whether such a plasma was created during a collision is not easy to answer. The reason for this is the confinement of quarks and gluons into color-neutral particles. Only very few particle species, mainly leptons, can provide direct information about the initial partonic stage of the collision. The much more abundant hadrons are substantially affected by secondary interactions and decouple from the collision region only during the final thermal *freeze-out* stage. A complete understanding of the space-time structure and dynamical state of the reaction zone at *freeze-out* can give an answer to the question whether a plasma phase was formed or not. Determining the size and lifetime of the state at decoupling together with the expansion velocity should allow for a back-extrapolation in time of the energy density to a point of vanishing transverse expansion. The most comprehensive way to obtain experimental information on the space-time structure of a particle emitting source created in relativistic heavy ion collisions is through two-particle intensity interferometry. The method, also named HBT-interferometry after Robert Hanbury-Brown and Richard Twiss who invented it, uses the quantum statistical momentum correlations between pairs of identical particles to extract the space-time structure of the source.

HBT intensity interferometry was used for the first time by the radio astronomers Robert Hanbury-Brown and Richard Twiss [28, 29]. In 1950 they invented the technique to measure the diameter of the sun, using two radio telescopes operating at 2.4 m wavelength, and examined in 1956 radio wave sources in the galaxies Cassiopeia and Cygnus [27], and subsequently applied the method to a measurement of the angular diameter of Sirius [29]. In [28] they demonstrated that photons in an apparently uncorrelated thermal beam tend to be detected in close-by pairs. This photon bunching or HBT-effect, first explained theoretically by Purcell [30], is one of the key experiments of quantum optics [31].

In particle physics the HBT-effect was independently discovered by G. Goldhaber, S. Goldhaber, W. Y. Lee, and A. Pais [32]. It is known as the *GGLP-effect*. In 1960, they studied the angular correlations between pions in $p\bar{p}$-annihilations and observed an enhancement of like-sign pion pairs at small relative momenta compared to unlike-sign pairs. The results could be explained only by considering the symmetrization of the wavefunction of the particle pair and the finite spatial extension of the decaying $p\bar{p}$ system. Measuring the correlation function as a function of the momentum difference reveals information about the spatial extension of the particle emitting source.

The difference between *intensity* interferometry and conventional *amplitude* interferometry can be illustrated using Figure 2.1. In *amplitude* interferometry each detectors could be a slit

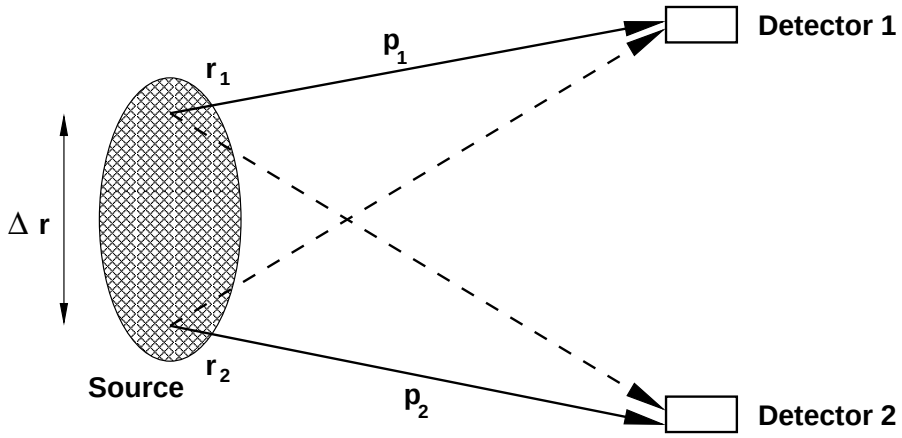

Figure 2.1: Schematic representation of the emission of two indistinguishable particles from two points $\vec{r}_1$ and $\vec{r}_2$ of the source. The momenta of the two particles are measured with two detectors.

through which the emitted particles pass. To use a traditional example, the particles could produce an interference pattern on a screen located behind the slits. The interference pattern depends on the relative phase of the particles' amplitudes measured at the two detectors. In *intensity* interferometry a correlation function C is constructed from the number of counts n_1 and n_2 measured in the detectors:

$$C = \frac{< n_{12} >}{< n_1 >< n_2 >} - 1, \tag{2.1}$$

where n_{12} denotes the number of counts in which particles are observed in detector 1 *and* detector 2. The correlation function is proportional to the intensity, i. e. the complex square of the amplitude of the particles at both detectors.

The origin of the observed particle correlations is the symmetry of the quantum mechanical wave function of identical bosons. A very simplified and descriptive argument given in [33] is based on the situation depicted in Figure 2.1. A spherical source emits a pair of identical particles from point $\vec{r}_1$ with momentum $\vec{p}_1$ and from point $\vec{r}_2$ with momentum $\vec{r}_2$. If these points are well separated in phase-space and the Heisenberg uncertainty relation

$$(x_1^i - x_2^i)(p_1^i - p_2^i) \geq \frac{\hbar}{2\pi}, \qquad i = 1,2,3 \tag{2.2}$$

is satisfied this process can be treated classically. But as soon as the particles are close to each other and

$$(x_1^i - x_2^i)(p_1^i - p_2^i) < \frac{\hbar}{2\pi}, \qquad i = 1,2,3 \tag{2.3}$$

becomes valid a quantum mechanical description becomes necessary. The quantum mechanical treatment needs to ensure the (anti-)symmetrization of the two-particle wavefunction which leads to vanishing probability for the emission of two identical fermions from the same space point while it leads to an enhanced probability for bosons to be found at the same point in phase-space compared to the classical expectation. Due to the finite extension of the source the distance of the two particles in coordinate space $(x_1^i - x_2^i)$ is limited. By measuring particle pairs with smaller

and smaller relative momentum $\vec{p}_1 - \vec{p}_2$ the system can be forced into the quantum domain. Once $q_i = p_1^i - p_2^i$ becomes smaller than $\hbar/(2\pi R)$ the particles have to be treated according to quantum mechanics and their emission probability will be affected by wavefunction symmetrization. The result is an enhanced pair emission probability for bosons compared to the classical expectation and a reduced probability for fermions. Thus, for relative momenta $q < q^* \simeq \hbar/(2\pi R)$ a significant deviation from unity of the two-particle correlation function is expected. The value q^* at which this effect sets in is a measure for the geometric radius R of the source. Unfortunately, this naive picture only works for photon interferometry of stars for which the method was invented. The basic reason for the failure of this simplified model in high energy heavy ion collisions is that the sources created in such collisions live only for a finite time and have an inhomogeneous temperature profile and strong collective dynamical expansion (*hydrodynamical flow*). For such sources the HBT radius parameters, synonymous with the half-width of the correlation functions, only measure the so-called *space-time regions of homogeneity* (or *length of homogeneity*) rather than the full source size. Inside the regions of homogeneity variations of the momentum distribution are small enough to allow quantum statistical correlations.

The homogeneity length varies with the momentum of the emitted particles. This leads to an important dependence of the HBT parameters on the pair momentum which can be used to extract the strength of the collective flow of the source at freeze-out.

2.2 Particle Correlations from Phase-Space Distributions

2.2.1 The Two-particle Correlation Function

HBT-interferometry is based on the principle that it is not possible in quantum mechanics to distinguish identical particles. The probability density of a two-particle system has to be the same for the interchange of the particles:

$$|\Psi_{1,2}|^2 = |\Psi_{2,1}|^2. \tag{2.4}$$

The probability to detect two particles with momenta $\vec{p}_1$ and $\vec{p}_2$, emitted by a particle source at positions $\vec{r}_1$ and $\vec{r}_2$ and detected at positions $\vec{x}_1$ and $\vec{x}_2$, must be independent of which of the both particle was actually emitted at position $\vec{r}_1$ or position $\vec{r}_2$ — it is impossible to decide by measurement which particle was emitted at position $\vec{r}_1$ or $\vec{r}_2$ (see Fig. 2.1). To fulfill this condition, the two-particle wavefunction has to be a linear combination of the single-particle wavefunction. These combinations can be done in two ways:

$$\Psi_{1,2} = \frac{1}{\sqrt{2}}\big(\Psi_1(\vec{r}_1)\Psi_2(\vec{r}_2) + \Psi_1(\vec{r}_2)\Psi_2(\vec{r}_1)\big) = \Psi_{2,1} \qquad \textit{symmetric} \tag{2.5}$$

$$\Psi_{1,2} = \frac{1}{\sqrt{2}}\big(\Psi_1(\vec{r}_1)\Psi_2(\vec{r}_2) - \Psi_1(\vec{r}_2)\Psi_2(\vec{r}_1)\big) = -\Psi_{2,1} \qquad \textit{anti-symmetric} \tag{2.6}$$

For a system of bosons the combined wavefunction has to be *symmetric*.

With the assumption of plane waves ($\Psi \propto \exp(\frac{i}{\hbar}(\vec{p}\cdot\vec{r} - Et))$ for Ψ_1 and Ψ_2 the probability density is given by:

$$|\Psi_{1,2}|^2 = |\Psi_{2,1}|^2 = 1 + \cos(\Delta p \Delta r) \tag{2.7}$$

with $\Delta p = |\vec{p}_1 - \vec{p}_2| = q$ and $\Delta r = |\vec{r}_1 - \vec{r}_2|$.

The probability to detect two bosons with momenta $\vec{p}_1$ and $\vec{p}_2$ is given by the integration of the probability density (2.7) over the emission function $S(\mathbf{r},\mathbf{p})$ (see Subsection 2.2.2) which in general is a function of the emission position in space-time $\mathbf{x}$ and the 4-momentum $\mathbf{p}$ of the emitted particle:

$$P_2(\vec{p}_1,\vec{p}_2) = \int S(\mathbf{r}_1,\mathbf{p}_1)S(\mathbf{r}_2,\mathbf{p}_2)\big(1+\cos(\Delta r\Delta p)\big)\,\mathrm{d}^4r_1\mathrm{d}^4r_2. \tag{2.8}$$

The single-particle probability $P_1(\vec{p})$ is given by:

$$P_1(\vec{p}) = \int S(\mathbf{r},\mathbf{p})\,\mathrm{d}^4r. \tag{2.9}$$

A measure for the correlation of pions with small difference in momentum is the correlation function C_2 which is defined as the ratio of two-particle and single-particle probabilities:

$$C_2(\vec{p}_1,\vec{p}_2) = \frac{P_2(\vec{p}_1,\vec{p}_2)}{P_1(\vec{p}_1)P_1(\vec{p}_2)}. \tag{2.10}$$

The value of the correlation function is 1 for big invariant momentum differences $q = |\vec{p}_1 - \vec{p}_2|$ and reaches 2 in the limit $q \to 0$. This is a direct result of the Bose-Einstein statistics. The region in which the correlation function is bigger than 1 determines the region in which the wave functions of the particles overlap, i. e. where $\Delta p\Delta r \leq \hbar/2\pi$. In this region it is impossible to distinguish the two particles.

The measurement of the correlation function C_2 contains information about the spatial as well as the temporal structure of the particle emitting source. For the simplest example of a static particle emitting source the momenta of the emitted particles are independent of the emission position within the source. The emission function $S(\mathbf{r},\mathbf{p})$ factorizes into a part depending on the momentum only and a part depending on the position where the emission happens. It can be written as $S(\mathbf{r},\mathbf{p}) = f(\mathbf{p})\rho(\mathbf{r})$. For this case the correlation function is given by

$$C_2(\vec{p}_1,\vec{p}_2) = C_2(q) = 1 + |\tilde{\rho}(q)|^2, \tag{2.11}$$

where

$$\tilde{\rho}(q) = \int \exp(i(\mathbf{p}_1-\mathbf{p}_2)\mathbf{r})\rho(\mathbf{r})\,\mathrm{d}^4r \tag{2.12}$$

is the Fourier transformation of the spatial emission function $\rho(\mathbf{r})$. For the simplest parameterization of the emission function with a Gaussian function

$$\rho(\vec{r},t) = \frac{1}{\pi^2R^3\tau}\exp\big(-\frac{\vec{r}^2}{2R^2} - \frac{t^2}{2\tau^2}\big), \tag{2.13}$$

also the correlation function is described by a Gaussian [34]:

$$C_2(q) = 1 + \exp(-\vec{q}^2R^2 - q_0^2\tau^2). \tag{2.14}$$

The difference in momentum of the two particles is given by $\vec{q}$ and R and τ are the spatial and temporal widths of the Gaussian emission function.

2.2.2 The Emission Function $S(\mathbf{x},\mathbf{p})$

The emission function $S(\mathbf{x},\mathbf{p})$ can be identified with the Wigner transform of the density matrix associated with the classical source amplitudes $J(\mathbf{x})$ (see e.g. [33]). This Wigner density is a quantum mechanical object defined in phase-space $(\mathbf{x},\mathbf{p})$. In general, it is neither positive definite nor real. But, when integrated over $\mathbf{x}$ or $\mathbf{p}$ it yields the classical source density in momentum or coordinate space. Thus, the emission function $S(\mathbf{x},\mathbf{p})$ is the quantum mechanical analogue of the classical phase-space distribution which gives the probability of finding at space-time point $\mathbf{x}$ a source which emits free pions with 4-momentum $\mathbf{p}$.

The relation between the single-particle Wigner phase-space density $S(\mathbf{x},\mathbf{p})$ of the particle emitting source, the invariant single-particle spectrum $E\mathrm{d}N/\mathrm{d}^3p$, and the two-particle correlation function $C_2(\vec{q},\vec{K})$ for pairs of identical bosons is given by [33]:

$$P_1(\vec{p}) = E\frac{\mathrm{d}N}{\mathrm{d}^3p} = \int S(\mathbf{x},\mathbf{p})\,\mathrm{d}^4x, \tag{2.15}$$

$$C(\vec{q},\vec{K}) \approx 1+\left|\frac{\int e^{iqx}S(\mathbf{x},\mathbf{K})\,\mathrm{d}^4x}{\int S(\mathbf{x},\mathbf{K})\,\mathrm{d}^4x}\right|^2. \tag{2.16}$$

In the two-particle correlation function (2.16) the relative momentum $\mathbf{q}$ and the average pair momentum $\mathbf{K}$ are defined as

$$\mathbf{q} = \mathbf{p}_1-\mathbf{p}_2 \tag{2.17}$$

$$\mathbf{K} = \frac{1}{2}(\mathbf{p}_1+\mathbf{p}_2), \tag{2.18}$$

with $\mathbf{p}_1$ and $\mathbf{p}_2$ being the momenta of the single particles.

Equation 2.16 shows that the correlation function is related to the emission function by a Fourier transformation. This suggest the possibility to reconstruct the emission function from the measured correlation function by the inverse Fourier transformation. However, this is not possible due to the mass-shell constraint. Since the correlation function is constructed from the on-shell momenta of the measured particle pairs, not all four components of the relative momentum $\mathbf{q}$ occuring on the right hand side of Equation (2.16) are independent. The mass-shell constraint can be formulated as

$$E_1^2-E_2^2 = (E_1-E_2)(E_1+E_2) = p_1^2-p_2^2 = (p_1-p_2)(p_1+p_2), \tag{2.19}$$

$$q_0\cdot K_0 = \vec{q}\cdot\vec{k}, \tag{2.20}$$

$$q_0 = \frac{\vec{K}}{K_0}\cdot\vec{q} = \vec{\beta}\cdot\vec{q}. \tag{2.21}$$

Thus, a completely model-independent reconstruction of $S(\mathbf{x},\mathbf{K})$ from measured correlation data is not possible. This implies a model-dependent analysis strategy in which a model emission function $S(\mathbf{x},\mathbf{K})$ is compared to data.

A simple, often used ansatz for the emission function in terms of very few, physically intuitive fit parameters, is for example [35, 36]

$$\begin{aligned} S(\mathbf{x},\mathbf{K}) = \frac{2J+1}{(2\pi)^3\pi\Delta\tau}\mathbf{K}\cdot\mathbf{n}(\mathbf{x})\cdot\exp\left(-\frac{\mathbf{K}\cdot\mathbf{u}(\mathbf{x})-\mu(\mathbf{x})}{T(\mathbf{x})}\right) \\ \times\exp\left(-\frac{r^2}{2R^2}-\frac{\eta^2}{2(\Delta\eta)^2}-\frac{(\tau-\tau_0)^2}{2(\Delta\tau)^2}\right). \end{aligned} \tag{2.22}$$

The factor $2J+1$ counts the spin degeneracy of the observed particle species. The assumption of local thermal equilibrium of the emitted particles at freeze-out with temperature $T(\mathbf{x})$ and chemical potential $\mu(\mathbf{x})$ is implemented with the Lorentz covariant Boltzmann factor $\exp[-(\mathbf{K}\cdot\mathbf{u}(\mathbf{x}) - \mu(\mathbf{x}))/T(\mathbf{x})]$. A directed dynamical component is included in the model via the flow field $\mathbf{u}(\mathbf{x})$. Space-time is parameterized by the longitudinal proper time $\tau = \sqrt{t^2 - z^2}$ and the space-time rapidity $\eta = \frac{1}{2}\ln[(t+z)/(t-z)]$ in longitudinal and temporal directions, and by $r = \sqrt{x^2+y^2}$ in transverse direction. The geometric properties of the source are described by the second exponential function. The spatial and temporal extension of the source are characterized by the Gaussian width R in the transverse, $\Delta\eta$ in the longitudinal, and $\Delta\tau$ in temporal direction. The absolute time-scale of the emission is fixed by τ_0.

$\mathbf{K}\cdot\mathbf{n}(\mathbf{x})$ is the flux factor through the freeze-out hypersurface whose normal direction is given by the unit vector $n_\mu(\mathbf{x})$.

More details about this ansatz can be found in [37].

2.3 Bjorken Scenario of Expanding Sources

For sources created in collisions of heavy ions the assumption of a static system is certainly not true. The sources live only for very short time periods and have inhomogeneous temperature profiles and strong collective dynamical expansion (*flow*). The momentum distribution of the emitted particles is not only determined by the thermal properties of the source but also depends on its collective behavior. For such sources the HBT radius parameters do not measure the full source size, but only so-called *lengths of homogeneities*. Inside this spatial regions the momentum distribution varies sufficiently little so that the particles can show the quantum statistical correlations. The size of the homogeneity regions varies with the momentum of the emitted particles, causing an important dependence of the HBT parameters on the pair momentum. This dependence of the pair momentum provides a tool to study the strength of the collective flow at decoupling or the freeze out time of the source.

Based on observations of a net-baryon free zone around midrapidity and the rapidity independent distribution of pions in proton-proton collisions, Bjorken developed the model of a source expanding in longitudinal direction [13].

At very high colliding energies the nuclei penetrate each other, creating a zone with high energy density at the center of the collision. This zone of high energy density expands in longitudinal direction. The velocity of each element of this source is given in a simple way by the position of the source element and the time since the collision:

$$v_l = \frac{z}{t}. \tag{2.23}$$

In this scenario, the velocity and the momenta of the emitted particles only depend on their positions. A source for which relation (2.23) is valid is called *boost invariant*. All observers in their rest frames see an infinitely long longitudinally expanding source.

As already mentioned, the momentum difference of the two particles has to be small. According to (2.23) the difference increases with the spatial distance Δz of the emitting points. The velocity gradient at the freeze-out time τ_f is given by

$$\frac{\mathrm{d}v_l}{\mathrm{d}z} = \frac{1}{\tau_f}. \tag{2.24}$$

If a difference in velocity $\mathrm{d}v_\mathrm{l}$ is compensated by the thermal velocity $\bar{v}_\mathrm{therm}$ the measured length of homogeneity is of the size $R_z = \mathrm{d}z$. The mean thermal velocity in one dimension is given by

$$\bar{v}_\mathrm{therm} = \sqrt{\frac{T}{m}}, \tag{2.25}$$

with m being the relativistic mass $m = \sqrt{m_0^2 + p_\mathrm{therm}}$. Assuming $p_l \approx 0$ in the longitudinal rest frame of the pair this reduces to $m = \sqrt{m_0^2 + p_\perp} = m_\perp$. This results in

$$\mathrm{d}z = R_z = \tau_f \cdot \sqrt{\frac{T}{m_\perp}} \tag{2.26}$$

for the homogeneity length, proposed for the first time by A. Makhlin and Y. Sinyukov [38, 39]. The measured result can not be interpreted as a geometrical extension of the source but it contains information about the freeze-out time τ_f. In addition, the homogeneity length depends on the transverse mass $m_\perp$ of the particle pair. An experimental observation of this dependence points to collective expansion of the source in the according spatial direction.

2.4 Parameterization of the Correlation Function

The most important feature of the two-particle correlation function is its width. This width is connected to the spatial extension of the source and leads to the HBT radii. The correlation function depends on the relative momentum $\vec{q} = \vec{p}_1 - \vec{p}_2$ which has three Cartesian components. Therefore it is not sufficient to describe the shape of the correlator for increasing $|\vec{q}|$ by a single width. The curvature of the correlation function near $\vec{q} = 0$ has to be described by a 3×3 tensor [35]. In order to compute the correlation function C_2, the true space-time dependence of the emission function is approximated by a Gaussian.

The arbitrary emission function $S(\mathbf{x}, \mathbf{K})$ can be written in the following form [35]:

$$S(\mathbf{x}, \mathbf{K}) \approx S\big(\bar{\mathbf{x}}(\mathbf{K}), \mathbf{K}\big) \cdot \exp\left[-\frac{1}{2}\tilde{x}^\mu(\mathbf{K}) B_{\mu\nu}(\mathbf{K}) \tilde{x}^\nu(\mathbf{K})\right] + \delta S(\mathbf{x}, \mathbf{K}) \tag{2.27}$$

with

$$\tilde{x}^\mu(\mathbf{K}) = x^\mu - \bar{x}^\mu(\mathbf{K}), \qquad \bar{x}^\mu(\mathbf{K}) = \langle x^\mu \rangle(\mathbf{K}), \tag{2.28}$$

where $\langle \ldots \rangle$ denotes an average with the emission function $S(\mathbf{x}, \mathbf{K})$:

$$\langle f \rangle(\mathbf{K}) = \frac{\int f(\mathbf{x}) S(\mathbf{x}, \mathbf{K})\, \mathrm{d}^4x}{\int S(\mathbf{x}, \mathbf{K})\, \mathrm{d}^4x}. \tag{2.29}$$

The symmetric curvature tensor $B_{\mu\nu}$ is given by

$$B_{\mu\nu} = -\partial_\mu \partial_\nu \ln S(\mathbf{x}, \mathbf{K})\Big|_{\bar{x}}. \tag{2.30}$$

For simplicity the correction term $\delta S(\mathbf{x}, \mathbf{K})$ is neglected. The space-time coordinates $\tilde{x}^\mu$ are defined relative to the *effective source center* $\bar{x}(\mathbf{K})$, which is the center of the emission function and

approximately equal to its saddle point. It is the point of highest emissivity for particles with momentum **K** and defined by

$$\frac{\partial}{\partial x_\mu} \ln S(\mathbf{x},\mathbf{K})\Big|_{\bar{x}} = 0 \qquad \mu = \{0,1,2,3\} \tag{2.31}$$

The choice

$$\left(B^{-1}\right)_{\mu\nu}(\mathbf{K}) = \langle \tilde{x}_\mu \tilde{x}_\nu \rangle(\mathbf{K}) \tag{2.32}$$

ensures that the Gaussian approximation (2.27) has the same widths in space-time as the full emission function. Inserting (2.27) into (2.16) results in

$$C(\vec{q},\vec{K}) = 1 + \exp\left[-\tilde{q}^\mu \tilde{q}^\nu \langle \tilde{x}_\mu \tilde{x}_\nu \rangle(\vec{K})\right] \tag{2.33}$$

for the correlation function. This involves the mass-shell constrain which permits to write the space-time variances $\langle \tilde{x}_\mu \tilde{x}_\nu \rangle$ as functions of $\vec{K}$ only.

Relating (2.33) to experimental data requires the elimination of one of the four relative momentum components of **q** from the exponent of the Gaussian via the mass-shell constraint. Depending on the choice of the three independent components, different Gaussian parameterizations exit, as discussed in the following sections.

2.4.1 Bertsch-Pratt Parameterization

The standard form for the parameterization of the correlation function is expressed in the *out-side-long* (*o-s-l*) coordinate system, proposed by G. Bertsch and S. Pratt [40, 41]. Figure 2.2 shows the decomposition of the relative momentum $\vec{q}$. The mean transverse pair momentum $\vec{k}_\perp$ is defined as

$$\vec{k}_\perp = \frac{1}{2}(\vec{p}_{t,1} + \vec{p}_{t,2}), \tag{2.34}$$

with the *out*-direction parallel to it and the *side*-direction perpendicular to it. The *long* component is parallel to the beam direction. The temporal component is eliminated via the mass-shell constraint

$$q_0 = \vec{\beta} \cdot \vec{q} = \beta_x q_x + \beta_y q_y + \beta_z q_z = \beta_\perp q_o + \beta_l q_l. \tag{2.35}$$

Using (2.35) to eliminate q_0 from (2.33) one obtains

$$C(\vec{q},\vec{K}) = 1 + \exp\left[-\sum_{i,j=\mathrm{s,o,l}} R_{ij}^2(\vec{K}) q_i q_j\right] \tag{2.36}$$

where the 6 HBT radius parameter R_{ij} are defined in terms of the variances of the source function:

$$R_{ij}^2(\vec{K}) = \langle (\tilde{x}_i - \beta_i \tilde{t})(\tilde{x}_j - \beta_j \tilde{t}) \rangle, \qquad i,j = s,o,l. \tag{2.37}$$

For an azimuthally symmetric sample of collision events, $C(\vec{q},\vec{K})$ is symmetric with respect to $q_s \to -q_s$ [35]. Therefore, $R_{os}^2 = R_{sl}^2 = 0$ and

$$C(\vec{q},\vec{K}) = 1 + \exp\left[-R_s^2(\vec{K}) q_s^2 - R_o^2(\vec{K}) q_o^2 - R_l^2(\vec{K}) q_l^2 - 2R_{ol}^2(\vec{K}) q_o q_l\right], \tag{2.38}$$

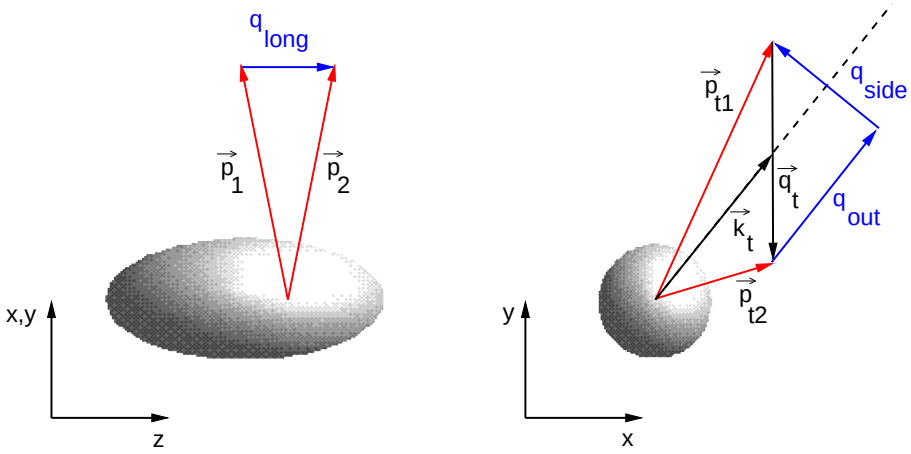

Figure 2.2: Coordinate system according to Bertsch-Pratt parameterization.

with

$$R_s^2(\vec{K}) = \langle \tilde{y}^2 \rangle, \tag{2.39}$$
$$R_o^2(\vec{K}) = \langle (\tilde{x}^2 - \beta_\perp \tilde{t})^2 \rangle, \tag{2.40}$$
$$R_l^2(\vec{K}) = \langle (\tilde{z}^2 - \beta_l \tilde{t})^2 \rangle, \tag{2.41}$$
$$R_{ol}^2(\vec{K}) = \langle (\tilde{x} - \beta_\perp \tilde{t})(\tilde{z} - \beta_l \tilde{t}) \rangle. \tag{2.42}$$

2.4.2 Yano-Koonin-Podgoretskii Parameterization

The mass-shell constraint allows for different choices of three independent relative momenta. The Yano-Koonin-Podgoretskii (YKP) parameterization uses the components $q_\perp = \sqrt{q_{\text{out}}^2 + q_{\text{side}}^2}$, q_0, and $q_\parallel = q_z$ [34, 42]. It starts from the following parameterization of the correlation function

$$C(\vec{q},\vec{K}) = 1 + \exp\left[-R_\perp^2 q_\perp^2 - R_\parallel^2 (q_\parallel^2 - q_0^2) - (R_0^2 + R_\parallel^2)(q \cdot U)^2\right] \tag{2.43}$$

Like the standard Cartesian parameterization the YKP parameterization has four $\vec{K}$-dependent fit parameters. $\mathbf{U}(\vec{K})$ is a 4-velocity, the so-called Yano-Konin velocity, with only a longitudinal spatial component:

$$\mathbf{U}(\vec{K}) = \gamma(\vec{K})\big(1,0,0,v(\vec{K})\big), \qquad \text{with} \quad \gamma = \frac{1}{\sqrt{1-v^2}}. \tag{2.44}$$

It is the longitudinal velocity of the particle emitting source.

An advantage of this parameterization is that the extracted YKP radii do not depend on the longitudinal velocity of the observer system in which the correlation function is measured. They are invariant under longitudinal boosts. In a frame where $v(\vec{K})$ vanishes their physical interpretation

is easiest and given by [35]:

$$R_\perp^2(\vec{K}) = R_s^2(\vec{K}) = \langle \tilde{y}^2 \rangle, \tag{2.45}$$

$$R_\parallel^2(\vec{K}) = \left\langle \left(\tilde{z} - \frac{\beta_l}{\beta_\perp} \tilde{x} \right)^2 \right\rangle - \frac{\beta_l^2}{\beta_\perp^2} \langle \tilde{y}^2 \rangle \approx \langle \tilde{z}^2 \rangle, \tag{2.46}$$

$$R_0^2(\vec{K}) = \left\langle \left(\tilde{t} - \frac{1}{\beta_\perp} \tilde{x} \right)^2 \right\rangle - \frac{1}{\beta_\perp^2} \langle \tilde{y}^2 \rangle \approx \langle \tilde{t}^2 \rangle \tag{2.47}$$

For a discussion of the validity of this approximation see [43].

The standard Cartesian and the YKP parameterizations are mathematically equivalent. They are based on a different choice of independent $\vec{q}$-components. The relations between the different sets of HBT parameters are given by [44]:

$$R_s^2 = R_\perp^2, \tag{2.48}$$

$$R_{\text{diff}}^2 = R_o^2 - R_s^2 = \beta_\perp^2 \gamma^2 (R_0^2 v^2 R_\parallel^2), \tag{2.49}$$

$$R_l^2 = (1 - \beta_l^2) R_\parallel^2 + \gamma^2 (\beta_l - v)^2 (R_0^2 + R_\parallel^2), \tag{2.50}$$

$$R_{ol}^2 = \beta_\perp (-\beta_l R_\parallel^2 + \gamma^2 (\beta_l - v)^2 (R_0^2 + R_\parallel^2)). \tag{2.51}$$

2.5 Final State Interactions

HBT-interferometry gives a picture of the particle emitting source at the moment of the last interaction (*freeze-out*) of the system. In an ideal world the phase-space population of the final state is determined at that moment, given by the Bose-Einstein statistics for identical particles. But even after *freeze-out* interactions between particles are possible. These so-called final state interactions lead to a modification of the phase space distribution and a distortion of the Bose-Einstein correlator.

Due to the short range of the strong interaction between pions (in the order of 0.2 fm) its influence on the final state is negligible. For source sizes of about 4 fm (obtained in collisions of nuclei with $A \approx 40$) its effect is a reduction of the chaoticity parameter λ (see page 87) of about 10% [45]. The expected source size in Pb-Pb collisions is around 6 fm. Therefore, the influence of the strong interaction should be even smaller for these systems and is neglected in the following discussion.

On the other hand, the long-range Coulomb interaction distorts significantly the observed momentum correlations for pions, dominating over the Bose-Einstein effect for small relative momenta. In the case of like-sign pion pairs the repulsion due to electric forces leads to a suppression of the correlator for small values of q. The aim of Coulomb corrections is to modify the measured two-particle correlations in such a way that the resulting correlator contains only Bose-Einstein correlations.

In the following subsections it is shown how Coulomb corrections can be calculated for given source functions.

2.5.1 Classical Considerations

The main effect of the Coulomb interaction between the particles of a pair is to accelerate them relative to each other. Thus, the two-particle correlation function is depleted at small relative

momenta for like-sign pairs and enhanced for unlike-sign pairs. This final state interaction can be reduced due to screening effects. In the presence of many produced particles, the relative Coulomb interaction is highly screened. The motion of the particles in the pair is strongly influenced by their interaction with the surrounding particles. Only when the pair has sufficiently separated from the other particles in the system the mutual Coulomb interaction or the pair becomes dominant.

Both effects are implemented in a classical toy-model presented in [46]. This model neglects Coulomb interactions between the pair for separations less than an initial radius r_0 and includes it for larger separations. The finally observed relative momentum $\vec{q}$ is related to the initial momentum of the pair $\vec{q}_0$ by

$$\frac{\vec{q}^2}{2\mu} = \frac{\vec{q}_0^2}{2\mu} \pm \frac{e^2}{r_0}, \tag{2.52}$$

with μ being the reduced mass of the pair. The plus sign is for particles of like-sign charge and the minus for particles with opposite charge. With the Jacobian $|\mathrm{d}^3q_0/\mathrm{d}^3q| = q_0/q$ the modification of the two-particle correlator is then given by (see [47, 46])

$$C(\vec{q}) = \frac{q_0}{q} C_0(\vec{q}_0) = C_0(\vec{q}_0)\sqrt{1 \pm \frac{2\mu e^2}{r_0 q^2}}, \tag{2.53}$$

where $C_0(\vec{q}_0)$ denotes the two-particle correlator in the absence of Coulomb interactions.

2.5.2 Quantum Mechanical Description

For a quantum mechanical description of final state Coulomb interactions a relative Coulomb wavefunction Ψ^{coul} is associated to the emitted particle pair. Only for particles with a difference of about 1 MeV (corresponding to the inverse Bohr radii) in momentum the Coulomb interaction plays a significant role. Because this is much smaller than the reduced pion mass of about 70 MeV a non-relativistic treatment of the problem is justified. In the center of mass system of the pair the wavefunction Ψ^{coul} is given by the solution of the Schrödinger equation

$$\left[-\frac{\nabla^2}{2m} + V(\vec{x}_1 - \vec{x}_2)\right]\Psi^{\mathrm{coul}} = \omega_p \Psi \tag{2.54}$$

with $V(\vec{x}_1 - \vec{x}_2)$ being the Coulomb potential of two particles at coordinates $\vec{x}_1, \vec{x}_2$ and ω_p being the energy Eigenwert of the pair. The solution of the equation is given analytically by the confluent hyper-geometric function F:

$$\Psi^{\mathrm{coul}}(\vec{r}) = \Gamma(1+i\eta)e^{-\frac{1}{2}\pi\eta}e^{\vec{q}\cdot\vec{r}}F(-i\eta;1;z_-), \tag{2.55}$$

$$z_\pm = (qr \pm \vec{q}\cdot\vec{r}) = qr(1 \pm \cos\theta). \tag{2.56}$$

Here, $r = |\vec{r}|$, $q = |\vec{q}|$, and θ denotes the angle between these vectors. The Sommerfeld parameter is given by $\eta = \pm\frac{\alpha}{v_{\mathrm{rel}}}$ where the plus sign is for pairs with like-sign particles and the minus sign for unlike-sign particles. The velocity of the particles in the pair relative to each other is given by $v_{\mathrm{rel}} = q/2\mu$. For pion pairs with a reduced mass $\mu = m_\pi/2$ follows:

$$\eta = \frac{m_\pi \alpha}{q}. \tag{2.57}$$

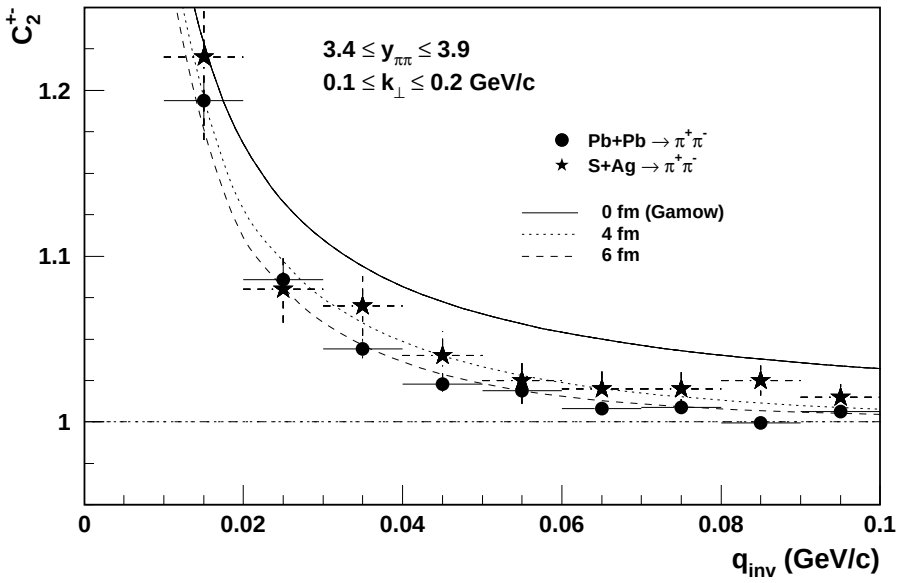

Figure 2.3: Measured two-particle correlation function C^{+-} for non-identical charged particles as a function of the relative pair momentum q_{inv}. Also shown are the calculated correlation functions based upon the Coulomb interaction for a point-like source (solid line) and finite-sized sources of radii 4 fm (dotted line) and 6 fm (dashed line). The Figure is taken from [50].

For sources with finite size and without $(\vec{x}-\vec{K})$-correlations and neglecting the time structure of the particle emission process in the pair rest frame, the corresponding two-particle correlation function for non-identical charged particle pairs is given by [48, 49]

$$C^{+-}(\vec{q},\vec{K}) = \int \mathrm{d}^3 r\, S_K(\vec{r}) \left|\Psi^{\text{coul}}(\vec{r})\right|^2. \tag{2.58}$$

$S_{\vec{K}}(\vec{r})$ describes the probability that a particle pair with pair momentum $\vec{K}$ is emitted from the source at initial relative distance r in the pair rest frame. For a parameterization of the source emission function with a Gaussian ansatz $S_{\vec{K}}(\vec{r}) \approx \exp[-\vec{r}^2/4R^2]$, the dependence of the Coulomb correlations on the size R of the source is then determined via Equation (2.58).

In the limit of a point-like source with $|\vec{r}| = 0$ the correlator C^{+-} is given by the classical Gamow function $G(\eta)$:

$$C^{+-} = \left|\Psi^{\text{coul}}(0)\right| = G(\eta) = \frac{2\pi\eta}{\exp(2\pi\eta)-1}. \tag{2.59}$$

2.5.3 Empirical Coulomb Correction

Correlations of unlike-sign particles do not show Bose-Einstein effects but only correlations due to final state interactions. This allows for the correction of the Coulomb correlations in like-sign pairs by using the information obtained by the measurement of unlike-sign correlations. The measured

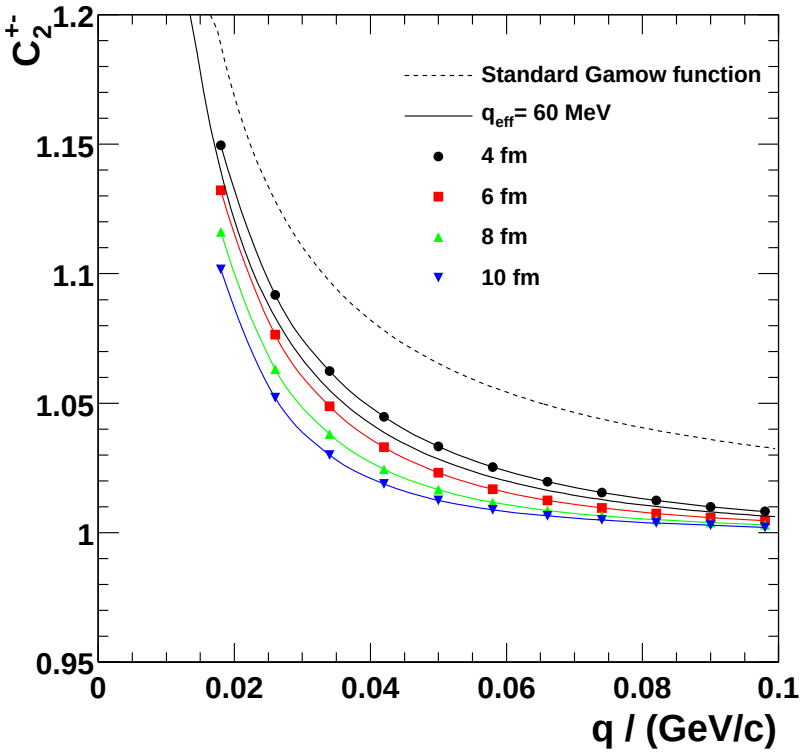

Figure 2.4: Calculated C^{+-} correlation functions for different source sizes. The standard Gamow function and the parameterization according to (2.60) with $q_{\text{eff}} = 60$ MeV are shown for comparison. Results are from [52].

correlation function $C^{+-}(\vec{q},\vec{K})$ is parameterized by a q-dependent function proposed in [51]:

$$F^{+-}(q) = \big(G(q)-1\big)e^{-q}/q_{\text{eff}} + 1. \tag{2.60}$$

The parameterization contains the Gamow function and an additional damping factor with q_{eff} as free parameter. For small q_{eff}, this function approaches the Gamow function for a point like source, while it includes a phenomenological finite-size correction for large relative momentum. Figure 2.3 shows measured correlation functions C^{+-} together with calculated correlation functions based upon the Coulomb interaction for a point-like source (standard Gamow function, solid line) and finite-sized sources of radii 4 fm (dotted line) and 6 fm (dashed line). The model used to calculate the Coulomb interaction, described in [46], integrates the Coulomb wave function Ψ^{coul} according to Equation (2.58) over a finite source volume. As one can see, the standard Gamow function does not fit to the data. It overestimates the data over the whole range of q. On the other hand, the calculated correlation functions are in good agreement with the data.

Figure 2.4 compares the standard Gamow function and the parameterization F^{+-} with the results of the numerical calculations, based on the model described in [46], for different source sizes. The calculations and the parameterizations are in good agreement and therefore it is justified to use F^{+-} to describe the effect of the Coulomb interaction on the data. Equation (2.60) with

$q_{\text{eff}} = 60$ MeV describes the expected source radii with good agreement. All Coulomb-corrected two-particle correlation functions shown in the remainder of this thesis are corrected with this parameterization with $q_{\text{eff}} = 60$ MeV.

The application of F^{+-} as a correction for the Coulomb interactions in like-sign pairs relies on the fact that the enhancement of C^{+-} compensates the suppression of C^{++} and C^{--}, i. e.

$$F^{++} = F^{--} \approx 1/F^{+-}. \tag{2.61}$$

In principle, this is not exactly true because already the Gamow functions are not equal for like-sign and unlike-sign pairs. The reason for this is the decrease of the Coulomb interaction between like-sign particles as they repel each other. On the other hand, the interaction increases for unlike-sign particles due to the attraction and the reducing distance between them. Even with the same initial conditions the transferred momentum is different in both cases. In fact, in [53] it is shown that the difference between $1/C^{+-}$ and C^{++} is very small. For $q = 10$ MeV/c it is about 3% only and becomes negligible small for higher values of q. This justifies the assumption of Equation (2.61).

3 The CERES Spectrometer with the New TPC

3.1 CERES — The Čerenkov-Ring Electron Spectrometer

The CERES/NA45 experiment is optimized for the measurement of low-mass e^+e^--pairs emitted in proton and ion induced collisions at SPS energies. The spectrometer covers the midrapidity region ($2.1 < \eta < 2.65$) and a very broad range of p_t. Until 1996 the experiment consisted of two Ring Imaging Čerenkov detectors (RICH) for electron identification, two silicon radial drift detectors (SDD), and a pad chamber. A superconducting magnet (solenoid) between the RICHes provided a deflection field for the determination of the particle's charge and momentum. The silicon detectors together with the pad chamber were used as tracking devices. With this setup CERES measured a significant enhancement of low-mass e^+e^- pairs in heavy ion collisions compared to contributions from hadronic decays, extrapolated from nucleon-nucleon collisions (see Chapter 1).

In 1998 the spectrometer was upgraded by an additional tracking detector downstream of the existing setup — a cylindrical **T**ime **P**rojection **C**hamber (TPC) with radial drift field which replaced the pad chamber. Figure 3.1 shows a cross-section of the setup. The aim was to achieve a mass resolution of $\delta m/m = 2\%$ at $m \approx 1\ \mathrm{GeV}/c^2$. This resolution allows for precise spectroscopy of the behavior of the ρ/ω and ϕ mesons in addition to the continuum measurement. Because of their short lifetimes, essentially all ρ mesons will decay inside the fireball while the ω and ϕ mesons will decay partly inside and partly outside. The goal of the upgraded CERES spectrometer was to obtain direct evidence of chiral symmetry restoration by determining experimentally whether or not the observed enhancement in the continuum is due to a modification of the vector mesons in the hot and dense medium. In parallel to the installation of the new detector the data acquisition system was rebuilt to provide an event rate capability of the spectrometer of ≈1000 events/s. This should enable a direct measurement of the yield for all three vector mesons ρ, ω and ϕ as well as any possible modifications of their properties.

The following sections describe the main parts of the spectrometer in more detail.

3.2 The Target Area with the Beam Counters

The target system used during the beam-time 2000 was made of 13 gold disks, each with a diameter of 600 μm and a thickness of 25 μm. The distance between the disks was 1.98 mm. Due to the selected diameter and distance of the individual disks the particles produced in a collision reach the sensitive detection volume of the spectrometer without traveling through further disks. This helps to minimize the conversion of γ's into e^+e^--pairs which is essential for the analysis of electron

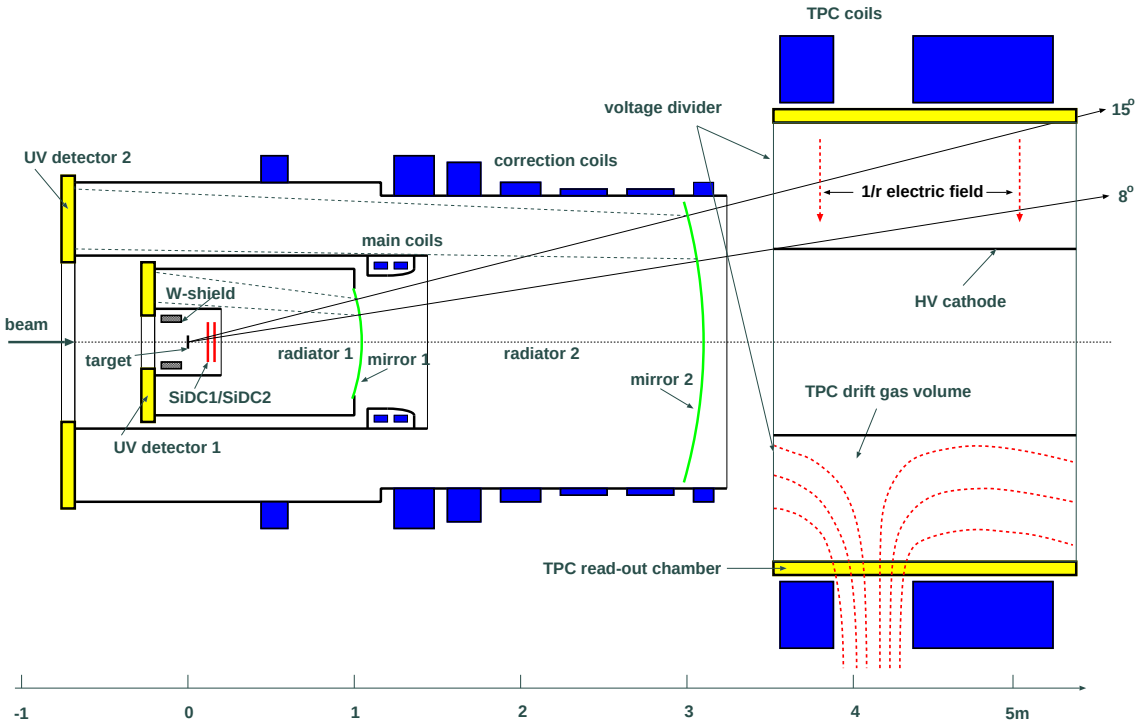

Figure 3.1: Schematic view of the CERES spectrometer.

pairs.

To start the read-out sequence of the detectors the occurrence of a collision has to be detected. This is done with a system of different beam/trigger detectors, shown in Figure 3.2 in a simplified view (see also Table 3.1). The beam counters BC1 to BC3 are used to detect collisions between projectile and target nuclei. These detectors are gas Čerenkov-counters with air as radiator, located on the beam-line. If any type of collision is detected, independent of the multiplicity of the event, the trigger condition is called *minimum bias* and the logical expression for this is given by:

$$T_{\text{minimum bias}} = BC1 \times BC2 \times \overline{BC3}. \tag{3.1}$$

The evolution of a heavy ion reaction can be very different depending on the impact parameter of the collision. A classification of the events has to use an evaluation of the final state because it is obviously not possible to track the colliding projectile and the target nuclei to measure the impact parameter in a direct way. Based on the assumption that more central collisions are more violent in a sense that they produce more particles, one can use the number of produced particles, which is called *multiplicity*, to classify an event. The most central collisions correspond to events with the highest multiplicities. However, CERES — as many other experiments — is not able to detect neutral particles and therefore the *charged multiplicity* is often used as a measure for the centrality to the collision. To select events with a certain multiplicity the MC or the MD detector can be used. These detectors are scintillation detectors and the output signal of these detectors is approximately proportional to the number of ionizing particles passing through them. Applying a threshold to the output signal allows the selection of different multiplicities. The condition for this

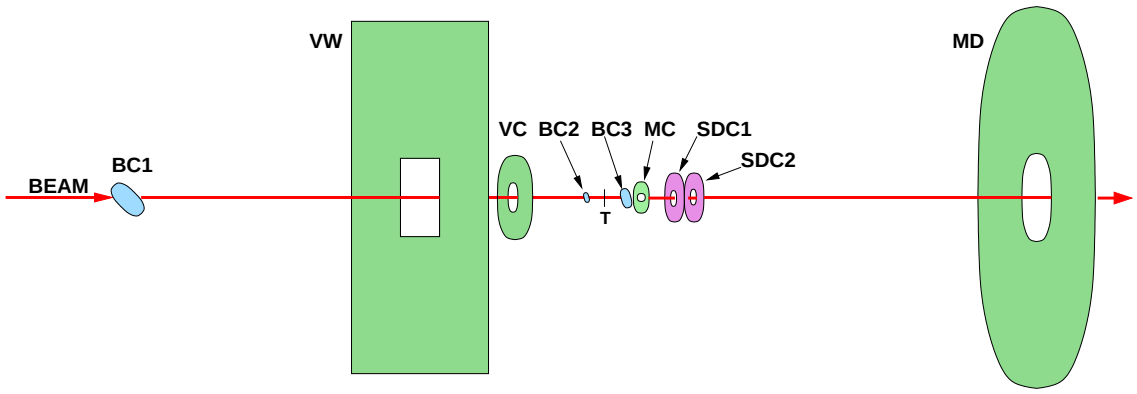

Figure 3.2: Schematic view of the target region with the trigger detectors.

so-called *central* trigger is given by:

$$T_{\text{central}} = T_{\text{minimum bias}} \times MC. \tag{3.2}$$

The veto detectors VW and VC are both plastic scintillators. They can be used to discard interactions which happened before the target.

Detector		Typ	z-Position
BC1	Beam Counter 1	Čerenkov Counter	≈-60 m
BC2	Beam Counter 2	Čerenkov Counter	-40 mm
BC3	Beam Counter 3	Čerenkov Counter	69 mm
MC	Multiplicity Counter	Scintillator	79 mm
MD	Multiplicity Detector	Scintillator	≈10 m
VC	Veto Counter	Scintillator	-2.62 m
VW	Veto Wall	Scintillator	-4.13 m

Table 3.1: Beam- and trigger detectors.

3.3 The Silicon Drift Detectors

The silicon drift detectors (SDDs) are located approximately 10 cm behind the target. Both detectors are realized on 4 inch silicon wafers with a thickness of 280 μm. The sensitive area covers the region between the radii 4.5 mm and 42 mm with full azimuthal acceptance. Due to the high pointing resolution of these detectors they are used to reconstruct the interaction vertex with a high precision.

Charged particles penetrating the detector create electron-hole pairs along their trajectory (see Fig. 3.3). The electrons are drifting in a radially symmetric electric field towards the edge of the silicon wafer. The drift field is created by voltage dividers which are implanted on the wafer. The typical drift time is around 3.8 μs. The edge of the wafer disk is divided into 360 anodes which are read out with charge sensitive amplifiers.

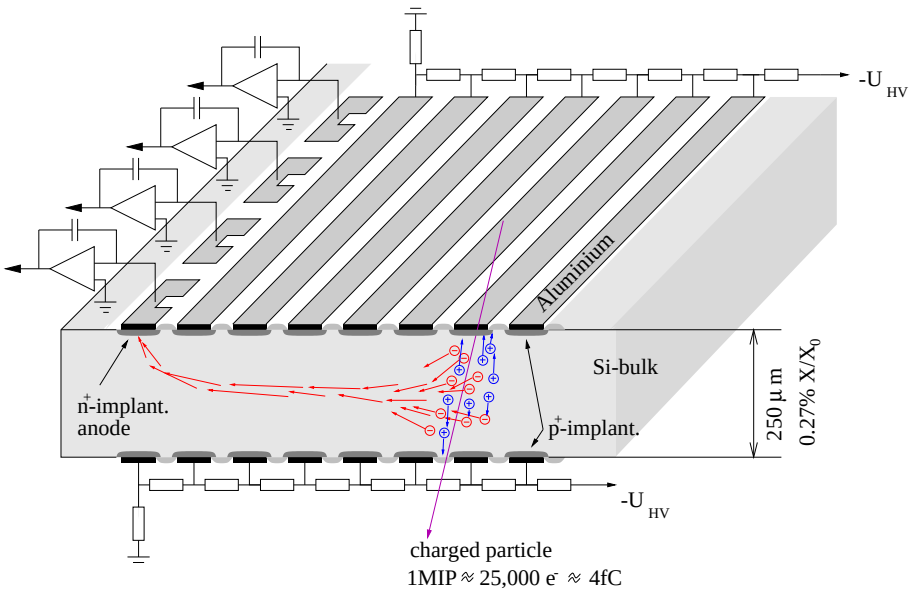

Figure 3.3: Working principle of the Silicon Drift Detectors.

The knowledge of the drift time allows for the reconstruction of the track position in radial direction. The azimuth angle is determined by the centroid of the charge shared by adjacent anodes. To measure the centroid of the charge cloud with a high precision, an interlaced structure was chosen where each anode is subdivided into 5 pieces. Figure 3.4 shows the used anode structure.

For more details see [54] and [55].

3.4 The RICH Detectors

Two Ring Imaging Čerenkov counters (RICH) are used to measure the velocity of the particle and their trajectory. If the momentum of the particle is known the mass can be determined.

The principle of these detectors was proposed by Seguinot and Ypsilantis [56] and relies on the position sensitive measurement of the emitted Čerenkov-light. Inside a radiator Čerenkov-light is emitted under a constant angle θ_C with respect to the trajectory of the charged particle.

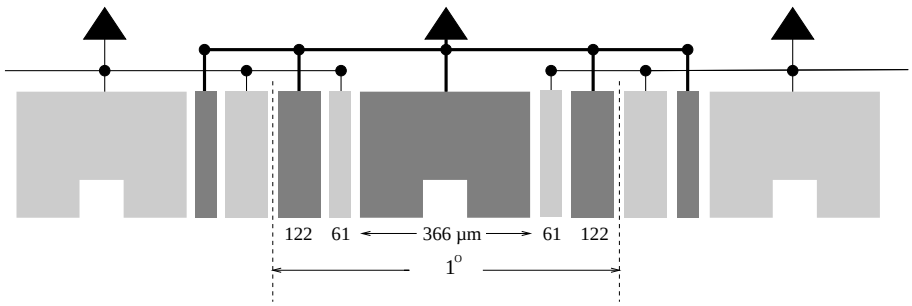

Figure 3.4: Anode structure of the SDD.

The relation between index of refraction n, velocity of the particle β and Čerenkov angle θ_C is given by:

$$\theta_C = \arccos\left(\frac{1}{\beta n}\right).$$

Emission occurs only if the velocity of the particles exceeds a certain threshold $\beta > 1/n$. The Lorentz factor for emission is given by:

$$\gamma_{th} = \frac{1}{\sqrt{1-\frac{1}{n^2}}}.$$

In the limit $\beta \to 1$ or $\gamma \to \infty$ the Čerenkov angle asymptotically reaches a maximum:

$$\theta_\infty = \arccos\left(\frac{1}{n}\right) \approx \frac{1}{\gamma_{th}}.$$

A spherical mirror reflects the emitted Čerenkov photons into ring images at the focal plane of the mirror. The diameter of these rings then corresponds to a certain Čerenkov angle and thus to the velocity of the particle.

The RICH detectors in the CERES spectrometer operate with CH_4 at atmospheric pressure as radiator gas. The threshold for light emission is thereby fixed to $\gamma_{\text{th}} = 32$. Practically all electrons produce light at the asymptotic angle whereas most hadrons, except pions with a momentum of more than 4.5 GeV, produce no signal at all. The detector is therefore practically hadron blind. To minimize the number of photon conversions in the spectrometer and to get the least possible loss of momentum resolution due to multiple scattering, the amount of material within the acceptance of the spectrometer is kept as low as possible. The RICH-1 mirror is therefore based on a thin carbon fibre structure which defines the spherical geometry and a vaporized aluminum coating for reflectivity. The radiation length is 0.4 % only. The mirror of the second detector consists of 10 glass segments with a thickness of 6 mm.

The UV detectors used for the position sensitive measurement of the photons are gas counters with a gas composition of 94% Helium and 6% Methane. They are located at the focal plane of the mirrors. The incoming photons are converted into electrons by added TMAE (Tetrakis-di-Methyl-Amino-Ethylen). TMAE is used because of its very low ionizing potential of 5.4 eV. At the working temperature of the UV detectors of 40° C the conversion length of UV photons is 5 mm. Thereby a conversion probability of 95% can be reached in the conversion region with a total depth of 15 mm. The primary electron is amplified in three steps to $2 \cdot 10^5$ e^- via avalanche creation. The ion cloud produced in the last step induces a signal on the cathode pad plane, subdivided into 53800 pads in RICH-1 and 48400 pads in RICH-2. The size of the pads in RICH-1 is 2.7×2.7 mm^2 and 7.6×7.6 mm^2 in RICH-2, corresponding to 2 mrad per pad in both detectors.

3.5 The Time Projection Chamber

In 1998, the spectrometer was upgraded by the addition of a radial **T**ime **P**rojection **C**hamber (TPC) in order to increase the mass resolution to allow a precise spectroscopy of the vector mesons ρ/ω and ϕ in addition to the continuum measurement. The design of the TPC was constrained by

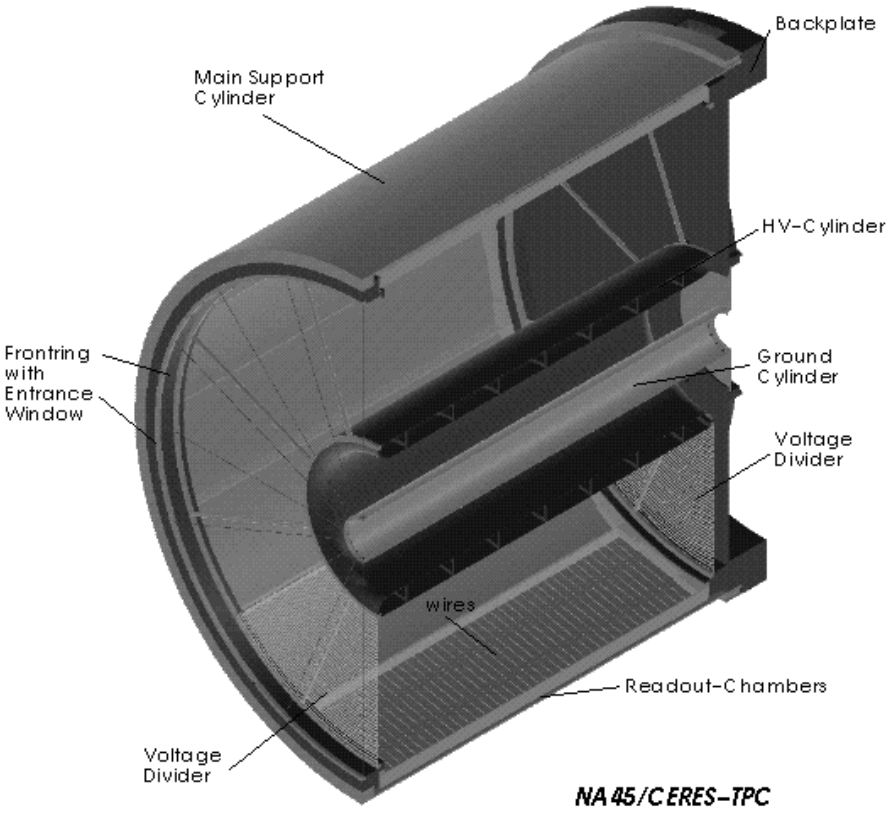

Figure 3.5: Perspective view of the TPC.

the need to preserve the azimuthal symmetry of the existing spectrometer, matching the acceptance for polar angles between 8° and 15°.

The CERES TPC (shown in a perspective view in Fig. 3.5) is a cylindrical drift chamber with the drift field in radial direction and segmented pad-readout. The sensitive volume is about 9 m^3 and the length 2 m. The inner electrode is an aluminum cylinder with a diameter of 972 mm around which 16 readout chambers are placed in a polygonal structure. The whole detector is mounted an a massive aluminum plate (*backplate*) and covered by a aluminum cylinder for mechanical and thermal stability. In total, 15360 individual channels, with 256 time samples each, can be read out, allowing a three-dimensional reconstruction of particle tracks. Along the z-axis the TPC is divided into 20 planes, each with $16 \times 48 = 768$ readout channels on the circumference.

The coordinate system of the TPC is shown in Fig. 3.6. The z-axis is defined by the beam-axis with its origin in the center of the first silicon detector. The x-axis runs horizontally along the boundary between chamber 15 and chamber 0 and the y-axis is upwards perpendicular on x and z. For the data analysis a different coordinate system is used. The position of a hit is specified by the radius r, the pad coordinate which is translated to ϕ and given by the readout channel, and the z-plane.

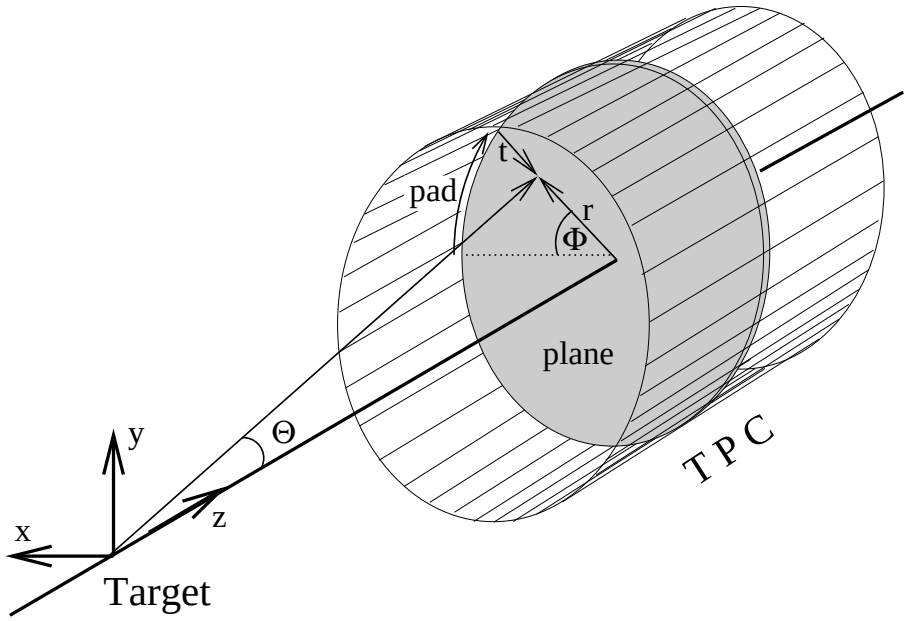

Figure 3.6: The coordinate system of the TPC.

3.5.1 Principles/Overview

Time Projection Chambers [57] allow the three-dimensional reconstruction of tracks originating from ionizing particles. They provide a large sensitive volume and are able to track several hundreds of tracks per event. A charged particle produces electron–ion pairs along its path through the detector. The electrons drift in the electric field towards a plane of proportional wires close to the pad plane. At distances of a few wire diameters the electron starts an avalanche process which creates free charges. Because the electrons are created very close to the wire they are captured by it and neutralized in a very short time. The movement of the much slower ions (about a factor 1000 slower than electrons) is responsible for the creation of the induced signal which is detected by the readout electronics. Moving charges lead to an induced current on the pads. This current is detected and recorded with the help of charge sensitive amplifiers attached to each pad. The measurement of the time between the start of the drift (which is essentially the time of the collision between a projectile and a target nucleus) and the arrival of the charge cloud at the wires combined with the knowledge of the drift velocity enables the reconstruction of the radial coordinate of the tracks. The other two spatial coordinates are determined by the location of the pad. Due to the chevron shape of the pads (see Subsection 3.5.2) the charge cloud is shared between adjacent pads. This allows for a precise reconstruction of the charge centroid in ϕ-direction. The presence of a magnetic field in the sensitive detection volume leads to curved tracks. The curvature allows the determination of the momentum of the particles.

Magnetic Field

The magnetic field is generated by two warm coils with current floating in opposite directions. The radial component of this field is maximal between the two coils and the deflection of charged

particles is mainly in azimuthal direction. The field integral is 0.18 Tm at a polar angle of $\theta = 8°$ and 0.38 Tm at $\theta = 15°$, respectively.

The Electric Drift Field

The electric drift field is defined by the inner electrode at a potential of -30 kV and the cathode wires of the readout chambers at ground potential. The resulting field shows approximately a $1/r$ dependence. The associated drift velocities are between 2.4 and 0.7 cm/μs. The maximum drift time is about 71 μs. The cylindrical drift volume is closed on both sides with 50 μm thick capton foils which are also used to build up the voltage dividers, necessary for a well defined electric field over the whole sensitive volume of the TPC. These dividers are realized with 100–200 nm thick copper strips on both sides of the foils. These strips are 15 mm wide and the distance between two of them is 5 mm. They are connected with resistors and the resulting resistor chain, connected between the inner electrode and the outer ground potential, defines the potential of each strip which is matched to follow the $1/r$ dependence of the electric field inside the TPC.

Gas Properties

Normally, the main component of the gas mixture is a noble gas which is used together with a *quencher*. As a quencher molecular gases can be used (e.g. CO_2 or CH_4). The main purpose of this component is the stabilization of the avalanche process. During the avalanche a large number of photons are created which could lead to free charges at metallic surfaces due to photo electric effects. Because of their huge number of internal excitation states the molecular gases possess a big absorption coefficient for photons and act as a counterpart to discharges.

In the CERES TPC a mixture of 80% Ne and 20% CO_2 is used. This composition was chosen after detailed studies and simulations of many different gas mixtures [58, 59] with respect to

- radiation length, i. e. multiple scattering
- number of created electron–ion pairs
- drift velocity and maximal drift time
- Lorentz angle
- diffusion coefficients

The trajectory of a particle is affected by multiple scattering in the detector gas. This results in a bias of the measured momentum. The relation between radiation length[1] and the width of the distribution of the scattering angel θ_{ms} is given by the following approximation [26]:

$$\theta_{\mathrm{ms}} = \frac{13.6\,\mathrm{MeV}}{\beta c p} z \sqrt{\frac{x}{X_0}} \left(1 + 0.038 \ln\left(\frac{x}{X_0} \right) \right). \tag{3.3}$$

In this equation, p is the momentum of the particle, βc its velocity and z its charge in multiples of the elementary charge e. The thickness of the medium, normalized to the radiation length, is

[1] The *radiation length* of material is defined as the distance over which the electron energy is reduced by a factor $1/e$ due to radiation loss only.

given by x/X_0. To minimize the effect of multiple scattering it is important to use a gas mixture with large radiation length. The radiation length is given by [26]:

$$X_0 = \frac{716.4\,\mathrm{g\,cm^{-2}}A}{Z(Z+1)\ln(287/\sqrt{Z})} \tag{3.4}$$

with A the mass number of the medium and Z its atomic number. In case of a mixture of different elements, e.g. a gas mixture, the radiation length is given by:

$$\frac{1}{X_0} = \sum \frac{w_i}{X_i}, \tag{3.5}$$

w_i meaning the fraction of the element i with radiation length X_0.

Along its path through a medium a charged particle undergoes a certain number of inelastic collisions which leads to electron–ion pairs. The created electrons can have an energy greater than the ionizing potential of the medium and thus create further electrons. The total number of created electron–ion pairs per unit length is [60]:

$$n_\mathrm{e} = \frac{\Delta E}{W_i}. \tag{3.6}$$

ΔE is the total loss in energy per unit length of a minimum ionizing particle and W_i is the mean ionizing potential of the gas. A large number of electrons is useful in terms of spatial resolution of the detector because the resolution scales with the square root of the number of electrons. On the other hand, with increasing n_e the probability for high momentum δ electrons and the influence of multiple scattering increases as well, which has a negative effect on the spatial resolution. This rules out the commonly used Argon as main component in the CERES TPC, despite of its large number of created electron-ion pairs. In the following table the properties of the Ne/CO_2 (80/20) gas mixture used are shown. For comparison the characteristics of Ar/CO_2 are shown as well.

	X_0 (m)	n_e/cm
Ne/CO_2(80:20)	280	49
Ar/CO_2(80:20)	120	93

Another important property of the gas mixture is its influence on the diffusion of the charge cloud. Thermal diffusion leads to a broadening of the drifting electron cloud. The effect is a decreased spatial resolution of the detector. Admixture of CO_2 to the detector gas reduces this effect which is particularly important in transverse direction.

The movement of charged particles in presence of electric and magnetic field is described by [61]:

$$\vec{v}_d = \frac{\mu}{1+(\omega\tau)^2}(\vec{E} + \omega\tau\frac{\vec{E}\times\vec{B}}{|B|} + (\omega\tau)^2\frac{(\vec{E}\vec{B})\vec{B}}{B^2}) \tag{3.7}$$

$$\omega\tau = \frac{\mathrm{e}}{m}B\tau = B\mu. \tag{3.8}$$

ω is the cyclotron frequency, τ the mean time between two collisions and $\mu = \mathrm{e}\tau/m$ the mobility. The drift velocity $\vec{v}_d$ comprises three components: components in direction of $\vec{E}$ and $\vec{B}$ as well as

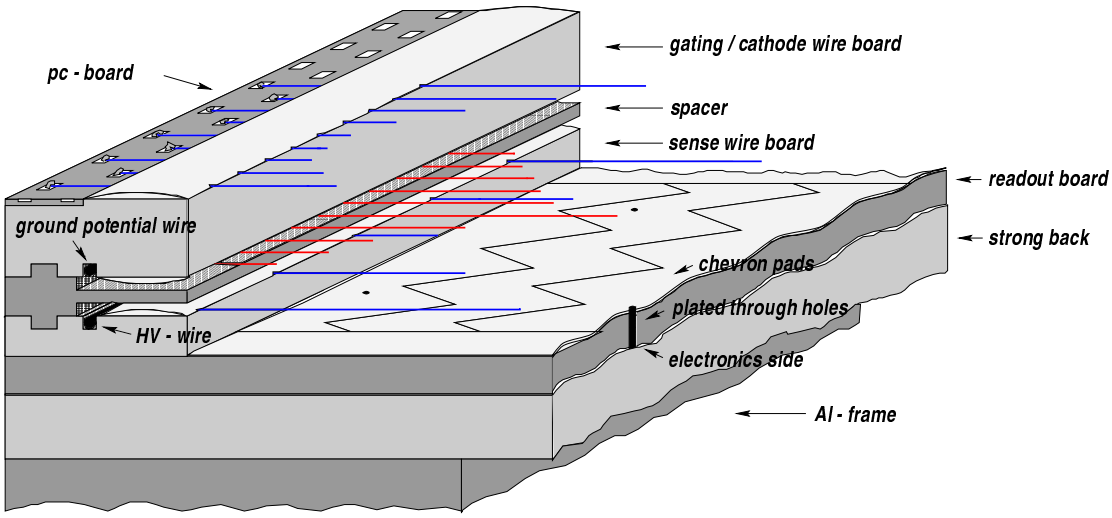

Figure 3.7: Perspective view of the TPC readout chamber.

a component orthogonal to the the plane given by $\vec{E}$ and $\vec{B}$. Because the magnetic field of the TPC possesses a component along the z-axis the drift direction of the charge does not strictly follow the electric field lines but also has a significant component in azimuthal direction. The angle between $\vec{v}_d$ and $\vec{E}$, the so-called Lorentz-angle, is given by

$$\tan \alpha_L = \omega\tau. \tag{3.9}$$

Given precise knowledge of μ, $\vec{B}$, and $\vec{E}$ the actual drift path can be calculated. However, to minimize residual uncertainties the factor $\omega\tau$ has to be small which can be achieved by increasing the CO_2 content of the gas.

However, a negative influence of the CO_2 gas component is the increased electron attachment. Drifting electrons are absorbed by the gas which leads to a deterioration of the resolution. The process responsible for the attachment is described in [62]. Important within this context is the content of O_2 in the gas. O_2 is a very efficient electron absorber and an increased CO_2 content leads to very high demands concerning the contamination with O_2. During the beam times the TPC was operated at a contamination level of 8 ppm O_2, leading to an attachment loss of 15% for the longest drift path.

3.5.2 The Readout Chambers

The following section gives a short survey of the readout chambers used in the CERES TPC. A detailed description can be found in [25]. The readout chambers are multi-wire proportional chambers with cathode pad readout (see Fig. 3.7 and 3.8). Three parallel wire planes are running in azimuthal direction: the gating grid, the cathode wires, and the anode wires.

Primary electrons are drifting in the electric field towards the cathode wires. Close to the anode wires, which are at a potential of about +1.3 kV, the electrons are multiplied by a factor of about 10^4 in an avalanche process. The movement away from the wires of the resulting ion charge cloud induces a signal on the segmented readout pad plane. This signal is amplified and shaped

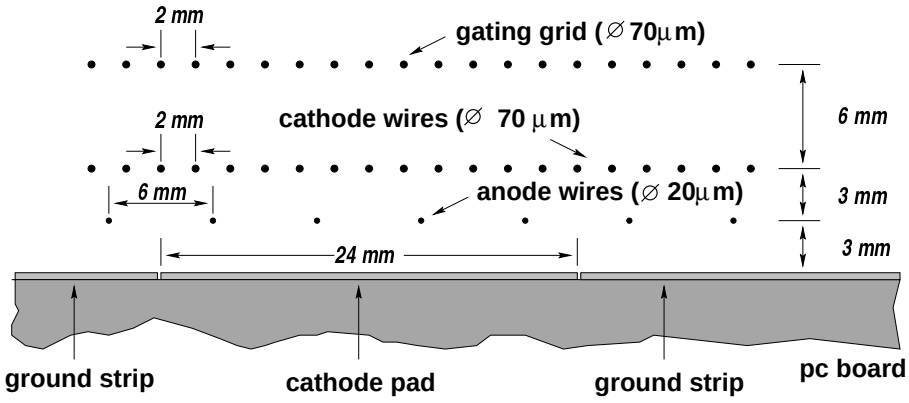

Figure 3.8: Cross section of the TPC readout chamber.

by an preamplifier with semi-Gaussian shaper, mounted directly on the backside of the pad plane. A detailed description of the front-end electronic is given in Chapter 4.

The cathode pads are shaped like a chevron [63]. The usage of this type of pads enables a precise determination of the charge centroid due to charge sharing between neighboring pads, even for relatively large pads. Another advantage of this pad geometry is the better linearity of the pad response [64]. As a result of simulations, the chevron type (b) of Figure 3.9 with $w = 10.3$ mm, $l = 6$ mm, and $f_x = 1.05$ was chosen. Four displaced single chevron structures are connected to one single readout channel with 4 anode wires running across (see Fig. 3.10). The number of readout channels in ϕ-direction has been fixed to 48 for each readout chamber.

The gating grid is necessary to protect the readout chambers from free charge inside the gas volume which is not caused by particles originating in a nucleus-nucleus collisions. It is possible to control the passage of electrons from the drift region into the amplification region with this grid. The potential of the gating grid can be regulated to switch it between a transparent or a non-transparent mode. Only after a trigger this grid is switched into a transparent mode allowing the drifting charge to reach the readout chambers.

The second function of the gating grid is to prevent the ions from floating back into the drift volume of the TPC. Free charge in the drift volume gives rise to electric fields which superimpose with the drift field and led to distortions. The positive gas ions moving towards the negative high-voltage electrode contributes the largest part to the distortion because due to the gas amplification of the primary electrons close to the anode wires approximately 10^4 electron-ion pairs per primary electron are produced. The gating grid in the CERES TPC is realized as a bipolar grid. Bipolar grids have the advantage of reduced signal coupling compared to mono polar grids (for details

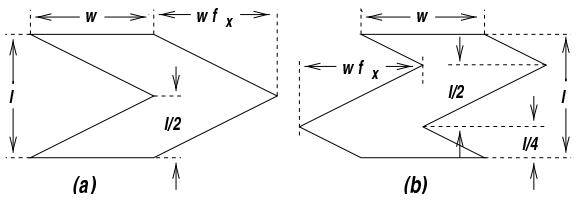

Figure 3.9: Chevron pads.

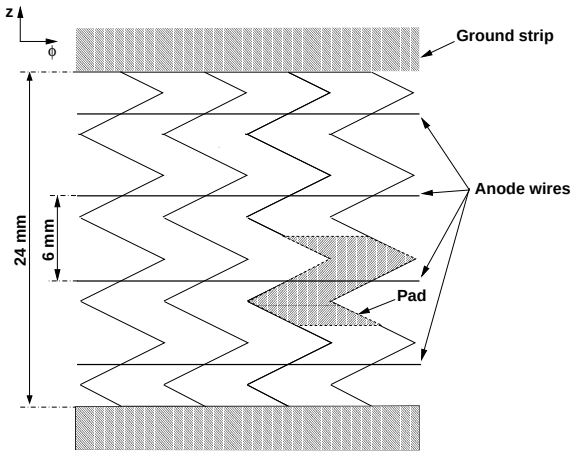

Figure 3.10: Layout of the pad plane. Four chevron structures are connected to one readout channel which is framed by ground stripes.

see [65]).

3.5.3 The Laser System

For calibration and monitoring of the properties of the TPC one would like to have straight tracks at known positions with a good resolution in space. For this purpose a laser system was attached to the TPC.

A Nd:YAG laser is used to generate a low divergence (< 0.5mrad, small diameter d $\approx$ 2 mm) laser beam with a wavelength of 1064 nm. This wavelength is too high to cause ionizations in the gas. Therefore, the frequency of the laser light is doubled twice. The resulting wavelength of 266 nm (UV) is sufficient to excite low-lying energy levels of complex molecules present in the gas volume of the TPC in form of impurities. To ionize the excited molecules a second photon is needed. Consequently, the intensity of the laser beam has to be high. With a pulse duration of several nanoseconds and a beam energy of 10-20 μJ per pulse an ionization similar to the one caused by charged particles can be achieved. The tracks can be reproduced with high precision due to missing multiple scattering and the fact that laser tracks produce a Poisson-like distribution of ionization along their path (no Landau fluctuations). The position of the tracks are determined to an accuracy of 200 μm by external diodes and the time resolution 10 ns. The response of the TPC to laser tracks at different positions and at different values of the magnetic field can be used to verify the knowledge of the electric and the magnetic fields and to test the reconstruction software. During data taking, the laser system generates events which are stored on tape in parallel to the physics events. This allows for for monitoring of the properties of the TPC during the beam-time.

With an optical system the laser beam is transported upstream the detector and aligned to the beam axis. A mirror system which is mounted on the backplane of the TPC and which can be controlled remotely allows to steer the laser beam to different quartz entrance windows distributed on the backplane of the TPC. The beam position is monitored with several position sensitive photo diodes. The information from these diodes is read out for each laser pulse and enables the

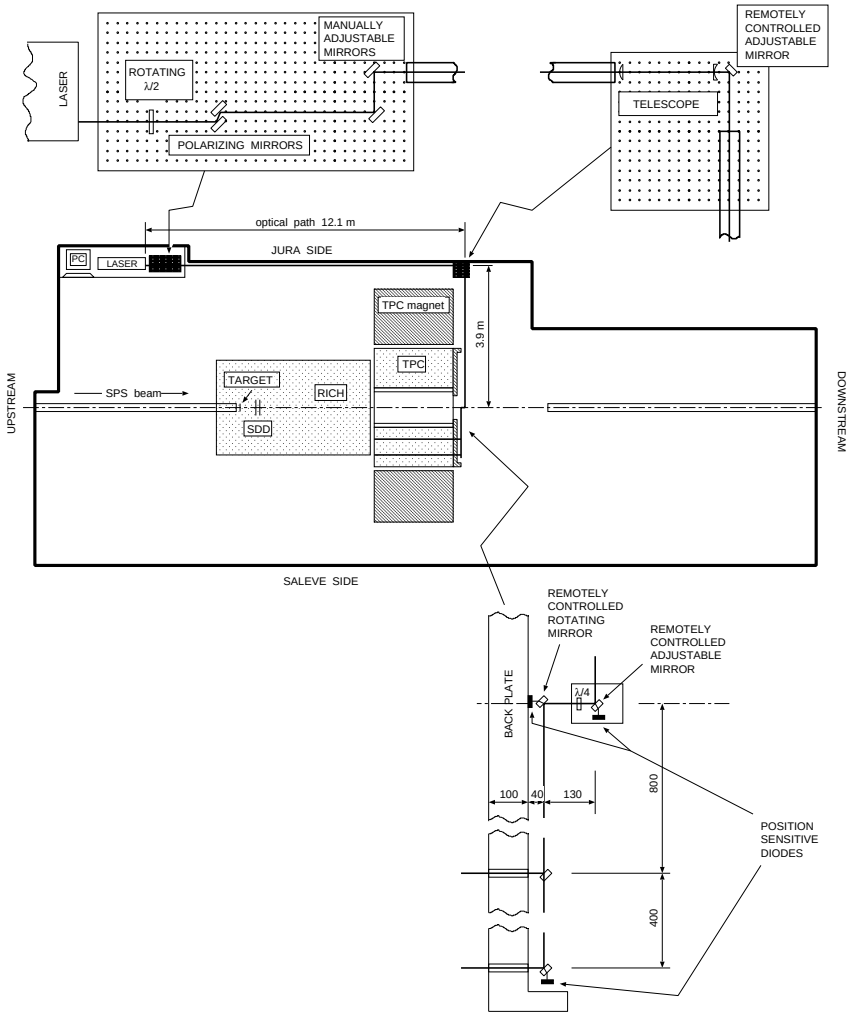

Figure 3.11: Overview of the laser system.

reconstruction of the laser track with good precision. More details about the laser system can be found in [66].

4 The Readout System of the TPC

4.1 Overview

The CERES TPC has a granularity of 15360 channels, recording 256 time samples each. Even after online data reduction by means of zero suppression and Huffman compression this constitutes a big increase in data volume per event as compared to the original CERES setup. To handle this amount of data and to be able to record $\approx$ 1000 events during a spill period of 5 s, the complete data acquisition scheme of CERES was redesigned. The new system incorporated the already existing hardware for the readout of the RICH and silicon detectors and defined a uniform interface to the event building/event recording for all detectors. For a detailed description of the RICH and silicon detectors the reader is referred to [67].

An overview of the TPC readout system is shown in Figure 4.1. In order to cope with the huge data volume, the system follows a highly parallel design. The smallest system unit comprises the complete electronics for one readout chamber of the TPC. Each of the 16 readout chambers has its own electronics which works more or less independently. The data acquisition chain starts with the front-end electronics, comprising a charge sensitive amplifier, an analog memory to record the analog output signal of the amplifier (the **S**witched **C**apacitor **A**rray) and an 8-bit Analog-to-Digital-Converter. These elements are assembled on a printed circuit board (the *FEEboard*) which is directly mounted on the readout chambers of the TPC. After digitization the data are sent to the *MotherBoards* where the simultaneously incoming data of 20 *FEEboards* are transformed into two bit-serial data streams which are transfered via two optical links to the *Receiver* boards. The *MotherBoards* are located at the backplate of the TPC and connected with flat-ribbon cables to the *FEEboards*. The *Receiver*, the first part of the so called back-end electronic, performs data reduction by applying a zero suppression followed by Huffman compression on the data stream. The resulting data are written via *FDCS* (a daisy-chain like data bus) into the *MemoryModule* where they are sorted and reformatted. From there the data are transmitted again via optical links and an intermediate station in a *compactPCI* module into the main memory of one PC which is responsible for combining the data of all detectors into the overall event data-structure (the so-called *event building*). This PC collects all data of all events belonging to one burst (a *burst* is the extraction period of the accelerator) and sends it between two bursts via TCP/IP sockets (multiple streams per PC) to disk servers located at the computer center of CERN.

A detailed description of the individual components and modules is given in the following sections.

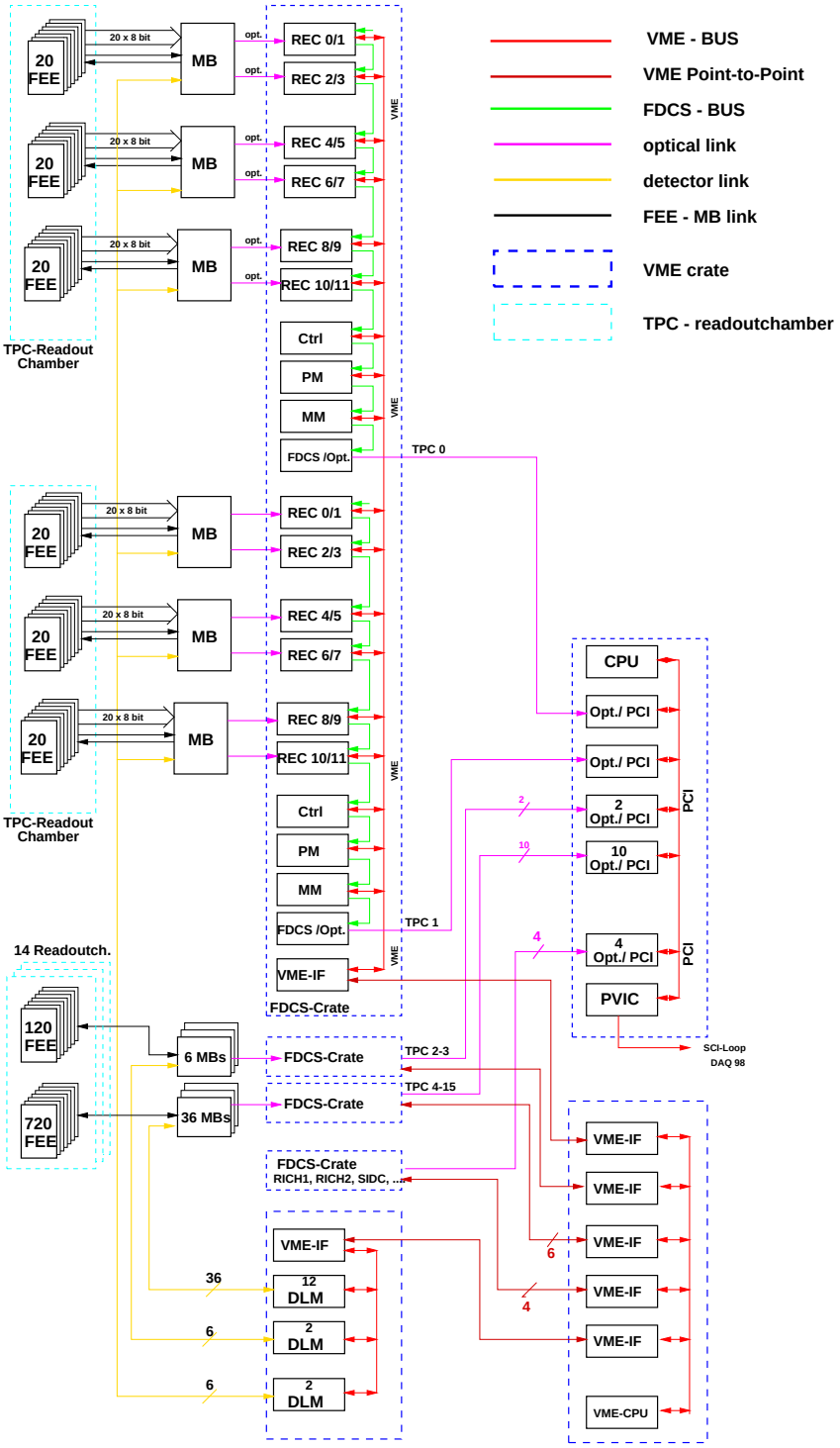

Figure 4.1: Overview of the complete readout tree for the TPC.

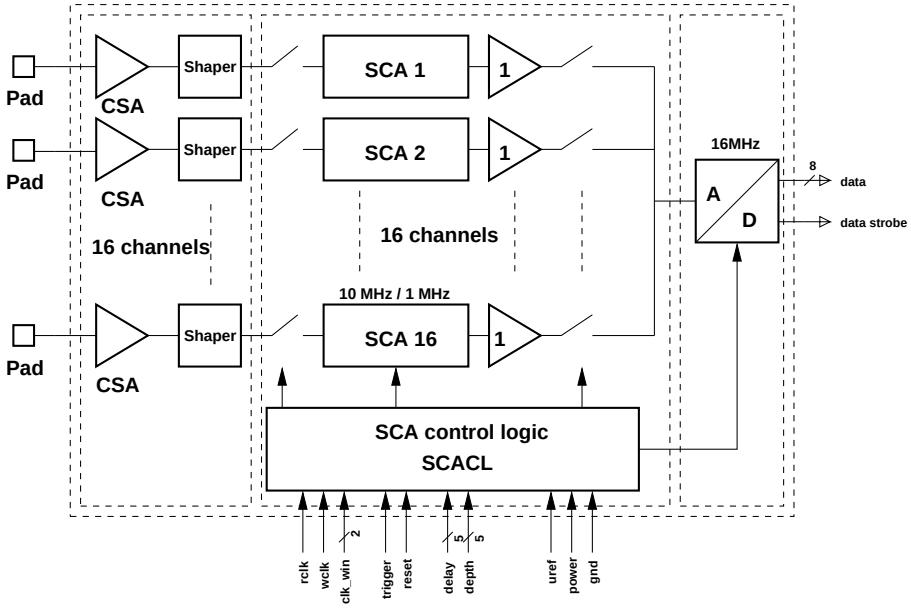

Figure 4.2: Sketch of a *FEEboard.*

4.2 The Front-End Electronic

For the front-end part of the electronics two integrated circuits have been developed: an amplifier and a **S**witched **C**apacitor **A**rray as an analog memory[68]. Both were implemented in the 0.8 μm AMS CMOS process. These two chips are the main components of the *FEEboard* which are attached directly to the pad-plane of the TPC. The boards contains also an 8-bit ADC for digitization of the signals. All necessary reference voltages for the preamplifier and the SCA are generated on-board with a DAC. Figure 4.2 shows a block diagram of the board.

4.2.1 The Amplifier

The amplifier is a charge-sensitive type (CSA[1]) with a semi-Gaussian shaper and tail suppression, shown in Fig.4.3. In contrary to common other designs which use a pulsed reset (e.g. the amplifier of the STAR experiment at RHIC [69]), this amplifier is continuously sensitive. In amplifiers with a pulsed reset the feedback capacitance C_f which integrates the signal charge is discharged with with a logical signal to prevent the CSA from being saturated by subsequent tracks. The drawbacks of this scheme are dead time, a blind system until the next reset cycle if a large undesired signal is collected, and the need for digital signals running on an analog low noise circuit. In order to avoid these imperfections for the CERES amplifier the scheme shown in Figure 4.3 was used. A feedback resistor M_f continously discharges the integration capacity C_f with a decay time $T_{\text{decay}} = C_f M_f$. The value of M_f is a trade-off between noise performance and the capability to process events with high occupancy. For a peaking time $T_{\text{decay}} = 400$ ns, noise considerations dictate a feedback resistance $M_f > 4\text{M}\Omega$. The only practical way to implement such a high resistance in

[1] **C**harge **S**ensitive **A**mplifier

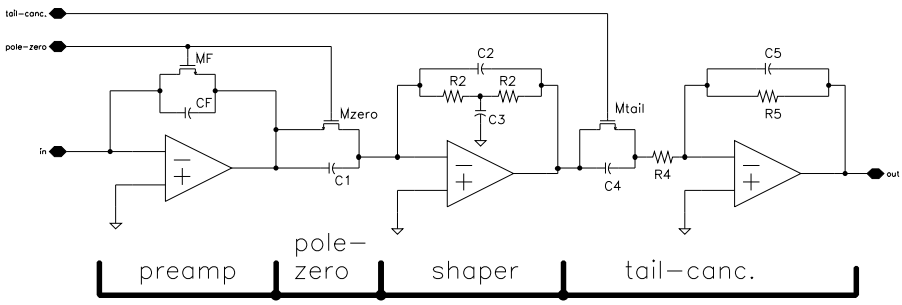

Figure 4.3: Schematic of the charge-sensitive amplifier used in the *FEEboards*.

CMOS technology is by using the associated drain-source resistance $R_{\mathrm{ds}}^{\mathrm{MF}}$ of a MOSFET transistor. $R_{\mathrm{ds}}^{\mathrm{MF}}$ depends on the biasing conditions of M_f. It decreases as the drain-source voltage $V_{\mathrm{gs}}^{\mathrm{MF}}$ of M_f increases. This dependence is an advantage in our case as signal charges increase $V_{\mathrm{gs}}^{\mathrm{MF}}$: the integration of small charges results in small $V_{\mathrm{gs}}^{\mathrm{MF}}$ swings, thus $R_{\mathrm{ds}}^{\mathrm{MF}} \approx R_{\mathrm{ds,DC}}^{\mathrm{MF}}$, its value being high enough to prevent deteriorate the noise performance. Conversely, large charges are discharged with a faster decay time and the baseline of the CSA is quickly restored. Even more important is that undesired large signals (as delta electrons) collected on TPC pads are transferred onto C_f and quickly discharged, minimizing dead time.

If a conventional pole-zero cancellation would be used, the dependence of $R_{\mathrm{ds}}^{\mathrm{MF}}$ on Q_{in} would deteriorate the linearity of the preamplifier-shaper. To resolve this issue, an adaptive pole-zero cancellation scheme was used to suppress the pole associated with $R_{\mathrm{ds}}^{\mathrm{MF}}$ and C_f. The transistor M_{zero} is biased in the same way as M_f during the discharge of C_f. The zero associated to the network $M_{\mathrm{zero}} - C_1$ adapts itself dynamically to accurately cancel the pole associated to the network $C_f - M_f$.

The peaking time of the shaper can be adjusted between 140 ns and 580 ns and the tail suppression can be varied over a range of 0.1 μs–1.5 μs to cope with different input signals due to various detector gases. The gain of the preamplifier can be adjusted from 35–110 mV/fC.

4.2.2 Linearity of the Preamplifier

In order to measure the linearity of the preamplifier one has to stimulate it with more or less realistic input signals. A “typical” pad-signal looks like the one shown in Figure 4.4. The pulse shown is the result of a Monte-Carlo simulation of the detector including the drift of the electrons and ions in the gas volume and the avalanche process in the vicinity of the anode wires. The Figure shows the current which flows onto the pad and the integrated signal corresponding to the total charge accumulated on the pad.

The signal was generated with a programmable function generator. The voltage signal at the output of the generator was converted into a current signal by means of an injection capacitor C_c. The test circuit is shown in Figure 4.5. Because the voltage at the input of the amplifier (U_{int}) is more or less fixed (“virtual ground”), the relation between input voltage U_{in} and the current $i(t)$ is given by

$$Q = C(U_{in} - U_{int}).$$

The derivative of Q with respect to time is the current flowing out of the capacitor and into the

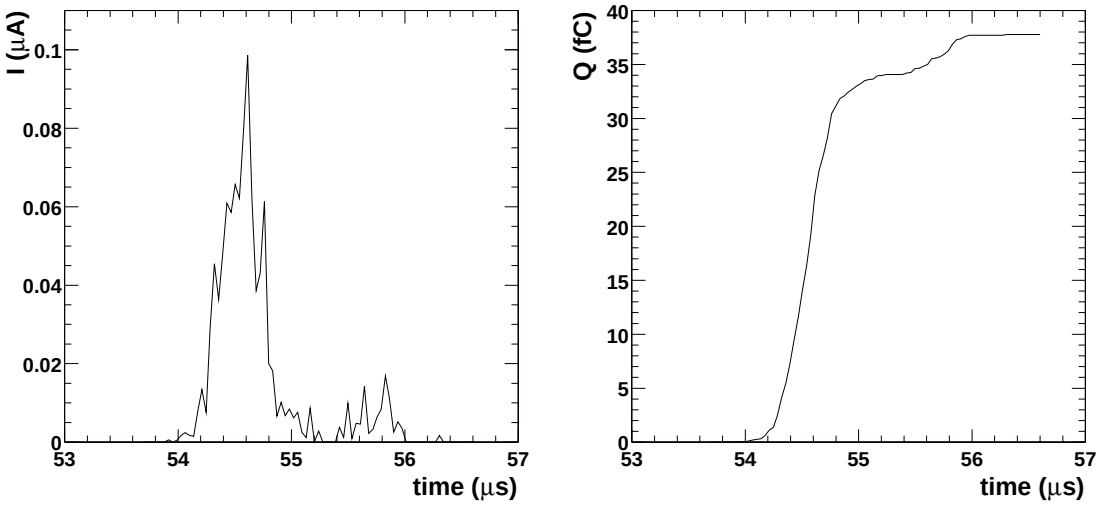

Figure 4.4: Simulated pad-signal. The current is shown in the left Figure. The right Figure shows the accumulated charge.

amplifier:

$$\frac{\mathrm{d}Q}{\mathrm{d}t} = i(t) = C\left(\frac{\mathrm{d}U_{\mathrm{in}}}{\mathrm{d}t} - \frac{\mathrm{d}U_{\mathrm{int}}}{\mathrm{d}t}\right).$$

Because U_{int} is almost constant, the expression for the current results in

$$i(t) = C\frac{\mathrm{d}}{\mathrm{d}t}U_{in}.$$

The additional capacitor C_{pad} at the input of the amplifier represents the capacity of one pad of the TPC's pad plane.

The function generator was programmed with the integrated pad current as shown in the right part of Figure 4.4 with the flat maximum of the voltage set to 5 Volts. For scaling of the input charge an attenuator was used. This device was connected between the output of the function

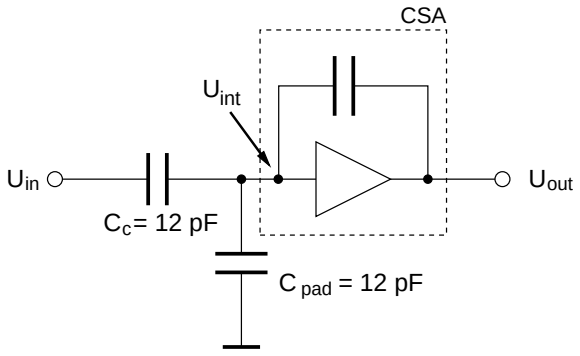

Figure 4.5: Circuit for stimulating the amplifier with realistic signals.

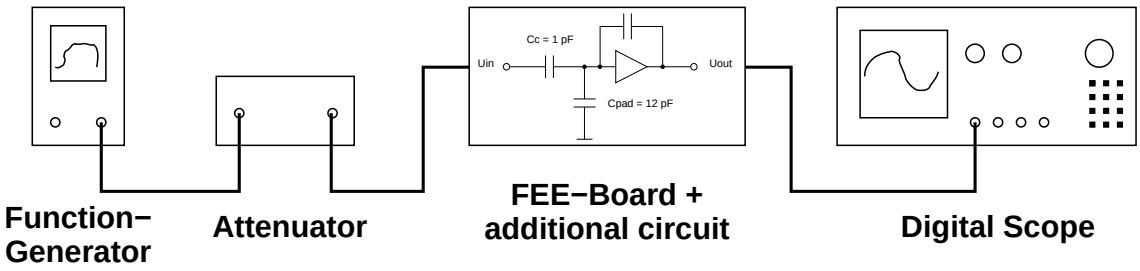

Figure 4.6: Experimental setup.

generator and the input of the amplifier. With a damping of -40 dB the input voltage (at the injection capacitor) is reduced to 50 mV, corresponding to an injected charge of 50 fC. The whole setup is shown in Figure 4.6.

The results of the measurements are shown in Figures 4.7. Shown is the output voltage as a function of the input charge for different settings of V_{tail}.

4.2.3 The Switched-Capacitor-Array

During the drift time of the TPC the output of the preamplifier is sampled and stored in an analog memory (SCA) at a rate of up to 14 MHz. After sampling is completed the stored analog data are read out and digitized with an external ADC at a frequency of up to 1 MHz. Figure 4.8 shows the simplified schematic of this device. The SCA chip contains 16 channels, each with 256 individual samples. A 16-to-1 analog output multiplexer allows the use of a single external ADC per chip.

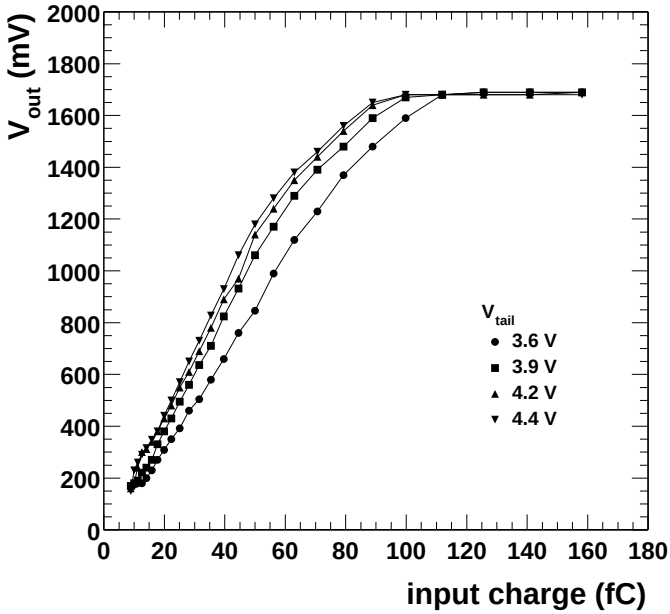

Figure 4.7: Linearity of the preamplifier.

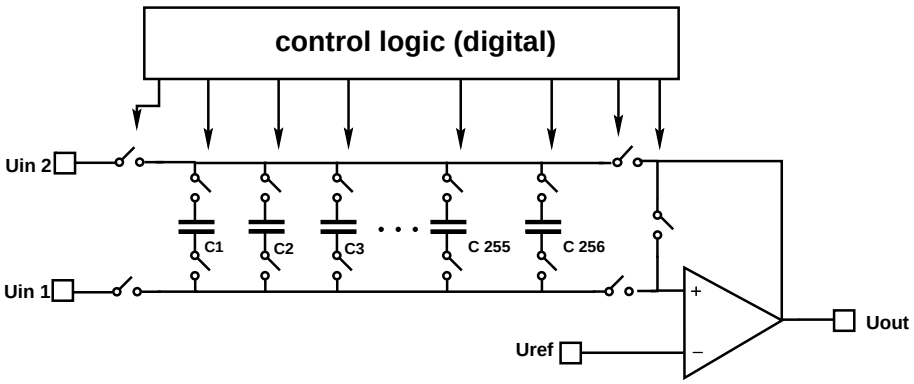

Figure 4.8: Schematic view of the SCA.

The SCA is operated in voltage-read–voltage-write configuration which has the benefit that the output is independent of the exact value of the storage capacitor. Each memory cell consists of a 1.4 pF double poly capacitor connected by two transmission gates to the common lines. This scheme reduces parasitic capacitances during read out, when the storage cells are switched in the feedback loop of an operational amplifier. Without this second switch the read-amplifier would charge the total capacitance of all bottom plates to the substrate. Because the two transmission gates are inherently less sensitive than single transistor switches, the clock feed-through and charge injections are further reduced. Only the difference of the capacitor voltages between the top- and bottom-plates are relevant and over a small range of input voltages the noise influence is the same on both plates. Symmetrical layout and only complementary signals running near analog cells ensure low switching noise caused by digital signals. The n-tub layer of the PMOS-switches is extended to cover also the capacitors in order to minimize coupling to the substrate, which in this technology is common to the digital and analog parts. The read-amplifier consists of a one-stage voltage-amplifier with an output push-pull stage and uses small sized input transistors. This is necessary since during read out charge sharing between the storage capacitor and the input capacitance of the amplifier would result in a distortion of the signal.

The digital part includes a shift register to sequentially address a column of cells. A programmable clock-window prevents overlapping addressing signals to inhibit charge-sharing between adjacent cycles. Two registers on the chip can be used to store a delay value for the start of the sampling and the maximum number of read out channels. This allows to suppress tracks outside the conical acceptance of the tracks matching to the other detectors. Additionally, the control logic provides all the necessary signals for the external components like the ADC and line drivers. After initialization, only a trigger signal and external reference clocks are needed. The digital blocks have been assembled from standard cells and take up only a small part of the total chip size.

4.3 The Control Electronic

The control electronic comprises the *MotherBoard*, the *DetectorLink* module and the *ClockModule*. Apart from the *MotherBoard*, these modules are realized as 6U VME-bus modules sitting in

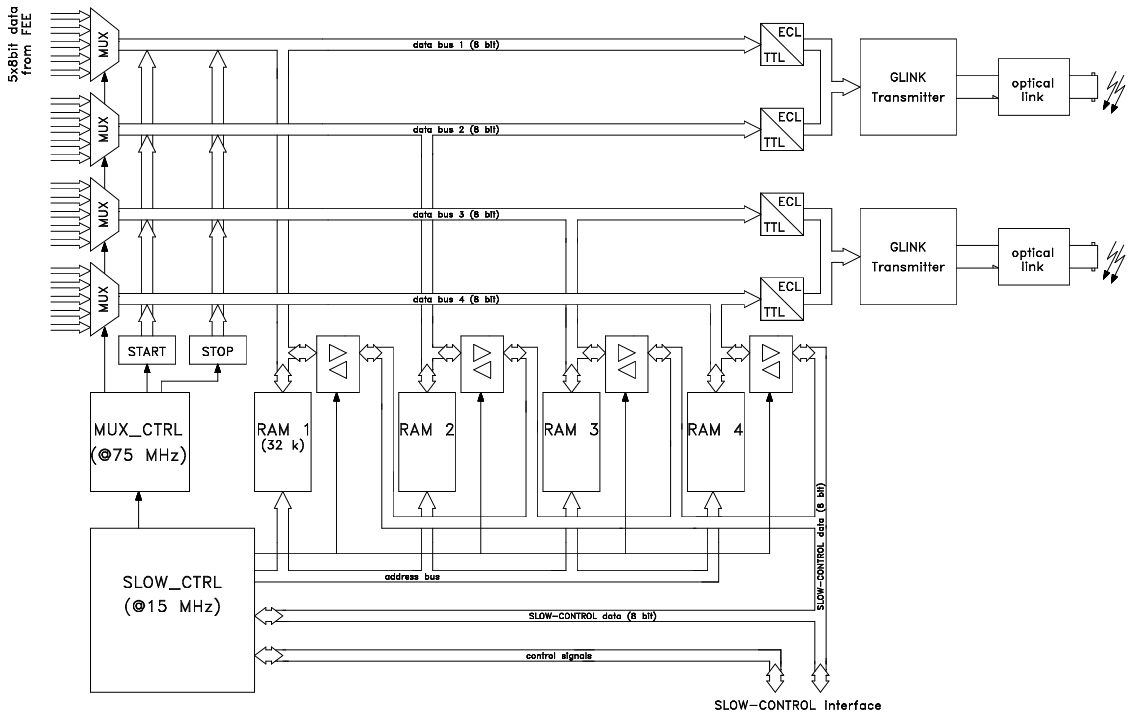

Figure 4.9: Schematic view of the Motherboard.

a crate in the vicinity of the detector. Initialization and programming of the modules is done via a CPU running OS9 as operating system located in the same crate. The CPU acts as the VME-bus master and is connected to Ethernet.

4.3.1 The *MotherBoard*

The main purpose of the *MotherBoard* is to assemble and reformat the data coming from the *FEEboards*. 20 *FEEboards* are connected with flat-ribbon cables to one *MotherBoard.* All data cables have the same length which allows to send the data without additional clock signals. The signals necessary for clocking the data into the input register are generated in the *ClockModule*. They are distributed synchronously to all *MotherBoards.*

The incoming 8-bit data are transformed into a serial bit stream which can be transmitted via an optical link to the electronics located further upstream in the readout chain. The parallel–serial transformation is done with the GLink transmitter chip of Hewlett-Packard. With 5×8-bit multiplexers the data of two *FEEboards* are connected to the 16-bit wide input of this chip. The switching of the multiplexers is done with a frequency 5 times higher than the readout frequency of the *FEEboards*. This way all data at the input of the multiplexers are processed and transmitted after 5 clock cycles and the next data from the *FEEboards* can arrive. A simplified overview of the board is given in Fig. 4.9.

The configuration and initialization of the board is done via a slow-control interface. This interface uses a very simple hand shake protocol to transmit or receive data from the *DetectorLink* module which itself receives the data via VME-bus from the CPU. The behavior of the *Mother-*

Command	Hex code	Comment
INI	0x01	Initialize the *MotherBoard* and resets the internal counters to default values.
WRITE	0x02	Initiates a data transfer to the RAM. The command is completed with the number of bytes to be written and a block of data.
CHECK	0x04	Reads the control output (one bit) of the DAC, signaling the status of the programming.
READ	0x08	Starts reading the content of the RAM. The command is followed by the number of bytes to be read.
STORE	0x10	The next event is stored in the RAM of the *MotherBoard.*
TRAM	0x20	Starts the transmission of the RAM content. The data are sent via optical link to the *Receiver* modules.
INIDAC	0x40	Starts the initialization sequence of the DACs on the *FEEboards*. The command is followed by the data for the DACs.
RESET	0x80	Resets the internal counters to default values.

Table 4.1: Motherboard commands.

Board is controlled with 8-bit codes which are interpreted by logic on the board. These codes are shown in Table 4.1.

Instead of sending the data directly via the optical links to the receiving electronics, data can also be stored in local memory on the board. From there, the OS9 CPU can read the data via the slow-control interface. This allows to bypass the rest of readout system of the TPC. This feature was very useful during the installation and test of the readout system. Essentially all data of the beam period 1998 have been recorded in this mode because the rest of the readout system was not working in a stable fashion. For test purposes it is possible to fill the memory on the *MotherBoard* with arbritrary data patterns and to send these data via the optical links to the *Receiver*. This feature mimics a freely programmable data source which simplifies debugging of the readout system.

4.3.2 The *DetectorLink* Module

The *DetectorLink* module acts as a bridge between the VME-bus protocol and the protocol of the slow-control interface of the *MotherBoard*. One *DetectorLink* module controls three *MotherBoards* associated with one readout chamber. Data for the *MotherBoards* are sent via VME-bus access to the appropriate link module which translates and forwards the data to the *MotherBoard.*

4.3.3 The *ClockModule*

The *ClockModule* (Fig. 4.10) generates and distributes the clock signals needed by the front end part of the electronic as well as the *TRIGGER* and *ABORT* signals. To ensure a synchronous sampling of the TPC channels, all *FEEboards* have to start sampling at the same time. For this reason the clock signals are generated by a central device and distributed to all *MotherBoards.* For the same reason, the *TRIGGER* signal is synchronized with respect to the sampling clock before it is sent to the *MotherBoards*. All these signals are distributed via flat-ribbon cables to

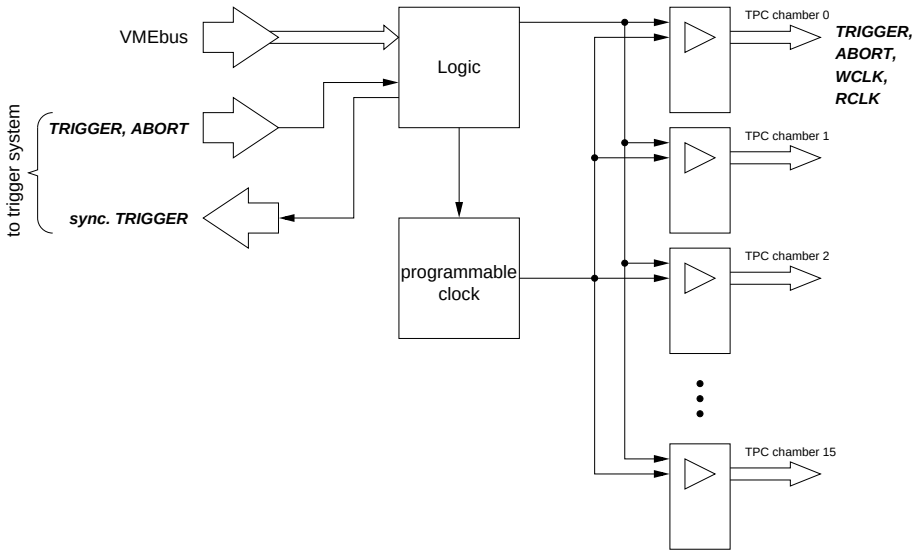

Figure 4.10: Schematic of the *ClockModule*.

the *MotherBoards* and from there to the *FEEboards*. To improve the noise performance of the system, the signals are transmitted differentially. The *ClockModule* contains a VME-bus interface (realized with a CPLD[2]) which allows setting of the two clocks. The clock signals are generated with a programmable clock synthesizer (ICD2051 from Cypress Semiconductor Corporation). The outputs can be set during operation to any desired frequency between 320 kHz and 100 MHz.

The bidirectional interface to the trigger system delivers *TRIGGER* and *ABORT* signals and returns a *TRIGGER* signal synchronized with the sampling-clock.

4.4 The Back-End Electronic

All modules of the back-end electronics are equipped with an interface to the *FDCS*[3] as well as an interface to the VME-bus. The modules sit in a modified VME crate at which the lower backplane for the connectors J2 are replaced with the backplane of the *FDCS*. This proprietary bus connects the modules in a daisy-chain, providing a simple and efficient way to move the processed data towards the personal computers used for temporary storage of the events. The VME-bus is used for initialization and controlling of the individual modules.

The data-path for one *MotherBoard* is shown in Figure 4.11. Data coming from the *FEEboards* are sent via the *MotherBoard* with two optical links to the *Receiver* boards and from there with the *FDCS* to the *MemoryModule*. The last element in this path is the *FDCS*-to-PCI interface which connects the readout system to the computers used for data storage.

[2]Lattice ISP1032
[3]**F**ast **D**ata **C**ollecting **S**ystem

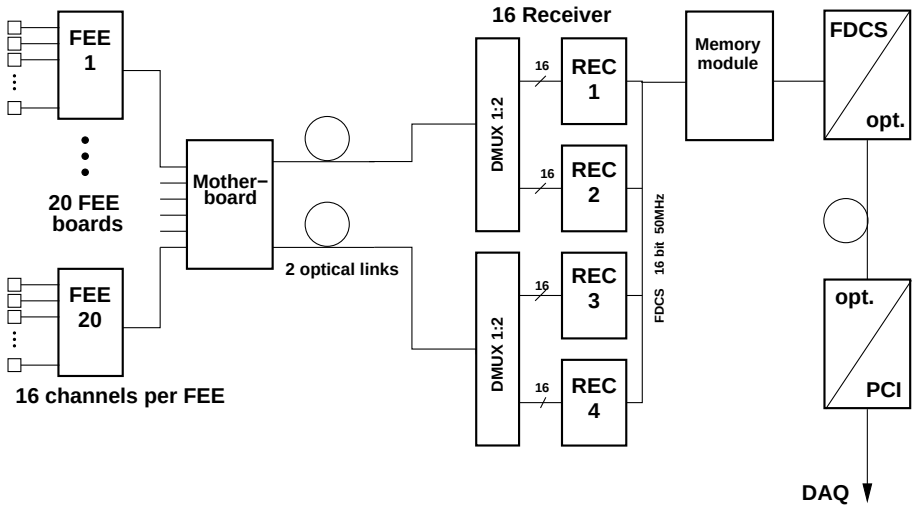

Figure 4.11: Data-path for one *MotherBoard.*

4.4.1 The *Receiver*

The data stream arriving at the *Receiver* contains all information from the detectors. Two *Receiver* are involved in processing the data coming from one *MotherBoard.* At the input of the *Receiver* the arriving data are split into two streams and both are processed in parallel in order to reduce the total processing time (cf. Fig. 4.12).

In order to meet the event rate requirements and to be able to store the data on tape, the data volume has to be reduced significantly. The data reduction is done by the *Receiver* in a two-step process: zero suppression followed by Huffman compression.

Zero Suppression

During zero suppression all amplitude values below a pre-defined threshold are removed from the data stream. For doing this, the baseline (or *pedestal*) has to be subtracted first. The pedestal with the relevant detector signal on top of it is caused by a DC offset at the outputs of the amplifier and the analog memory (SCA). Consecutive samples below the threshold are replaced by a single 9-bit value representing the number of removed samples. This allows for offline reconstruction of the time structure of the amplitudes. Since real amplitude values are represented by a 8-bit code, the 9-bit counter values can easily be recognized.

Huffman Compression

In a very general sense, data compression means the transformation of a stream of *symbols* (e.g. the digitized values of the output signals of the preamplifiers) into appropriate *codes*. With an effective compression the output code stream is less in volume compared to the input data stream. Huffman compression, a so-called lossless compression method, is based on the knowledge of the probability of occurrence of different *symbols* in the input data stream. According to these the codes are created in such a way that symbols with a high probability are replaced by shorter codes.

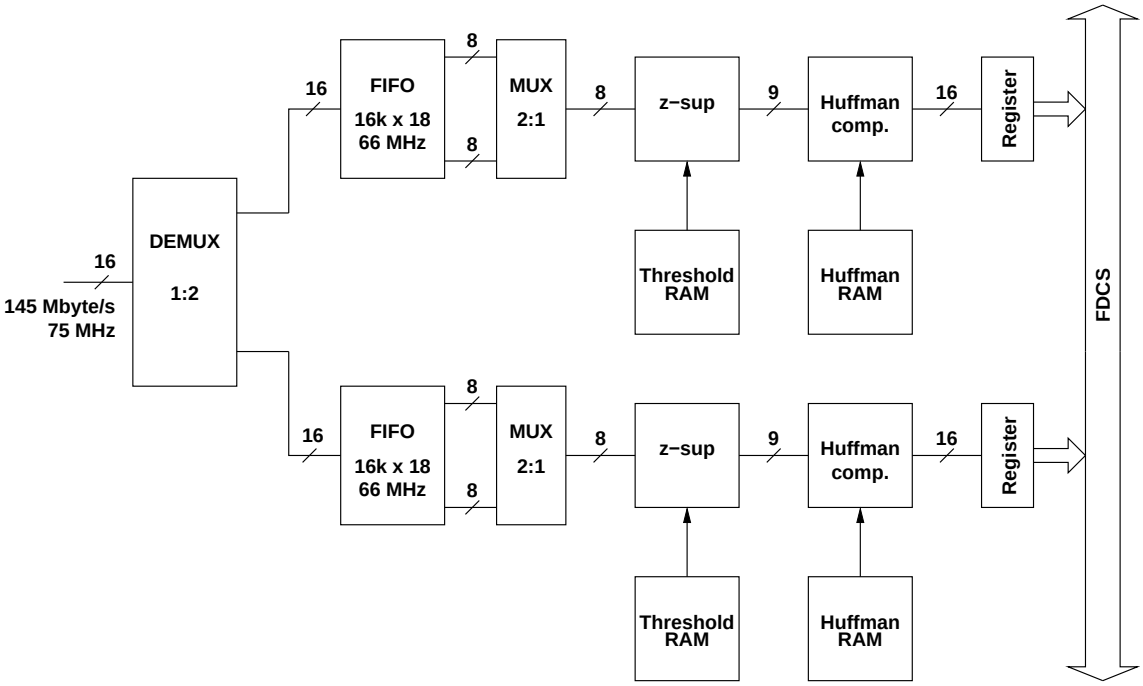

Figure 4.12: Schematic view of the Receiver board.

On the other hand, symbols which appear very rarely are represented by codes which can be longer than the original symbol. Because Huffman codes are unequivocal and are never the beginning part of another code the compressed data can be correctly decoded with the help of a binary tree. The Huffman codes are obtained by analyzing a small sample of data. The codes together with the individual thresholds for the zero-suppression are stored in a RAM on the *Receiver* boards which can be programmed via the VME-bus interface.

4.4.2 The *MemoryModule*

The *MemoryModule* is a high performance memory board. A schematic diagram of the module is shown in Figure 4.13. The VME-bus interface can handle standard D16 data transfers as specified by the VME-bus specification. Via VME-bus one can get information about the current status of the module and it can also be used to feed test data into the module. The module also has a slave interface which can be accessed in standard (24 bit, A24) address mode.

During an event the module sorts the arbitrarily incoming[4] data according to the sending *Receiver* and stores them in FIFO-memories. The *FDCS* delivers 16-bit data with a nominal frequency of 50 MHz. Immediately after the module has received all data belonging to one event it transfers the event identification number (which counts the events in one burst), the global counter value (number of received data), the sorted data, and the local counter values (number of received data for each *Receiver*) to the FDCS-to-PCI interface. After sending all data the module returns

[4]Due to the data compression inside the *Receiver* modules the order in which the compressed data are dumped onto the *FDCS* is randomized.

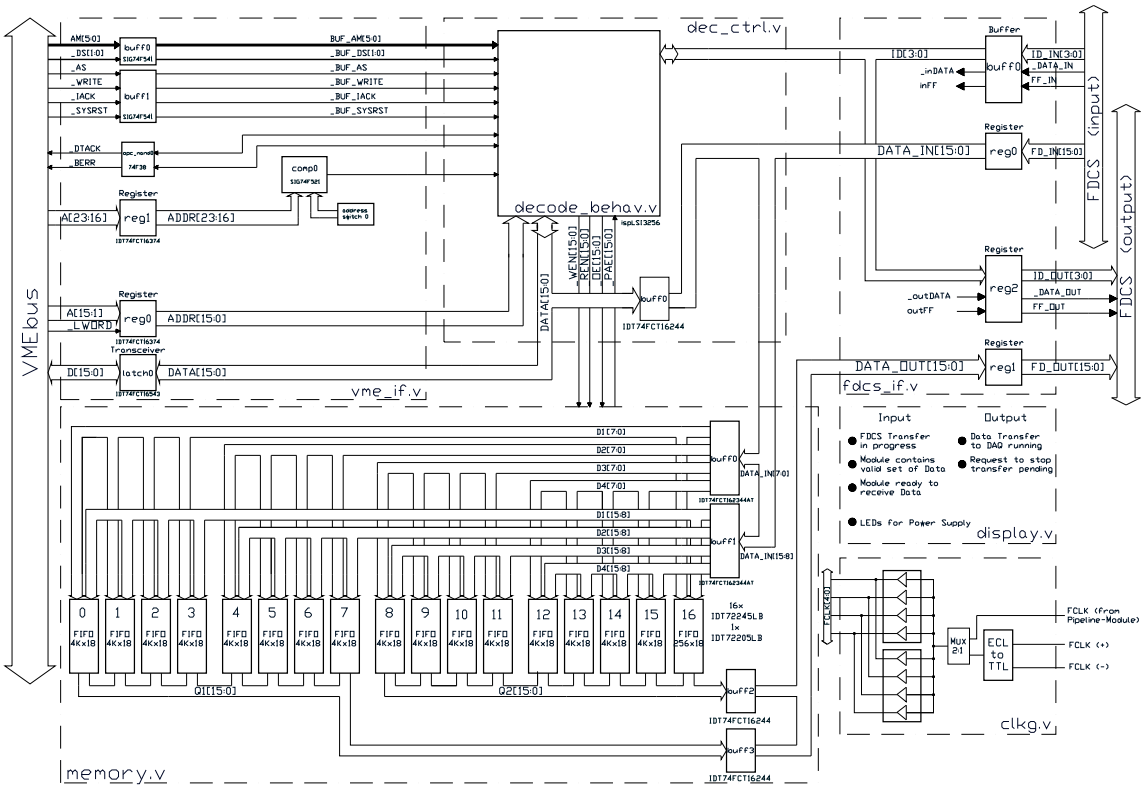

Figure 4.13: Schematic view of the *MemoryModule.*

into an idle state and waits for the next event.

4.4.3 FDCS-to-PCI Interface

The FDCS-to-PCI interface is the connection between the *Receiver*s which collect the data from the various detector systems (TPC, RICH, silicon detectors, trigger system) and the computers used for reconstruction and storage of the events. The interface has a transmitter at the *FDCS* side and a receiver at the PCI side. The connection is implemented as an uni-directional channel, utilizing an optical fiber capable of a 1.5 Gbit/s data rate. Figure 4.14 shows the block diagram of the module.

Transmitter

The transmitter picks up any value provided at the *FDCS* and sends it via an optical fiber to the receiver part. It is a 6U VME-bus module with the proprietary *FDCS* at the J2 location. The only VME-bus features of the module that are used are the mechanical support and power supply. The block diagram of the transmitter is shown in Figure 4.15. The essential part of the FDCS-to-PCI Interface is HP's Low Cost Gigabit Transmit/Receive Chip Set HDMP-1012/1014 together with an optical transmitter from Finisar[5]. The T/R link is operated in 20-bit mode with a parallel word

[5]FTR-8510 Low Cost Gigabit Optical Transceiver

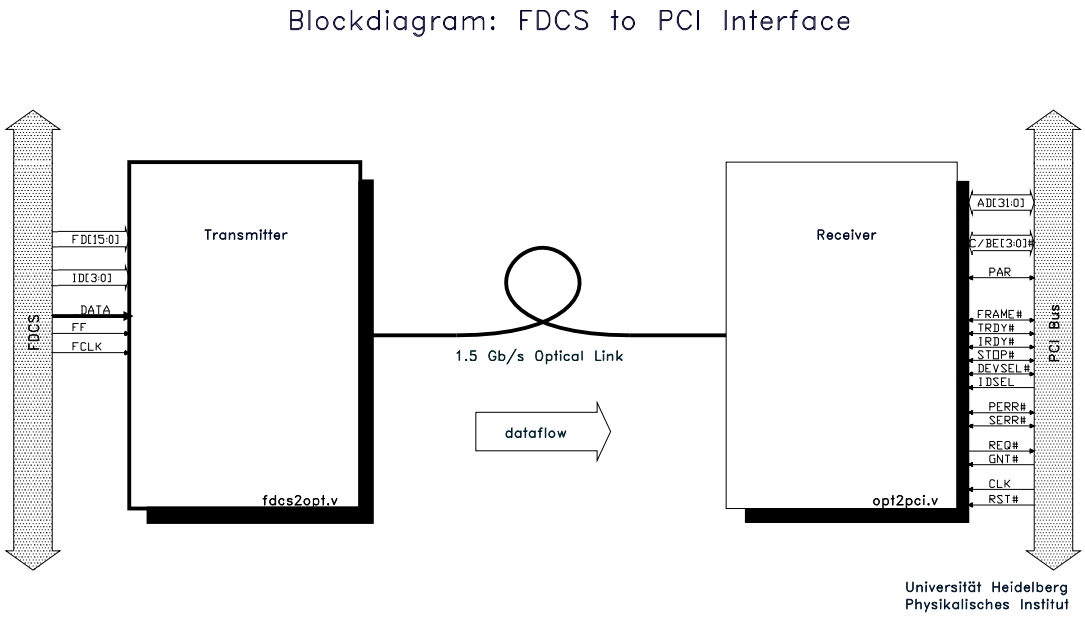

Figure 4.14: Block diagram of the FDCS-to-PCI interface.

rate of 50 MHz.

Receiver

The receiver part of the FDCS-to-PCI interface is implemented on a 6U *compactPCI* board. It receives an event sent by the *MemoryModule* and transfers it to PCs for final processing and storage. The block diagram is shown in Figure 4.16. The main part of the module is the PCI-bridge chip from PLX Technologies Inc. (PCI9060). The module supports a clock rate of 33 MHz and a bus width of 32-bit. After powering up the module or after a *RESET*, the PCI9060 is loaded via serial EEPROM with its application specific values. To initialize the module the values of three PCI-bus addresses have to be written to the module:

- target address for the Event-ID
- target address for the Global-Counter
- target address for the End-Of-Event flag

After the module has received these three values it is ready for data coming from the *Memory-Module*. Once the module has received the first three data words (containing the Event-ID and Global-Counter) it writes these data to the addresses given before. It then waits until it receives the target address for the data. The address value is written into a register of the module's logic. Immediately after it has received this address it starts to send the data with DMA transfers to the specified address. As soon as it has transferred the whole block of data it writes a '1' to the End-Of-Event flag to signal the receiving PC that it has sent all data. Then the module is ready and

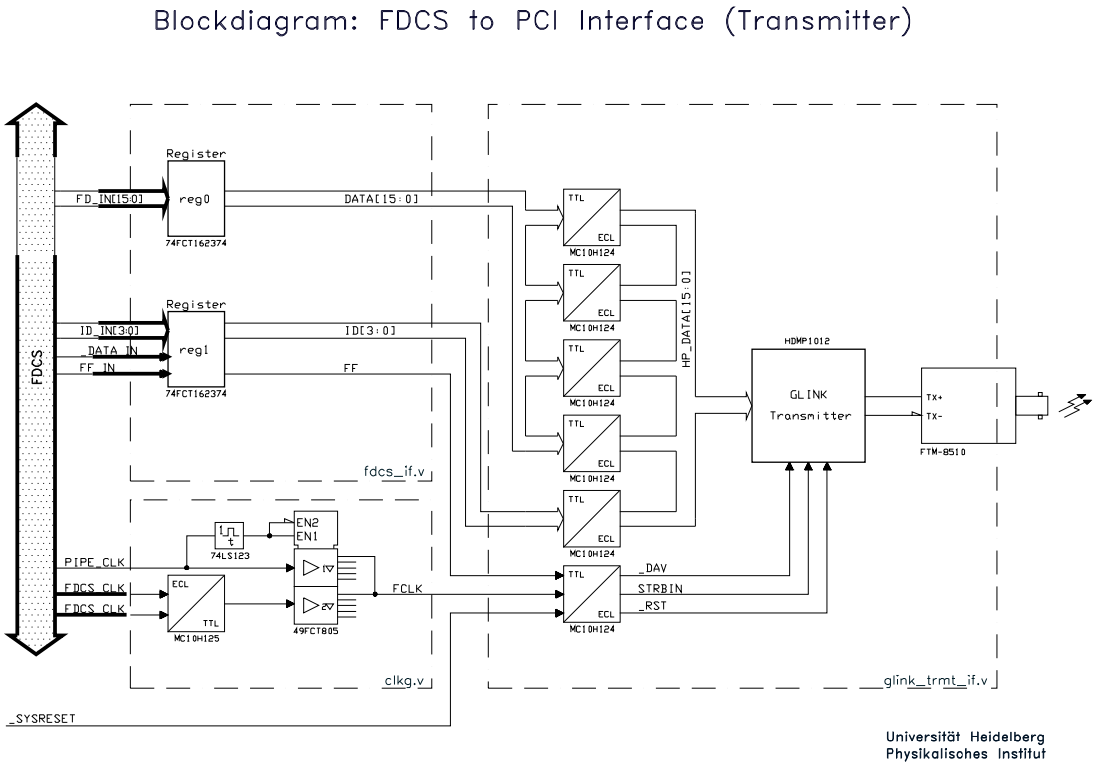

Figure 4.15: Transmitter part of the FDCS-to-PCI bridge.

waiting for the next event. A FIFO in the input data stream is used as elasticity buffer. It stores the incoming data temporarily until the module is able to transfer the event data. The used FIFO is capable to handle fully asynchronously and simultaneously read and write operations. This feature is necessary to decouple the input data rate from the outgoing data rate which is coupled to the PCI clock frequency of 33 MHz. Since the size of the FIFO prohibits to store a full event, the module has to signal the *MemoryModule* to interrupt the data transfer before an overflow occurs.

The target address for the data can change from event to event. The target addresses for the Event-ID, Global-Counter and End-Of-Event flag can only be written after power-up or manual reset of the module.

Like the transmitter part of this interface the receiver comprises HP's Gigabit chip set together with an optical receiver from Finisar.

4.4.4 The Fast Data Collection System

The **F**ast **D**ata **C**ollection **S**ystem was developed for the first readout generation of the RICH detectors. It was used to transport the data from the ADC modules to the trigger processor, as fast as possible (see [67]). In the readout system which was used for the beam periods 1999 and 2000 the *FDCS* was employed in all detector systems for the transport of the data from the *Receiver* to the *MemoryModule*.

The *FDCS* is realized as a daisy-chain. This means data are transfered from one slot to the

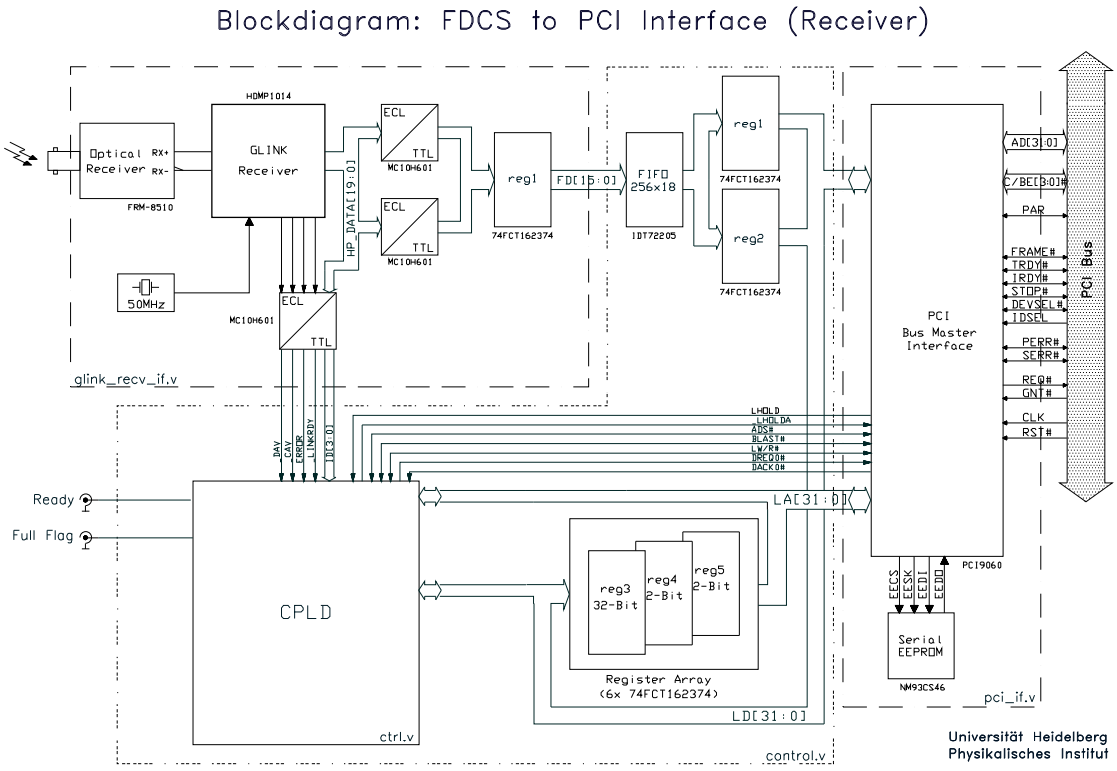

Figure 4.16: The receiver part of the FDCS-to-PCI bridge.

next via a point-to-point connection. Only a couple of control signals are distributed to all slots. The whole *FDCS* can be enabled/disabled with a control signal (*START_FDCS*). A running data transfer is flagged with the control signal *_BDATA* which is low active and driven by each data source at the *FDCS* in a wired-and configuration. Once the *FDCS* is enabled by a special control module, the *Receivers* start as soon as they have data to assert their *_BDATA* signal and put valid data in a free data slot. As long as a *Receiver* gets full data slots from its left neighbor (marked with an extra data bit *FF_IN*) it will pass them unchanged to its right neighbor. If there is a free slot from the left side, the Receiver can put a datum into the slot, mark it as full and send it to its right neighbor.

The leftmost Receiver can always put data on the *FDCS* because it has no neighbor and therefore sees only empty data slots. With that procedure all available data slots are filled on their way to the *MemoryModule* as the rightmost device. With this scheme it can happen that the rightmost *Receiver* is not able to put data on the *FDCS* for a long time because all the data slots are filled. In the original *FDCS* there was a scheme implemented to avoid this case by assigning each module a certain priority *P*. Modules with a lower priority had to let pass $15 - P$ empty data slots, where the priority can be chosen between $0 \ldots 15$. In the presently implemented version the prioritizing scheme is omitted to simplify the logic on the *Receiver*. Figure 4.17 shows the currently implemented *FDCS* logic. A detailed description can be found in [67].

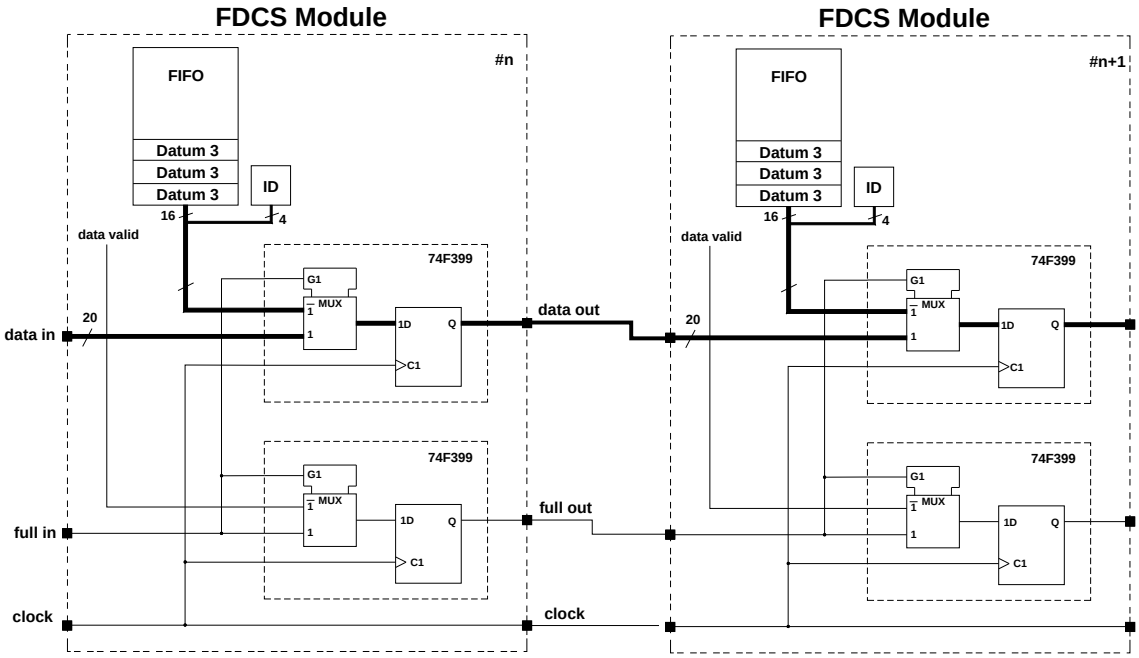

Figure 4.17: Schematic picture of the *FDCS*.

4.4.5 The Interface to Data Storage

After each accepted trigger the data stream from the detectors end up in two *compactPCI* crates as shown in Fig. 4.18. In addition to the FDCS-to-PCI interfaces these crates are equipped with a Ziatech CPU-board with a 200 MHz PentiumPro processor and a so called PVIC link. The PVIC is a high bandwidth transparent PCI to PCI link. It was developed to allow interconnection of PCI based processors or workstations, while preserving the full PCI throughput of 132 Mbyte/s block access. It utilizes a 16-bit bus operating at 66 MHz. The PVIC links connect the *compactPCI* crates with the PCs used for collecting the data from all events of one burst (*Event Builder*). The *Event Builder*-PCs are directly connected to a Gigabit switch with an up-link to the central data recording farm located in CERN's computer center. Due to limited performance in writing data to the disks, the *Event Builders* send their data to 7 individual PCs. These PCs collect the data on their internal disks and from time to time the disks are flushed to tape.

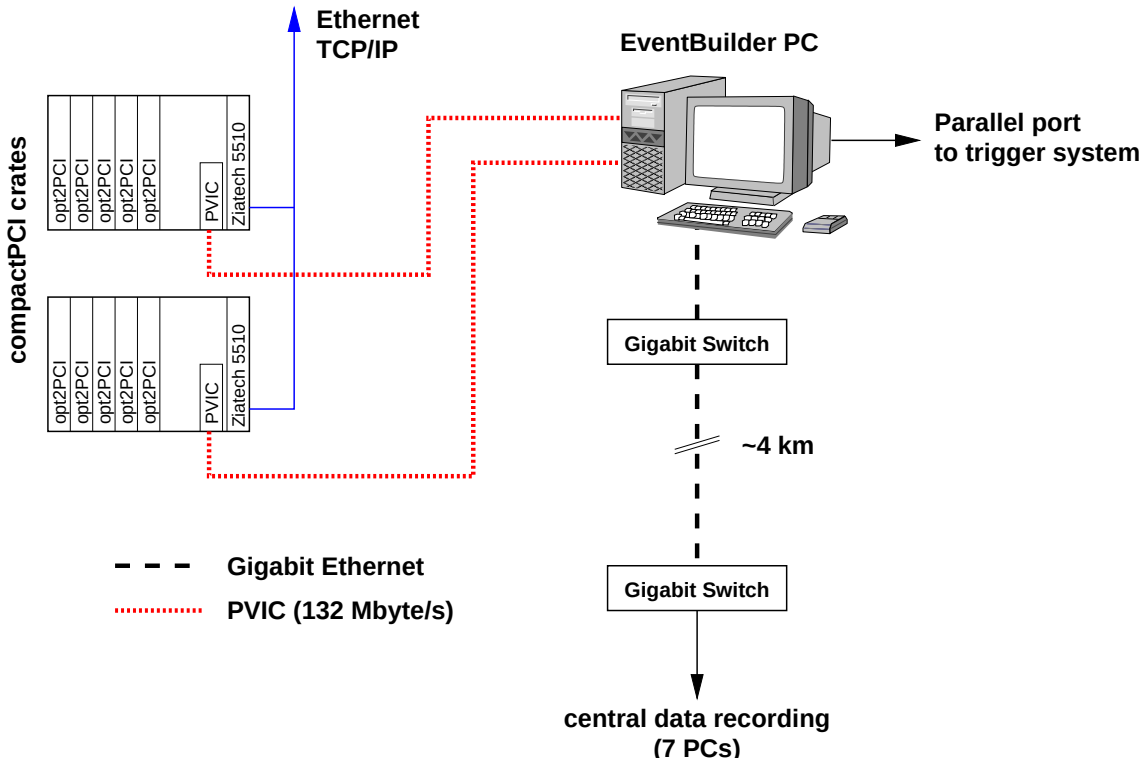

Figure 4.18: The interface of the readout electronic to central data recording.

5 The Modified Readout

Due to problems with the originally proposed readout system (as described in Chapter 4) during the beam-time in 1999, the system was significantly changed during the year 2000.

One problem of the proposed readout system was the loss of synchronization between different *MotherBoards*. Another problem was the complicated mixing of the data already at the *MotherBoard* level. Data from different *FEEboards* were combined into one data stream. This data stream was further mixed at the input of the *Receivers*. In case of a not properly working *Receiver* this leads to the corruption of a large part of the detector data. Unfortunately, this happened during the beam time in 1999 and was the reason for the changes described in the following chapter.

The data of the beam time in 2000 (beam energies of 80 AGeV and 158 AGeV) have been taken with the new readout system.

5.1 Overview

Figure 5.1 shows an overview of the CERES readout system implemented for the beam time in 2000. The analog output signals of the SCA on the *FEEboards* are sent via a shielded cable to the FEDC boards [70] where the signals are digitized. This digitization process of the FEDCs is clocked by an external clock signal which is provided by the TPC *ClockModule*.

To handle the data of two TPC chambers three FEDC modules are necessary and they are grouped in one 9U VME crate close to the TPC. Each crates is connected via a MXI[1] interface to a so-called *readout PC*. During the 5 s long burst all data are collected in the readout PCs. In the 14 s long burst pause the accumulated data are sent via Gigabit-ethernet connection to *event builder PC*, located in CERN's **C**entral **D**ata **R**ecording facility (CDR). There the data of all detector systems are merged into one data block and saved on disk. A tape daemon, asynchronously running on the machine, copies the file to tape.

Up to the *compactPCI* crate, the data paths for the silicon drift detectors and the RICH detectors are the same as in 1999. In contrast to the 1999 setup, the data of these detectors are collected in the main memory of the embedded PC which is plugged into the *compactPCI* crate. From there the data are sent via ethernet to the event builder.

The start of the readout is triggered by an external signal applied to an input channel of an I/O card plugged in the ISA bus of the readout PC. After receiving a trigger, the readout PC set a busy signal on an output channel of the I/O card. A logic OR of all busy signals is used to inhibit new triggers. After all data are sent to the readout PC the busy signal is removed.

The *MotherBoards* which were used for reformatting and compacting the data coming from

[1] **M**ultisystem e**X**tension **I**nterface

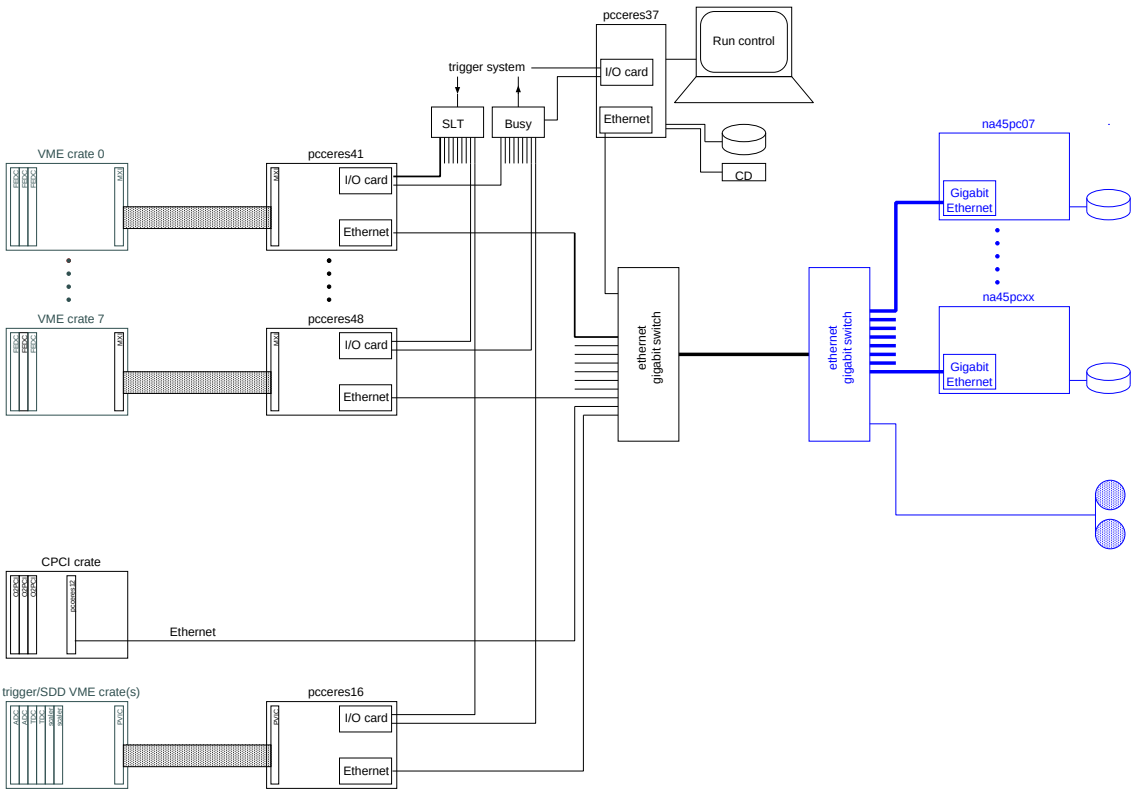

Figure 5.1: Overview of the CERES data acquisition in 2000.

the *FEEboards* are in the new system only necessary for initialization of the *FEEboards* and for distributing the various clock-, trigger- and abort-signals to the *FEEboards* belonging to one chamber.

5.2 Clock Distribution

One reason for the bad quality of the data recorded during the beam period 1999 was the loss of synchronization between different *MotherBoards* and between the so called WCLK (the signal which clocks the sampling of the SCA) and RCLK. The RCLK signal was used to clock the readout-phase of the SCA. It was also used to control the multiplexing and reformatting of the incoming FEE-data.

In the new readout-system only one clock signal (the *Master-Clock*) is generated globally with a synthesizer on the ClockModule and distributed to all *MotherBoards*. One draw-back of this is the loss off flexibility in setting the WCLK. This signal has to be generated with a counter inside the control logic of the *MotherBoards* and is fixed to $1/4$ of the Master-Clock.

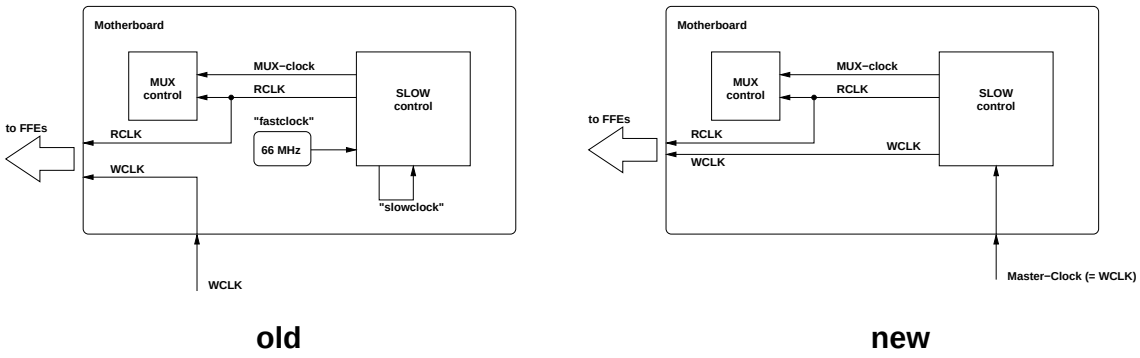

Figure 5.2: Clock distribution.

5.3 Front-End-Electronic

Instead of using a 16-bit digital data link between the front-end electronics and the *MotherBoards*, on which the data were compacted and reformatted, an analog connection to the FEDC-boards[2] was used. To match the output signal of the SCA with the input of the FEDCs an external line driver (linear buffer) was used. The output of the SCA has a maximal swing of 5 V. As long as the SCA is in the idle state the output stays at -3.0 V. During the sampling of the TPC signals the output changes to +2.0 V. Hits in the TPC result in an output signal of the SCA with a maximum amplitude of approximately 2 V on top of a baseline (DC component) of about -0.5 V. The baseline is not fixed but can be varied during the initialization of the SCA via a DAC on the *FEEboard*. In the linear buffer the signal is shifted and compressed in order to match the dynamic range of the FEDC input. The function of this buffer is depicted in Fig. 5.3. This additional driver was also necessary to drive the long cable (about 14 m) running to the FEDCs. This driver was realized on a small PCB directly glued to the *FEEboards*. The output of the SCA was rerouted to the input of the buffer, bypassing the ADC on the Front-End-Board.

[2] **F**ront **E**nd **D**igitization **C**ard

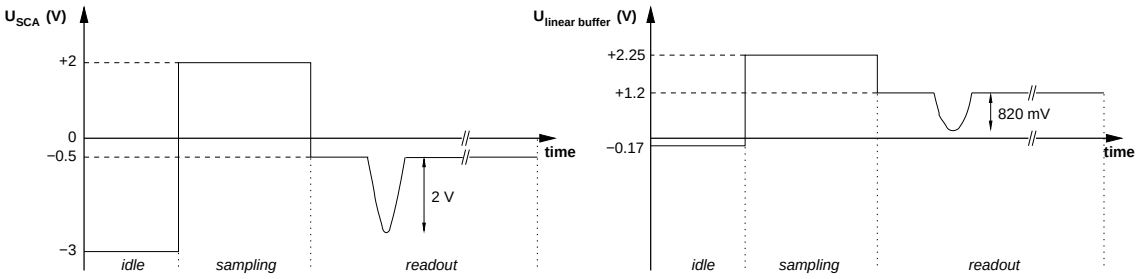

Figure 5.3: The main purpose of the linear buffer is to adjust the output signal of the SCA to the input of the FEDC.

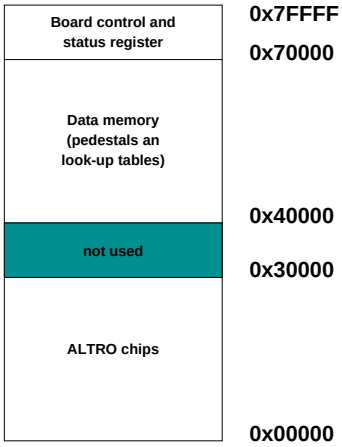

Figure 5.4: Address space of the FEDC-board.

5.4 The FEDC-board

5.4.1 Setup

The digitization and further processing of the TPC signals is done on the FEDC-boards [70]. These boards are realized as 9U VXI devices which can contain up to 48 readout channels. Each readout channel comprises a 10-bit ADC and a digital ALTRO[3] chip. Four ADCs together with four ALTRO chips are arranged on one daughter card. For the CERES readout only 40 channels per FEDC were used. Some global control registers and memory for the processed data complete the board. The FEDC-board is an A32 slave. The 5 MSB, A31–A27, define the board address. The remaining 19 bits (A18–A0) define the FEDC's address space which is shown in Figure 5.4.

The behavior of the FEDC-board and of the ALTRO chip is controlled by a set of internal control/status registers, summarized in Table 5.1 and 5.2.

Two connectors at the front panel of the module allow for the connection of the input signals. Each connector provides access to 24 channels of the FEDC of which only 20 are used. Each channel processes the data of one *FEEboard*, in fact data coming from 16 SCA corresponding to TPC pads. The *FEEboards* are connected with approximately 14 m long coaxial cables to minimize the distortion of the signals due to the noisy environment.

The event memory of the ALTRO chip has a capacity of 4096 bytes, 256 bytes for each pad. Depending on the number of accepted clusters on a pad, this is not in all cases sufficient to store all clusters. If the data of one pad exceeds the 256 bytes limit the data block of the following pad will be partly overwritten, resulting in the loss of the first clusters of this pad.

5.4.2 Signal Processing

Immediately after receiving a first-level trigger signal the SCA starts to sample the 16 outputs of the amplifier in parallel. This *sampling phase* is followed by the *readout phase* in which the stored analog values are dumped in a time-wise order (first sample of channel 0, fist sample of channel

[3] **AL**ice **T**PC **R**ead**O**ut. For the CERES readout a modified version of this chip was used.

Address	Name	Access	Description
0x70000	CSR0	R/W	[31:0]: enable bit for channels 0 to 31
0x72000	CSR1	R/W	[15:0]: enable bit for channels 32 to 47
0x74000	CSR2	R/W	[19:16]: trigger delay [12:0]: readout delay
0x76000	CSR3	R/W	[31]: flag [30:21]: event number [20:16]: board address [15:0]: event length
0x7a000	RST	W	RESET
0x7b000	EVRST	W	event counter RESET
0x7c000	TRG	W	trigger

Table 5.1: Control and status registers of the FEDC board.

Address	Name	Access	Description
0x800	CSR0	R/W	[16:9]: number of samples to process [8:1]: zero suppression threshold [0]: data stream coming from ADC (=0) or pedestal memory (=1)
0xa00	WBASL	R	access to pedestal memory

Table 5.2: Registers of the ALTRO chips.

1, . . ., fist sample of channel 15, second sample of channel 0, . . .).

The data coming from the TPC front-end electronic are digitized using a 10 bit ADC on the FEDC card of which only the 9 most significant bits are used for further processing. Therefore, inside the ALTRO chip the signals are represented by 9bit codes, ranging from 0 to 511. The baseline corresponds to a value of about 300. The processing of the incoming data is started with a trigger signal which is generated from one *MotherBoard*. After converting the analog signal the data stream is demultiplexed according to the 16 channels of the preamplifier. The resulting 16 data streams are processed in parallel inside the ALTRO chip.

In the following processing steps (see Fig.5.5) the polarity of the signal is changed and the baseline is subtracted. After this subtraction the signal should be confined within the first half of

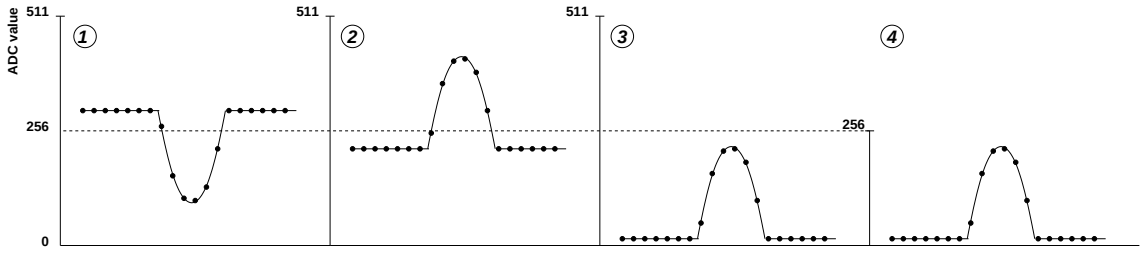

Figure 5.5: The different steps of signal processing inside the ALTRO chip.

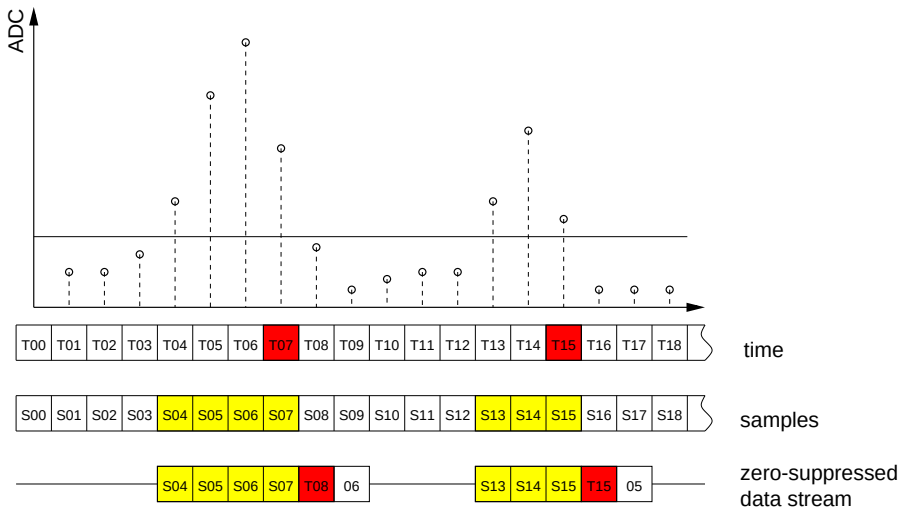

Figure 5.6: Zero suppression. Trigger at $t = 0$.

the 9 bit range. Therefore the most significant bit can be omitted reducing the signal representation to 8 bit codes. Finally, the signal undergoes the zero suppression. Samples with a value smaller than a constant threshold (8 bit) are rejected. This threshold is stored in one of the control register of the ALTRO. When a sample is found to be above the threshold, it is considered as the start of a pulse (cf. Fig. 5.6)

5.4.3 Pedestals

As each ALTRO chip processes data coming from 16 TPC-channels with maximum 256 time samples (= 4096 bytes), it was not possible to provide enough memory inside the chips to hold pedestal values for all samples. In fact, due to the stability of the pedestals and their smooth dependence on the sample time it was not also not necessary. Instead, a scheme using a look-up table was implemented. Figure 5.7 shows a pictorial representation. The look-up table contains 256 7 bit words. The index (the *line number*) of this table corresponds to the sample number. The entries are the addresses of the data-buffers which contain the pedestal values. This means, 128 pedestal values can be assigned to each channel. For this scheme only 2048 bytes for the data plus 256 bytes for the look-up table are necessary.

The format of the data files used to program the pedestal values reflects this setup. The information belonging to 4 ALTROs of one daughter card are combined in one file. The file name contains the branch number (x), the FEDC-board number (y) and the daughter card number (z): `ped_x_y_z`. Each ALTRO data block consists of the pedestal values and the look-up table. The pedestal values are arranged in 128 lines with eight 16 bit words. The first word contains the information for channel 0 and 1, the second for channel 2 and 3, and so on. The look-up table, which follows the data block, consists of 256 lines each line containing a 7 bit word.

One disadvantage of this scheme compared to the one used in the original CERES readout is the missing possibility to specify a threshold for zero-suppression for all time-bins. This feature is useful if the noise of individual time-bins is very different. Instead, the ALTRO uses one threshold

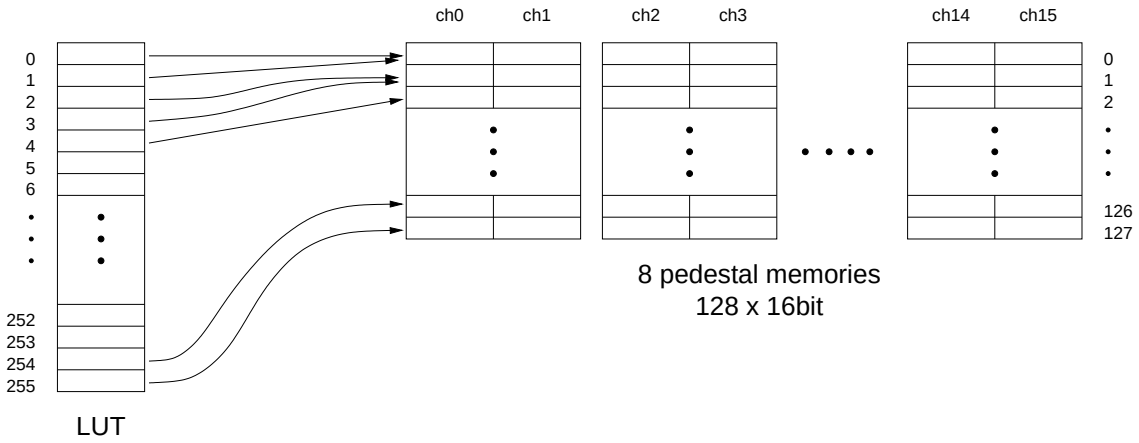

Figure 5.7: Implementation of the pedestal memory using a look-up table.

value for all time-bins (CSR0 register). This restriction was evaded by adding the threshold (determined individually for each time-bin) to the pedestal value and storing this combined value in the pedestal memory. The zero-suppression value which is used to detect the start of a pulse is set to 0. With this scheme, not only the true baseline is subtracted from the signal but also the specific threshold. If the resulting value is above zero, the pixel is considered being part of a pulse. For the off-line analysis the additionally subtracted threshold has to be added again for each pixel.

5.4.4 Data format

The event is stored in the FEDC memory as a back-linked structure as depicted in Fig. 5.8. Due to the removal of a varying number of samples between the accepted clusters, the timing information would be lost during the zero-suppression process. This requires two additional data words per recognized cluster — the time-stamp and the cluster-length — to be able to reconstruct the signals off-line. The cluster-length corresponds to the total number of samples plus the data word containing the time-stamp and the data word for the cluster-length. The time-stamp gives the (sample-)position of the last sample in the cluster relative to the trigger signal. This cluster structure (sample values + time-stamp + cluster-length) is repeated for each accepted cluster in a specific channel. These data are completed by a 32bit trailer word which contains the channel identifier and the total number of bytes in the packet. The trailer word always starts at a 32bit boundary. This is ensured by using dummy bytes at the end of the channel data structure. The data block shown in Fig. 5.8 consists of *n* clusters. Cluster 0 comprises of 5 samples, cluster 1 of only 3 and so on. This example needs two additional fill bytes at the end of the structure which are shown as well.

The overall FEDC-board data block contains the channel data blocks for channel 0 to channel 703. In the CERES version, only 640 out of 768 channels of the FEDC-board are used, numbered from 0 to 319 and from 384 to 703. The gap in the numbering is due to unused input connectors at the front panel of the FEDC.

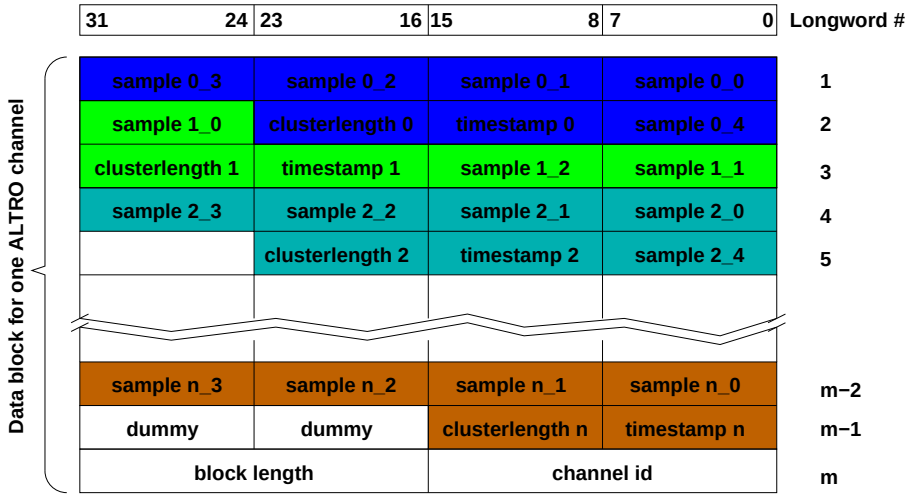

Figure 5.8: ALTRO data format

5.4.5 Trigger

To start the signal processing of the FEDCs an additional trigger signal has to be provided which is related to the switch-over from the sampling phase to the readout phase of the SCA. Such a signal already exists on the *MotherBoard* (the *data-output* signal generated by the SCA and indicating the start of the readout phase). This signal is routed from one *MotherBoard* to a fan-out module and distributed to all FEDCs simultaneously (see Fig. 5.9). A delay-line is used to synchronize this signal with the data from the SCA.

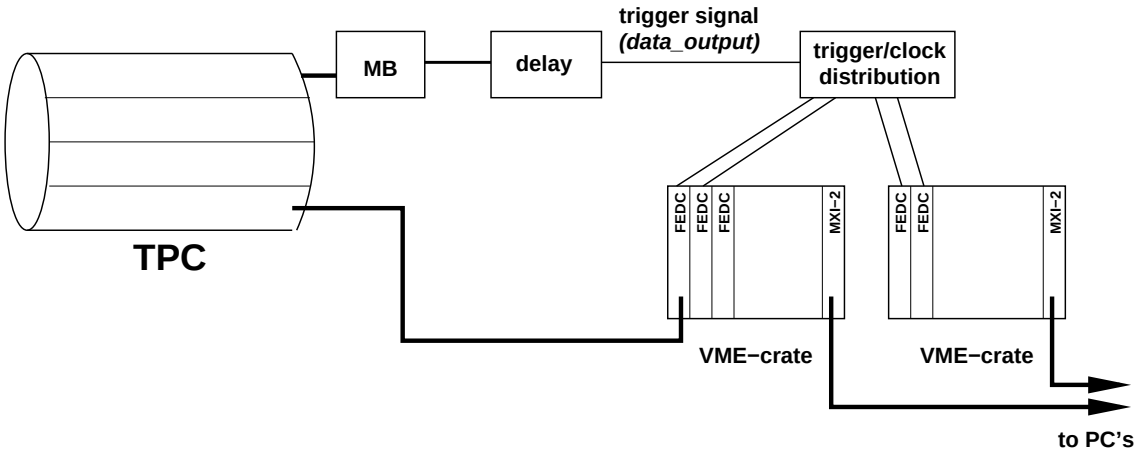

Figure 5.9: FEDC tigger distribution.

5.5 The MXI-2 Interface

The MXI-bus[4] is a high-performance communication link that interconnects devices using a flexible cabling scheme. MXI-bus is a general purpose, 32-bit multi-master system bus on a cable. It provides a high-performance way of controlling VXI[5] systems using commercially available desktop computers and workstations. MXI devices can directly access each other's resources by performing simple read and write operations to appropriate address locations. The MXI-2 standard expands the number of signals on a standard MXI cable by exporting all VXI backplane signals such as VXI triggers, interrupt lines and system clocks directly to the cabled bus.

A VXI device has a unique logical 8-bit address, which serves as a means of referencing the device in the VXI system and allows up to 256 VXI devices in a VXI system. Each VXI device must have a specific set of registers, called configuration registers. These registers are located in the upper 16 kbyte of the 64 kbyte A16 VME address space. The logical address of a VXI device determines the location of the device's configuration registers in the 16 kbyte area reserved by VXI.

Through the use of the VXI configuration registers the system can identify each VXI device, its type, model and manufacturer, address space, and memory requirements. VXIbus devices with only this minimum level of capability are called register-based devices. With this common set of configuration registers, the centralized *Resource Manager*, a software module, can perform automatic system configuration when the system is initialized.

In addition to register-based devices, the VXIbus specification also defines message-based devices, which are required to have communication registers in addition to configuration registers. All message-based VXIbus devices, regardless of the manufacturer, can communicate at a minimum level using the VXI-specified Word Serial Protocol. In addition, one can establish higher-performance communication channels, such as shared-memory channels, to take advantage of the VXIbus bandwidth capabilities.

The setup used in CERES consists of the VME FEDC-boards which are controlled by a PCI-VME bridge — the National Instruments VME-MXI-2 bus extender. This configuration consists of a PCI card (plugged in the so-called Readout-PCs), MXI-2 bus and a MXI-VME interface card. Data from the FEDCs are converted on the MXI-VME interface board and sent over the MXI bus, which is essentially the VME on a cable, into the PCI card. The maximal achieved data rate was about 12 Mbyte/s.

5.6 Software

The communication with the TPC-electronics is based on a VME processor running the OS9 operating system (FIC 8234 from CES). All parts of the readout electronics are configured via the VME-bus. For the beam-time of 2000 all programs were adapted to Linux and were running on a PC. The communication between the software on the PC and the hardware is based on a very simple client/server architecture (Fig. 5.10). The programs (clients) open a TCP/IP connection to the VME processor and send short commands to a server process. The server interpretes the

[4] **M**ultisystem e**X**tension **I**nterface
[5] **V**ME e**X**tensions for **I**nstrumentation

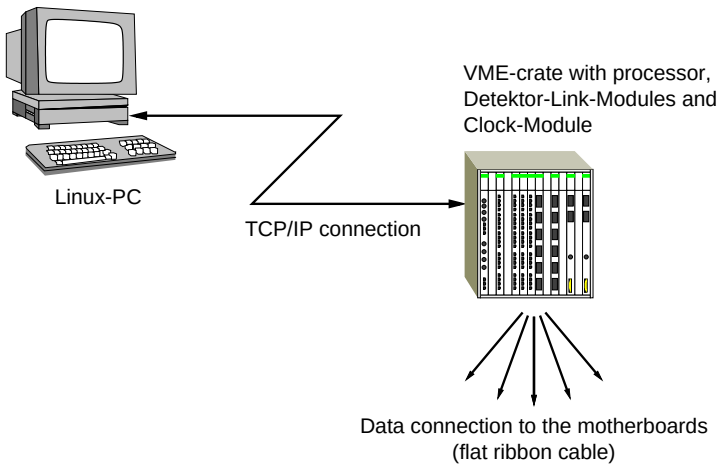

Figure 5.10: Client-server architecture of the TPC software.

commands and initiates a VME-bus access. In case of a read access the data are sent back to the PC using the established TCP/IP connection.

6 Reconstruction of the Raw Data

6.1 Data Set

In the framework of this thesis, data samples of Pb–Au collisions taken at beam energies of 40 AGeV, 80 AGeV, and 158 AGeV at the CERN SPS have been analyzed. The beam period of the year 1999 with $E_{\text{beam}} = 40$ AGeV was accompanied with severe problems in the readout system (see Chapter 5). Therfore, only a limited part of the TPC data could be used for the analysis presented in [71]. In the course of this thesis a reanalysis of this data set was done using the improved software for hit- and track-finding as well as the augmented knowledge about the calibration of the different detectors. To enhance the quality of the data sample only the information from readout chambers 0 and 1 was used. These two chambers have been the only ones which showed a stable and reliable performance of the readout.

The data at beam energies of 80 and 158 *A*GeV were taken during the beam time in 2000, the 80 *A*GeV data essentially in one night at the very beginning of the heavy ion run. At the time of the 80 *A*GeV run, the silicon drift detectors were not operational yet. During data taking with the full beam energy of 158 GeV all detectors were operational. To have a consistent analysis scheme for all beam energies only the data of the TPC have been used to determine the momentum of the tracks and to construct the two-particle correlation functions.

The analyzed data samples for all beam energies are summarized in Table 6.1.

6.2 Production: From Raw Data to ROOT-Trees

The goal of all data analysis is the extraction of meaningful numbers from the measured detector signals and their interpretation in terms of physics. Clearly, the data volume of the raw data, i. e. the data as recorded from the detectors, are much too bulky and difficult to handle. In addition, the data are not calibrated, which means that the data are not corrected for environmental changes like temperature, gas compositions, or known imperfections of the detectors. Therefore, the first step of data processing is the so-called *production*. In this time consuming process the compressed raw data are decompressed, the during data taking subtracted pedestal is reestablished (see page 47), measured ADC values are transformed into hits in the individual detectors, hits are grouped to tracks, and finally the momenta of the tracks are determined by a fit algorithm. As the output of the production a very limited number of parameters (e.g. coordinates of hits or tracks) are stored in the ROOT[1] tree format.

The processing of the raw data is done on a PC cluster at CERN running Linux, each PC having two processors. During the beam-time the data of all events belonging to one burst were

[1]The ROOT system is an Object Oriented framework for large scale data analysis developed at CERN.

$E_{beam} = 40$ *A*GeV			$E_{beam} = 80$ *A*GeV			$E_{beam} = 158$ *A*GeV		
run	bursts	No. events	run	bursts	No. events	run	bursts	No. events
781	7	5733	1114	33	11447	1270	43	14327
784	15	13454	1118	271	102102	1271	247	78432
786	10	8432	1119	206	72422	1272	266	92034
791	30	35067	1120	93	36128	1273	314	108705
792	115	158388	1121	55	19933	1274	362	125063
793	80	95777	1122	156	54298	1275	81	28410
796	262	270967	1123	129	49200	1276	329	112543
813	31	28808	1124	363	143241	1277	75	26471
816	9	9242				1279	57	7620
817	30	26928				1280	238	96112
818	165	138726				1281	150	61173
819	92	95699				1282	156	55713
820	17	16586				1284	71	29911
822	22	20924						
824	65	78628						
825	163	214167						
827	51	66253						
828	33	41980						
832	100	147966						
834	119	171626						
837	114	179773						
841	115	173181						
844	9	16568						
845	7	13254						
846	46	73523						
849	63	108562						
850	25	41618						
851	116	184462						
Total:		2436292	Total:		488771	Total:		836514

Table 6.1: Overview of the analyzed data samples at the three different beam energies.

collected in one binary file which was stored on tape at CERN's computer center. These files are the smallest data units which can be processed individually. To use the computer cluster as efficiently as possible an automatic load sharing tool (LSF) was used. This software takes care of the distribution of individual jobs to the PCs, ensuring a high and equal load of all available resources.

The production process is controlled by a few *Perl* scripts. An overview is given in Fig. 6.1. The main script controls the *staging* of the raw-data files. *Staging* means copying of data from tape to a disk pool. This disk pool is a collection of several data disks which are managed by the CASTOR system in a completely transparent way. The user does not have to know were exactly

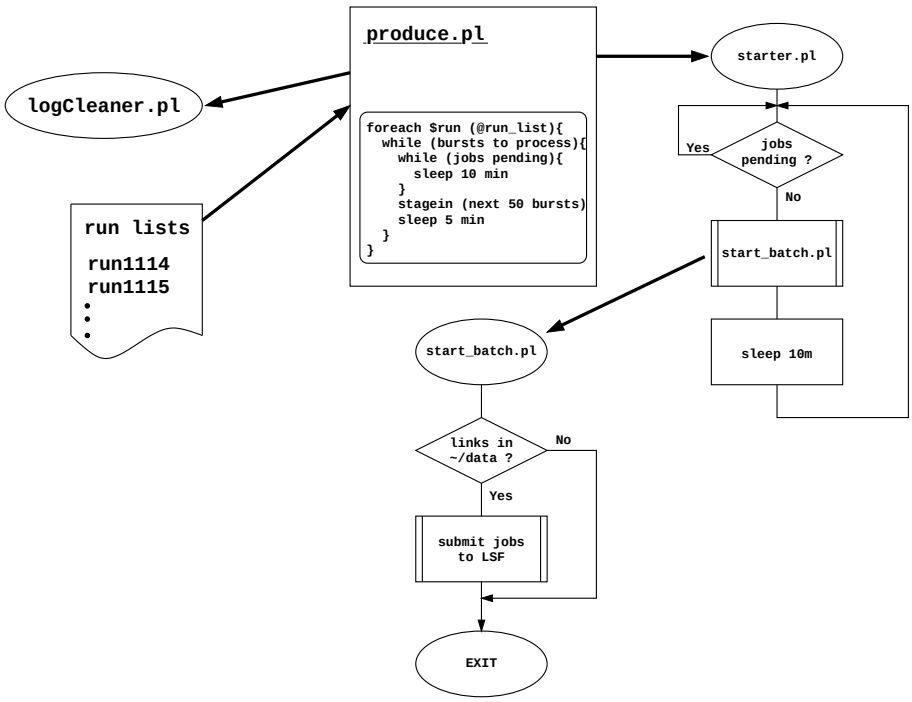

Figure 6.1: Production of the raw data is done in a automated way and controlled by simple *Perl* scripts.

the files are stored in this pool. A logical link created by the staging command gives access to the file. From a list containing all files which have to be processed, bunches of up to 100 files are chosen and requested for staging. The *Perl* script ensures that only files which are not already processed are read from tape. The *starter.pl* script is responsible for starting the individual jobs for processing of the raw data files. For each file copied to the disk pool a job is submitted.

CASTOR

During spring of 2000 all recorded data from the beam-time in 2000 were transfered to the new CASTOR system at CERN [72]. CASTOR stands for ***CERN Advanced STORage Manager*** and the project was started to handle the huge amount of anticipated data from the LHC[2] experiments in a fully distributed environment. CASTOR is an implementation of a so called *managed storage* system where users reference data through a logical name space rather than through explicit tape names and tape file sequence numbers. By using a command interface (the RFIO API)[3], access to remote files is identical to reading or writing to a local disk path.

When a program wants to access a CASTOR file, it first contacts the *CASTOR Name Server* and checks if the file exists. Afterwards the appropriate *stager* is contacted which checks if the file is already on disk and if not recalls the data from tape. The *stager* uses a memory resident catalog to maintain data of all disk files in the disk pool it manages. The files are copied on disks

[2] **L**arge **H**adron **C**ollider
[3] **R**emote **F**ile **IO** **A**pplication **P**rogram **I**nterface

which are managed by the *stager* and which establish the *disk pool*. As a last step a symbolic link to this file is created. The *CASTOR name server* maintains the logical name space. All files in the CASTOR system have an associated logical name entry in the name server. The name space is very similar to a UNIX directory structure. An entry in the name server contains information to locate the file on a specific tape, size of the file, access permissions, and others.

A small number of command line programs which are built on top of the RFIO API can be used to perform routine file and directory manipulations such as remotely copying, moving or renaming files.

6.3 The Reconstruction Chain

Reconstruction of the data means the transformation from raw detector data into meaningful physical information (e.g. information about hits or tracks of particles with their momenta). During this process the amount of data is reduced significantly. The main parts of this process are:

- calibration
- hit finding
- track finding
- track fitting

Essentially all software which is used in CERES is based on the COOL[4] library. COOL is a collection of C++ classes, varying from very simple classes like a momentum classes (`C3Momentum` and `C4Momentum`) to very sophisticated classes for finding and reconstructing hits or fitting momentum to a track (`CTPCHitFinder` or `CTPCTrackFitter`).

The first step in the the reconstruction chain is the unpacking of the detector data. For each detector the zero suppressed data are read from a binary file and the original time sequence of the signals which was lost during the data-reduction process in the readout-electronic is restored. The amplitudes and the time information of the pixels are filled into lists of the appropriate detector class (`CTPC`, `CRich1`,`CRich2`,`CSDC1`, `CSDC2`). All following analysis steps operate on these pixel lists. Figure 6.2 shows the different steps towards the ROOT tree for the TPC only. The ROOT output finally contains the extracted physical information necessary for further analysis. In the following sections the main parts of the reconstruction chain for the TPC are explained in more detail.

6.3.1 Hit Finding

After unpacking the raw data are searched for *hits*. A hit is characterized by a local maximum in the amplitude values of adjacent pads and time bins. The amplitude values of the TPC signals are stored in a two-dimensional array according to the pad and time coordinates. In a first loop local maxima in time direction are searched for each pad, followed by a search for local maxima in pad direction for each time bin. Only if the local maxima in time and pad direction are at the same location in the data array, this is considered as a local maximum which corresponds to a hit.

[4] **C**eres **O**bject **O**riented **L**ibrary

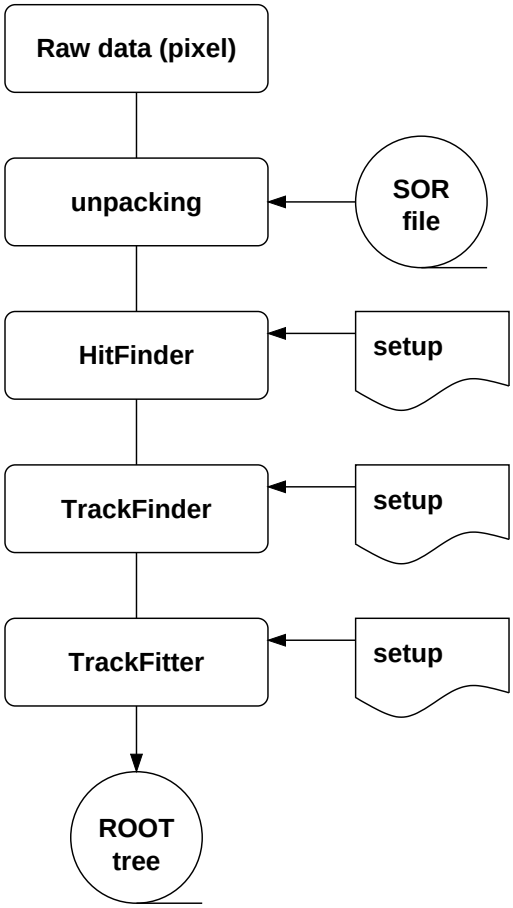

Figure 6.2: Schematic view of the different steps in the reconstruction chain. During unpacking, all information about the detector calibration is read from the **S**tart **O**f **R**un (SOR) file. The setup files contain data (e. .g. threshold values) which control the behavior of the analysis steps.

The criteria for a local maximum must be chosen in a way to ensure a certain tolerance against fluctuations on the signal. Otherwise every low amplitude peak originating from noise fluctuations would result in a hit.

After all absolute maxima are found, the positions of the hits are determined by calculating the center of gravity in time and pad direction respectively. For this calculation an area of 3 pads $\times$ 5 timebins (15 pixels, the so called *Hit-Area*) around the maximum of a hit is considered (see Fig. 6.3). If this area overlaps with another *Hit-Area* of a close-by hit, the hits are classified as overlapping and the calculation of the hit parameters needs more sophistication. A counter variable f_i, assigned to each pixel in the *Hit-Area*, is filled with the sum of the maximum amplitudes of all hits it belongs to. The values of these flags are used to weight the individual pixels during the

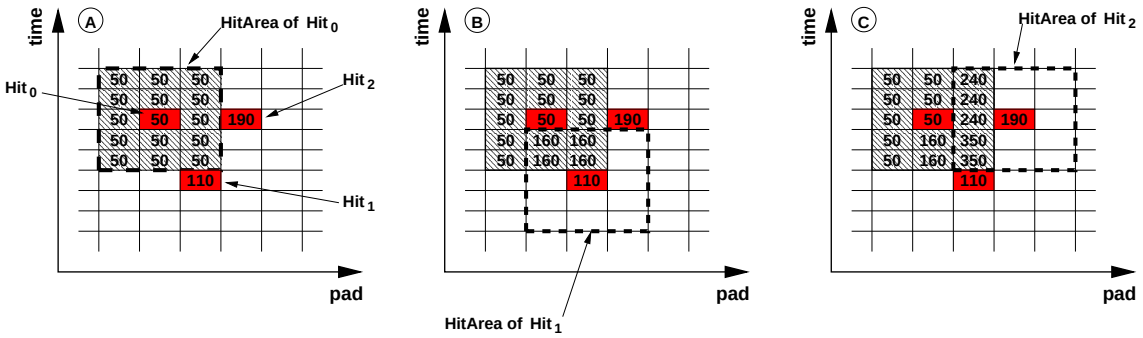

Figure 6.3: Example for the treatment of overlapping hits in the *HitFinder*. The flags in the *HitArea* of Hit_0 are filled with its maximum amplitude plus the maxima for the overlapping hits Hit_1 and Hit_2.

calculation of the center of gravity [73]:

$$\bar{t} = \frac{\sum_i A_i \cdot A_{\max 0} / f_i \cdot t_i}{\sum_i A_i \cdot A_{\max 0} / f_i} \tag{6.1}$$

$$\bar{\phi} = \frac{\sum_i A_i \cdot A_{\max 0} / f_i \cdot \phi_i}{\sum_i A_i \cdot A_{\max 0} / f_i} \,. \tag{6.2}$$

i is the index of the pixels in the 3 pads $\times$ 5 timebins area around a hit, A_i the value of the amplitude of pixel i, t_i and ϕ_i are the nominal positions in time- and ϕ-direction of the pixels. Figure 6.3 shows an example of three overlapping hits.

With the help of a lookup table the transformation from pad-time-plane coordinates into (x,y,z)-space coordinates of the hits is carried out. This table absorbs the whole transport process of the charge clusters in the electric and magnetic fields inside the TPC. It is obtained using a microscopic simulation of the drift process. The drift path of the primary charge clusters created by tracks passing through the TPC is calculated with the drift equation (3.7). Since $\vec{v}_d$ depends on $\vec{E}(\vec{x})$ and $\vec{B}(\vec{x})$ a precise knowledge of these fields is necessary in order to reconstruct the hit coordinates.

6.3.2 Track Finding

The task of the track finder is to combine *hits* to *tracks*. Each track inside the TPC is defined by a certain number of hits (up to 20), distributed over the 20 planes in z-direction.

The tracking starts from a so-called candidate hit with a z-position around the center of the TPC. This hit is combined with its two closest neighbors in z-direction to predict the sign of the track's curvature in ϕ-direction which is used to define a ϕ-window in which further hits are searched. Starting from the candidate hit the track is supplemented with hits on planes following in upstream and downstream direction. The ϕ-position of these hits is predicted with a linear extrapolation using the two previous hits. If no hit is found in a small window around this direction the procedure stops. In the following step the tracking software tries to find the still missing hits by fitting a polynomial of second order to the already found hits. The polynomial is used to predict the position of the hit on the next plane.

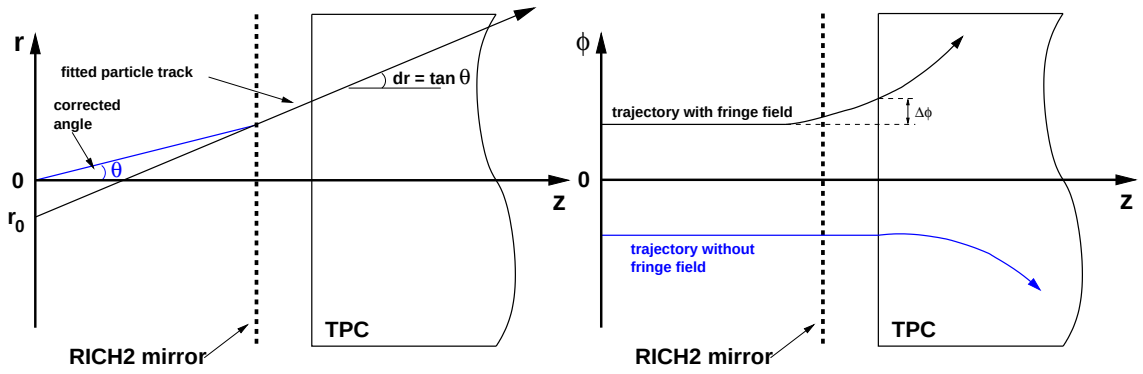

Figure 6.4: Momentum fit.

The tracking software is described in more detail in [74].

6.3.3 Track Fitting

The trajectory of a ionizing particle is defined by up to 20 hits in the TPC. Since the magnetic field is very inhomogeneous an analytical description of the trajectory is not possible and the determination of the particles' momentum is done using a two-dimensional fit based on reference tables. These tables contain the hit coordinates of particles with a fixed momentum of 1 GeV/c for different θ angles. The trajectories of these reference particles have been created using a simulation of the TPC based on the software package *Geant* [75].

The output of the fit procedure are the ϕ and θ angles of the trajectory and the magnitude of the momentum from which the Cartesian components p_x, p_y, and p_z are calculated. Due to the configuration of the magnetic field the deflection of charged particles is mainly in ϕ direction [59]. With this assumption, θ is obtained by fitting a straight line to the hits in the r-z plane. The results of this fit are the radial offset r_0 at the target and the slope of the track $\tan(\theta)$. For tracks coming from the target the distribution of r_0 should be centered around zero with a width which is given by the spatial resolution of the TPC and by multiple scattering. To correct for the influence of multiple scattering for tracks coming from the target it is assumed that all scattering happens in the RICH-2 mirror. This is reasonable because the mirror is the most massive material (its thickness is 4.7% of a radiation length) particles have to traverse (see Fig. 6.4, left).

The magnitude of the momentum as well as the ϕ angle and the slope of the track at the entrance of the TPC are obtained by fitting the hits in the ϕ-z plane with a reference track.

6.4 Momentum Resolution

The momentum resolution is determined by the spatial resolution of the detector as well as multiple scattering due to the detector material. The relative momentum resolution $\mathrm{d}p/p$ as a function of the momentum p can be parameterized as:

$$\left(\frac{\mathrm{d}p}{p}\right)^2 = \left(\frac{\mathrm{d}p}{p}\right)^2_{\mathrm{ms}} + \left(\frac{\mathrm{d}p}{p}\right)^2_{\mathrm{res}} \tag{6.3}$$

with the following assumptions:

$$\left(\frac{\mathrm{d}p}{p}\right)_{\mathrm{ms}} \propto \frac{1}{|\vec{B}|}\sqrt{\frac{1}{L \cdot X_0}} = \text{const.}, \tag{6.4}$$

$$\left(\frac{\mathrm{d}p}{p}\right)_{\mathrm{res}} \propto p \tag{6.5}$$

L is the measured track length and X_0 the radiation length. The formulas for the statistical part of the momentum resolution given in the literature [65, 76, 77] can not be applied directly to the CERES TPC. They are based on very specific assumptions concerning the setup and field configuration of the spectrometer. Nevertheless, it is possible to specify the momentum resolution in a quantitative way using a Monte-Carlo simulation of the detector. By comparing the reconstructed momentum of a simulated particle with its true momentum the resolution of the detector can be studied. Finally, the quality of the detector simulation is cross-checked by reconstructing the invariant mass of the Λ hyperon from its charged decay products p and π^-.

In addition to the statistical uncertainties of the momentum determination due to the finite local resolution and multiple scattering there are systematic distortions of the reconstructed hit positions. They are caused by the already mentioned problems at hit finding/reconstruction where the determination of the hit coordinates is based on the non-perfect knowledge of the drift properties inside the TPC (see page 70). It is due to these imperfections that the design resolution of the TPC has not yet been achieved (see below). However, since the measured hit residual distributions are used as input for the simulations, we expect to obtain a realistic estimate of the resulting momentum resolution.

6.4.1 Spatial Resolution

For a fixed geometry and magnetic field configuration the momentum resolution is mainly determined by the single hit position resolution. The spatial resolution of the TPC can be investigated by comparing the reconstructed hit positions with the ideal hit positions given by the fitted trajectory of a track. The width of the distribution of the differences between both positions, the so-called residual distribution, gives the spatial resolution. The spatial resolution can be decomposed into a radial component σ_r and a component in azimuthal direction σ_ϕ. Figure 6.5 shows the mean values together with the widths of the residuals as a function of the z-coordinate. Especially towards both ends of the TPC a significant deviation of the hits from the trajectory in radial direction is visible, caused by the still incomplete knowledge of the electrical field used in the reconstruction of the hit positions. The distortions in ϕ direction are due to the imperfect consideration of the magnetic and electric fields, gas properties such as mobility, geometry of the TPC, and the Lorentz-angle. The accurate determination of these values are under way but not yet included in this analysis. At this present intermediate stage of calibration the mean spatial resolution (integrated over all z positions and radii) is:

$$\begin{aligned} \sigma(\Delta r) &\approx 930\ \mu\mathrm{m} \\ \sigma(\Delta\phi) &\approx 520\ \mu\mathrm{rad}. \end{aligned}$$

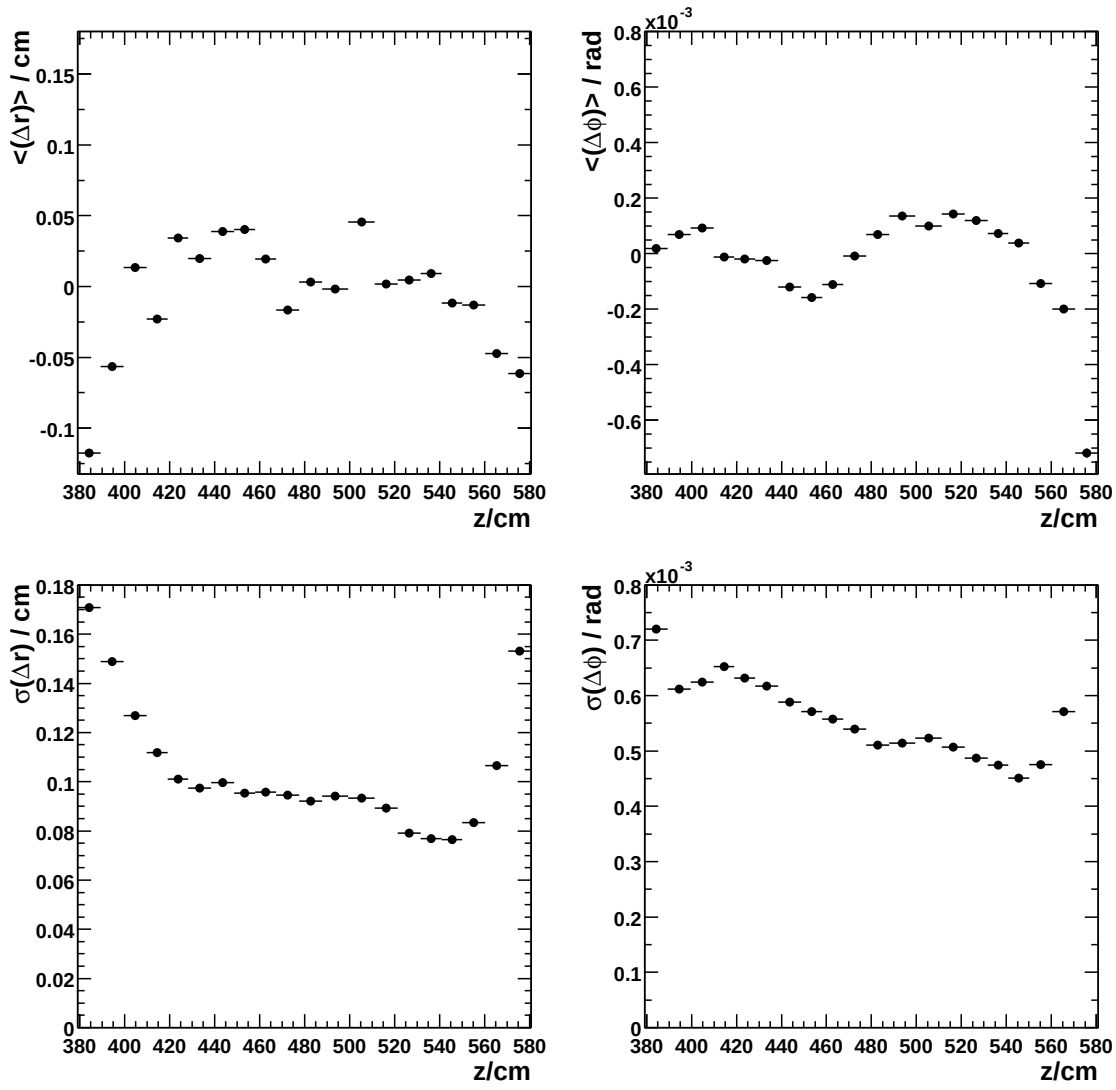

Figure 6.5: Residuals of the track fit for runs at beam energy of 158 *A*GeV with magnetic field.

This has to be compared with the design values

$$\begin{aligned} \sigma^{\text{design}}(\Delta r) &\approx 600 - 700\ \mu\text{m} \\ \sigma^{\text{design}}(\Delta\phi) &\approx 200 - 300\ \mu\text{rad} \end{aligned}$$

which are significantly better.

6.4.2 Momentum Resolution from Monte-Carlo Simulations

As already mentioned, a Monte-Carlo simulation of the detector is used to determine the momentum resolution. In order to do this, the simulation has to describe the detector with good precision.

All imperfections in the reconstruction of the hits due to the insufficient knowledge about the drift properties at the present stage of the calibration have to be implemented. This can be achieved by tuning the simulation according to the distributions obtained from the analysis of real data, e. g. the deviation of the reconstructed hit positions from the fitted trajectory (the hit residuals), as shown in Figure 6.5, have to be considered. This was done by by smearing the r and ϕ coordinates of each reconstructed hit according to the experimentally obtained distribution.

By comparing the real momentum of a particle with its reconstructed one the momentum resolution as a function of momentum is obtained. The result is shown in Figure 6.6. According to Eq. (6.3) the resolution can be parameterized as

$$\left(\frac{\mathrm{d}p}{p}\right) = \sqrt{0.021^2 + (0.022 \cdot p)^2}, \tag{6.6}$$

where the momentum p is given in units of GeV/c. For values of $p < 1$ GeV/c the parameterization deviates significantly from the simulation. The reason for this are inconsistencies in the Monte-Carlo simulation of the TPC which lead to momentum offsets at small values of p. These offsets are different for positive and negative tracks.

Compared to the design resolution

$$\left(\frac{\mathrm{d}p}{p}\right)_{\mathrm{design}} = \sqrt{0.01^2 + (0.01 \cdot p)^2} \tag{6.7}$$

the present momentum resolution is still about a factor two worse but consistent with the observed averaged global width of the hit residuals (see Fig. 6.5) which is largely affected by remaining distortions of the drift field. However, the local single hit spatial resolution is consistent with the design goal so that the expectation is that after finishing the various calibration issues a result close to the design resolution will be reached.

6.4.3 Reconstruction of the Λ Hyperon

In order to check the reliability and precision of the TPC Monte-Carlo simulation it is useful to reconstruct the decay of particles and to compare the reconstructed invariant mass $m_{\mathrm{inv}} = \sqrt{(\mathbf{p}_1 + \mathbf{p}_2)^2}$ with the result obtained by the simulation. For this purpose the decay of the neutral Λ hyperon was investigated.

The neutral Λ-hyperon is reconstructed using its charged decay products. The considered decay mode with a branching ratio of about 64% is

$$\Lambda \rightarrow \mathrm{p}\ \pi^-.$$

The invariant mass is reconstructed by combining all positive tracks with all negative tracks measured in the TPC in one event, resulting in the signal mass distribution S. This procedure leads to a large combinatorial background. To evaluate the shape of this background accurately an event-mixing method is used. Positive tracks from one event are combined with negative tracks of a different event. These combinations contain no real Λ decays and describe the background very well. The normalized background distribution B is subtracted from the signal distribution S to obtain the invariant mass spectrum:

$$M = S - N \cdot B. \tag{6.8}$$

The normalization constant N is extracted from the signal-free region in the invariant mass spectrum ($1.15 < m_{\mathrm{inv}} < 1.2$ GeV/c^2).

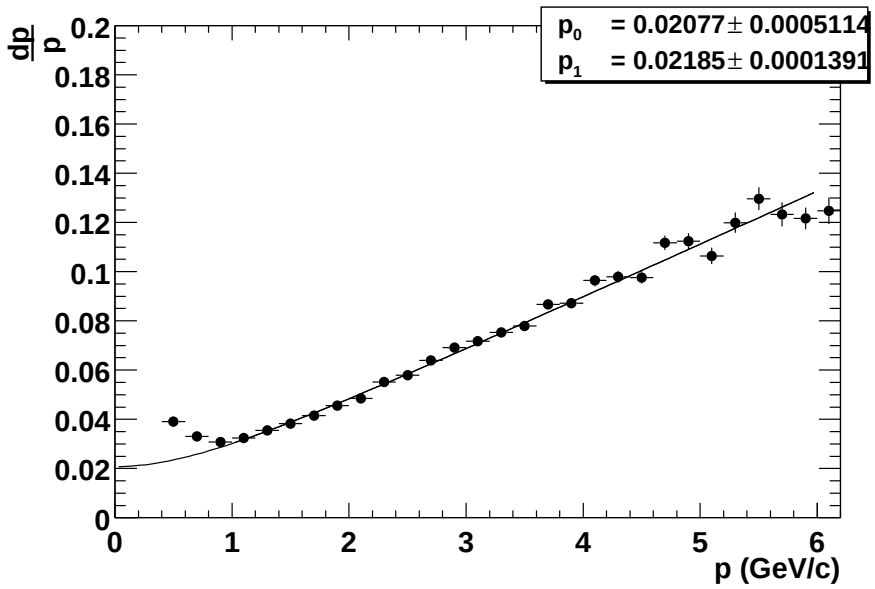

Figure 6.6: Momentum resolution of the TPC.

Reconstruction of Secondary Vertex and Fringe Field Correction

The main problem in reconstructing secondary particles from their decay products is the discrimination of the huge combinatorial background. For the Λ with a mean life time of $(2.632 \pm 0.020) \times 10^{-10}$ s or a mean decay length of 7.89 cm (in the rest frame of the particle) [26] a very efficient tool to reject the background is a cut on the *z*-position of the reconstructed decay vertex. Due to the Lorentz boost of the produced particles the decay length in the lab frame is much longer, thus the decay vertices of the majority of produced Λ hyperons are well separated from the target. The transformation of the decay length into the lab frame is given by:

$$c\tau_{\text{lab}} = \gamma\beta \cdot c\tau. \tag{6.9}$$

Assuming $\gamma\beta \approx 5$, the mean decay length in the lab frame is about 40 cm. Requiring a minimum distance of 50 cm between target and reconstructed vertex of the Λ decay, target tracks can be efficiently suppressed.

The decay vertex is found by calculating the *point of closest approach* of two trajectories by back-extrapolating the measured momentum vectors of the particles from the entrance of the TPC towards the target. In order to do this, the tracks are parameterized using the measured θ and ϕ_{TPC} angles (ϕ_{TPC} is the track angle at the entrance of the TPC) as well as the position where the track enters the TPC (for the coordinate system of the TPC see Figure 3.6). For non-target tracks $\phi(z)$ and $\theta(z)$ are not constant even in the field free region. Therefore, the slope $\mathrm{d}\phi/\mathrm{d}z$ of the track at the entrance of the TPC is needed as additional information for the back-extrapolation. The entrance position of the track as well as θ, ϕ_{TPC} and the slope $\mathrm{d}\phi/\mathrm{d}z$ are results of the track fitting procedure.

For particles originating from the target, neglecting the influence of multiple scattering, $\phi(z)$ is constant as it traverses the spectrometer until it reaches the TPC where the radial component of the

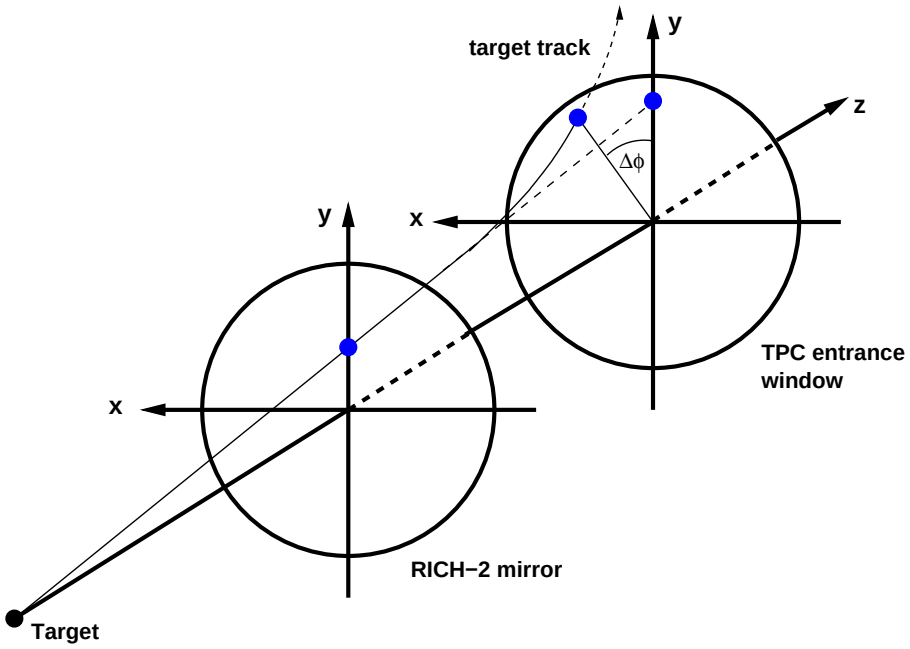

Figure 6.7: Effect of the fringe field on tracks. The remnant magnetic field in front of the TPC entrance window is bending charged particles in ϕ direction. $\phi(z)$ is no longer constant and the particles enter the TPC with some slope $\mathrm{d}\phi/\mathrm{d}z$.

magnetic field starts to bend its trajectory. However, due to the magnetic fringe field in front of the TPC the particle is already deflected before it enters the TPC and $\phi(z)$ varies with the increasing z-coordinate of the particle, see Figures 6.7 and 6.8 . This effect is irrelevant for target tracks since ϕ is measured with the silicon detectors. For secondary charged particles, produced downstream of the silicon detectors, the effect of the fringe field becomes more severe. The reconstruction of the decay vertex strongly depends on ϕ_{TPC} and $\mathrm{d}\phi/\mathrm{d}z$ at the entrance of the TPC (both are given by the track fit) which are affected by the fringe field.

To correct for the effect of the fringe field, its influence on target tracks has been studied. Because by far most of the reconstructed tracks in an event are due to particles produced at the main interaction vertex all tracks of an event are assumed to be target tracks. To quantify the deflection caused by the fringe field, ϕ_{TPC} and the slope $\mathrm{d}\phi/\mathrm{d}z$ have been used to calculate with a linear extrapolation the corresponding ϕ value at the arbitrarily chosen position of the RICH-2 mirror. The difference $\Delta\phi = \phi_{\text{RICH-2}} - \phi_{\text{TPC}}$, which should be zero without fringe field (which means $\mathrm{d}\phi/\mathrm{d}z = 0$), is shown in Figure 6.9 as a function of the inverse momentum of the track. Assuming that the influence of the fringe field is the same for target and non-target tracks the parameterization of $\Delta\phi$ by a straight line is used to correct each track (also non-target tracks) according to its momentum.

Invariant Mass Spectrum

Fig. 6.10 shows the reconstructed invariant mass spectrum of the Λ as obtained by a Monte-Carlo simulation (solid line) and by the analysis of data (black circles), normalized with respect to the

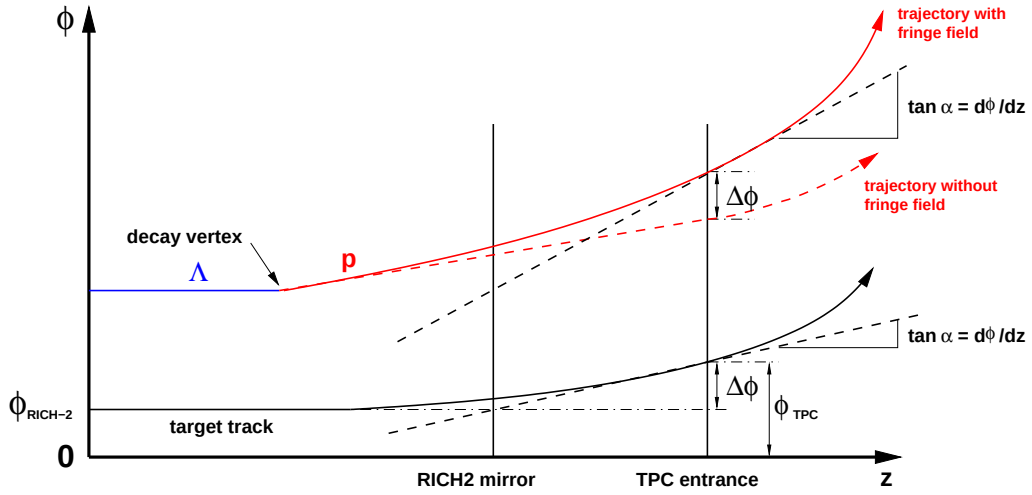

Figure 6.8: Effect of the fringe field on target tracks and tracks coming from secondary vertices (in this case from the decay of a Λ), both with the same momentum. The measured $\Delta\phi$ for the target track is also used to correct the trajectory of the secondary particle.

peak value. For both analysis the same cuts have been used. The spectra are fitted by a Gaussian with the following results:

$$\text{Data:}\quad \overline{m}_\Lambda = 1.114\,\text{GeV}/c^2 \qquad \text{Monte-Carlo:}\quad \overline{m}_\Lambda = 1.1086\,\text{GeV}/c^2$$
$$\sigma = 10.65\,\text{MeV}/c^2 \qquad\qquad \sigma = 7.37\,\text{MeV}/c^2$$

The mean values of the Λ masses differ by about 0.4%. The value obtained by analyzing data is in good agreement with $m_\Lambda = 1.115683\,\text{GeV}/c^2$ quoted in literature [26] while the value obtained with the Monte-Carlo simulation differs from the literature value by 7 MeV. This points again to the fact that the Monte-Carlo at its present stage does not describe the experimental setup with high precision (see above).

However, the absolute mass/momentum scale is not crucial for the HBT analysis. There, the correlation function is determined by the momentum difference of two particles and therefore an offset in the momentum becomes balanced. The mass resolution, reflected in the width of the Gaussian, differs by about 3 MeV/c^2.

As one can see, the agreement of simulations and data is not perfect. This points to the fact that the used Monte-Carlo simulation does not describe the experimental situation in full detail. Including the hit residuals in order to emulate the incomplete stage of the calibration of the drifting charge clusters (see page 70) may not be sufficient. Another problem which is inherent to the usage of the Λ as a probe for the mass resolution is the determination of the opening angle of the decay. The reconstructed invariant mass does not only depend on the single particle momenta and its uncertainties but also on the opening angle of the decay, on his part strongly influenced by the fringe field and its correction. This speaks in favor of using a decay with a shorter lifetime, e. g. the decay

$$K_s^0 \rightarrow \pi^+\pi^-$$

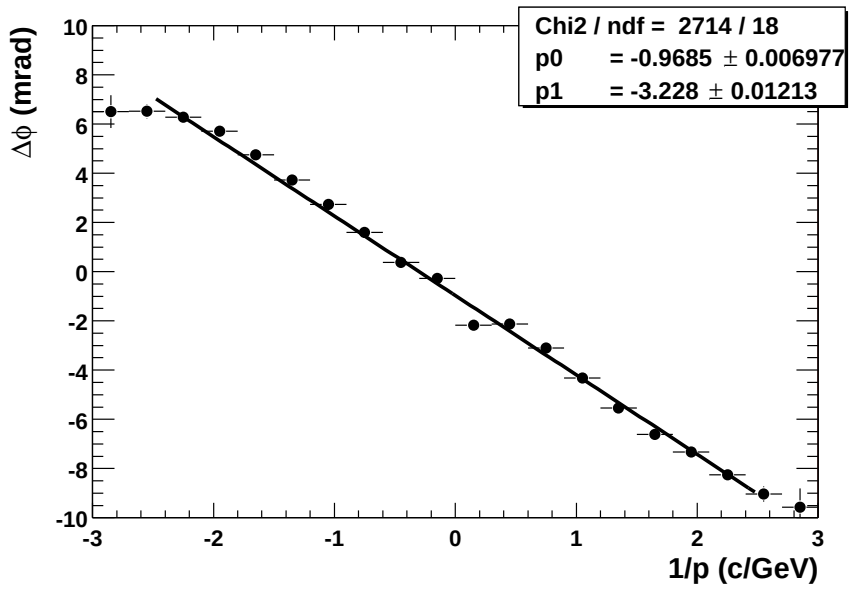

Figure 6.9: Influence of the fringe field on target tracks. Shown is the deflection $\Delta\phi$ as a function of the inverse momentum. $\Delta\phi(p^{-1})$ is parameterized by a polynomial of first order.

with a mean decay length of 2.676 cm [26]. Due to the short decay length a big fraction of the K_s^0 decay between target and silicon detectors. Their decay products can be tracked by the silicon detectors, superseding the fringe field correction. However, this approach needs a modified version of the silicon software in order to allow for the reconstruction of secondary vertices which was not yet available.

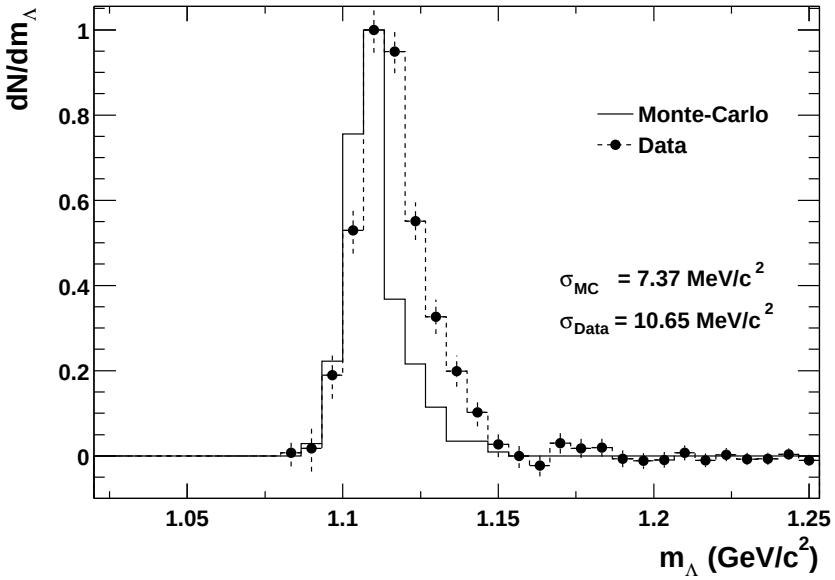

Figure 6.10: Invariant mass spectrum of the Λ. Shown are the results of a Monte-Carlo simulation of the TPC (solid line) and the mass spectrum as reconstructed from data (points and dashed line).

7 HBT Interferometry Analysis

The analysis of Bose-Einstein momentum correlation of identical particles provides an ideal tool to gain insight into the space-time evolution as well as the existence of a collective velocity field at the time of thermal freeze-out of a particle emitting source, created in ultrarelativistic collisions of heavy ions [50, 78]. This chapter gives a detailed description of the different analysis steps in order to obtain the correlation function and consequently the source parameters. In the context of this thesis correlations of like-sign pion pairs have been studied. The three-dimensional correlation function C_2, depending on the relative momentum components of the particle pair, was parameterized using a three-dimensional Gaussian, modified to consider the final state Coulomb interaction. The parameterization was done in the Cartesian *out-side-long* system [40, 41]. The three components of the relative pair momentum were determined in the **L**ongitudinally **C**o **M**oving **S**ystem (LCMS) of the pair, the longitudinal rest frame of the pair.

7.1 Multiplicity and Event Selection

The evolution of a heavy ion reaction strongly depends on the centrality of the collision. The centrality is determined by the impact parameter: the more central a collision, the smaller the impact parameter. For a detailed analysis of the reaction process the events have to be classified according to their centrality and analyzed separately. Practically, the direct measurement of the impact parameter is not possible, thus the multiplicity of charged particles created in the collision is used as a measure for the centrality of the reaction.

For the data taken during the beam-time in 1999 the number of tracks in the silicon detectors were used to classify the centrality of a reaction whereas in 2000 the MC detector was used for this purpose. The distributions of silicon tracks per event and the ADC value of the MC detector are shown in Figure 7.1. A detailed detector simulation with events generated by the UrQMD event generator allows to relate the number of charged particles (as measured in the SDD or MC) to the centrality of the reaction, expressed as fraction of the total cross section. The result of the simulations are shown in Figure 7.2 together with the classification of the used multiplicity bins.

Compared to previously shown distributions of the number of tracks in the silicon detectors the present one shown in Figure 7.1 is shifted towards lower values. The reason for this is the usage of a different set of calibration values for the silicon detectors in the production of the 40 *A*GeV data used in this thesis, leading to the loss of tracks by a factor of 1.22. The cut values defining the centrality bins needed to be scaled accordingly.

The knowledge of the impact parameter $|\vec{b}|$ together with a model of the collisions allows to obtain the number of nucleons participating in the collision. The model used herein was introduced by Eskola [80] and describes a nucleus-nucleus collision in terms of binary collisions between nucleons. Nuclear density distributions of the two colliding nuclei are used to calculate the number

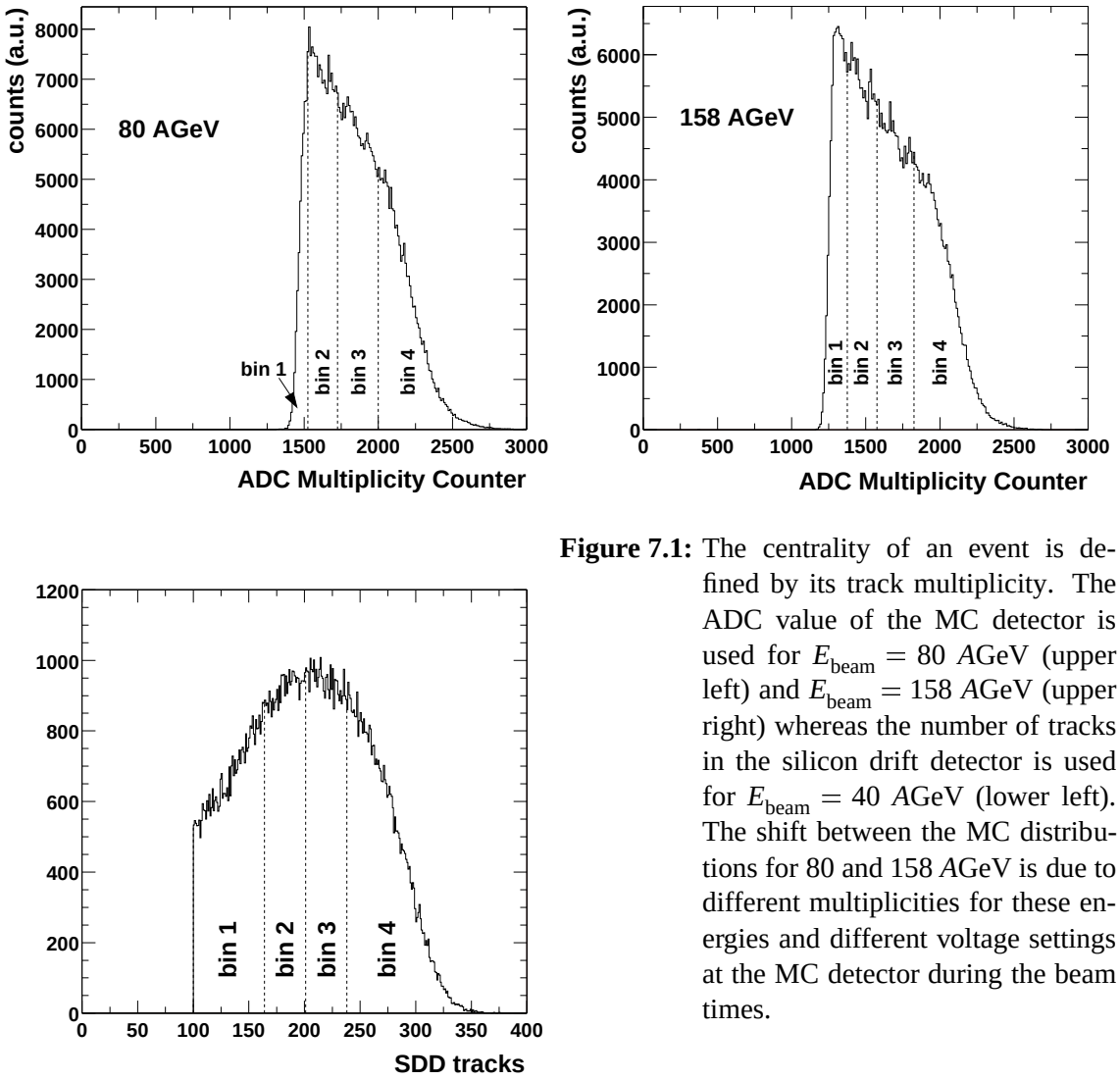

Figure 7.1: The centrality of an event is defined by its track multiplicity. The ADC value of the MC detector is used for $E_{\text{beam}} = 80$ *A*GeV (upper left) and $E_{\text{beam}} = 158$ *A*GeV (upper right) whereas the number of tracks in the silicon drift detector is used for $E_{\text{beam}} = 40$ *A*GeV (lower left). The shift between the MC distributions for 80 and 158 *A*GeV is due to different multiplicities for these energies and different voltage settings at the MC detector during the beam times.

of participating nucleons and the number of binary collisions as a function of the impact parameter. The nuclear density distribution is described by a Woods-Saxon function

$$\rho_A(r) = \frac{1+\rho_0}{1+\exp((r-R_A)/z)}, \tag{7.1}$$

where R_A is the nuclear radius at half central density and z the surface thickness. The values used are:

$$\rho_0 = 0.17\ \text{fm}^{-3}, \tag{7.2}$$

$$R = (1.12\,A^{1/3} - 0.86\,A^{-1/3})\ \text{fm}, \tag{7.3}$$

$$z = 0.54\ \text{fm}. \tag{7.4}$$

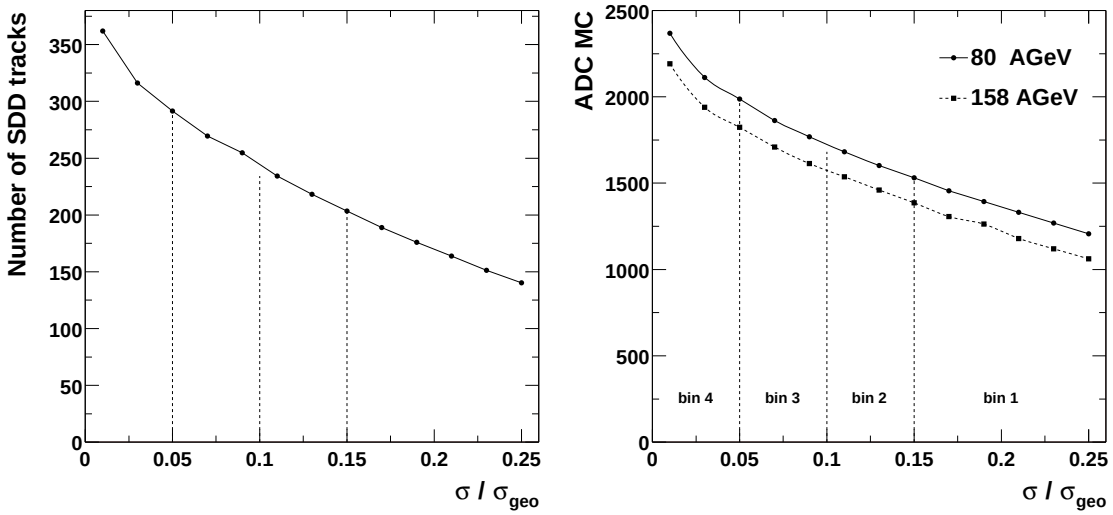

Figure 7.2: The number of SDD tracks and the ADC value of the MC detectors as a function of the centrality. The curves are obtained with the help of a detector simulation [79].

The central density ρ_0 is obtained by the normalization condition

$$\int_0^\infty \rho_A(r)\, d^3r = A. \tag{7.5}$$

Within this model participants are defined as nucleons which have encountered at least one binary collision. The mean number of participants in an $A+B$ collisions at an impact parameter $\vec{b}$ is given by:

$$N_{AB}(\vec{b}) = \int d^2s\, T_A(\vec{s}) \left(1 - \left(1 - \frac{\sigma_{NN} T_B(\vec{s}-\vec{b})}{B}\right)^B\right) \tag{7.6}$$

$$+ \int d^2s\, T_B(\vec{s}) \left(1 - \left(1 - \frac{\sigma_{NN} T_A(\vec{s}+\vec{b})}{A}\right)^A\right). \tag{7.7}$$

σ_{NN} is the inelastic NN cross section in milli barn. The value used is $\sigma_{\mathrm{NN}} = 30$ mb. The factors of the two integrals represents the probability for a nucleon to pass through the nucleus without any collision:

$$P(0) = \left(1 - \frac{\sigma_{NN} T_B(\vec{b})}{A}\right)^A. \tag{7.8}$$

The probability of becoming a participant is given by

$$1 - P(0) = 1 - \left(1 - \frac{\sigma_{NN} T_B(\vec{b})}{A}\right)^A. \tag{7.9}$$

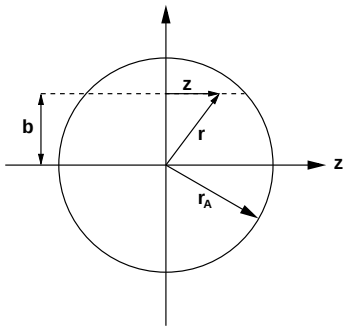

Figure 7.3: The thickness function.

The integrated density function along a path parallel to the beam axis z at a distance $|\vec{b}|$ is called the *thickness function* $T_A(b)$ (cf. Fig.7.3):

$$T_A(b) = \int_{-\infty}^{\infty} \rho_0(\sqrt{b^2+z^2})\,\mathrm{d}z \tag{7.10}$$

The product $T_A(b) \cdot \sigma_{NN}$ can be interpreted as the number of binary collisions encountered by a nucleon passing through a nucleus at impact parameter $\vec{b}$.

The definition of the centrality bins with the corresponding number of participants are summarized in Table 7.1. The determination of these numbers neglects fluctuations in $|\vec{b}|$ for a given value of $\sigma/\sigma_{\mathrm{geo}}$.

bin	$\sigma/\sigma_{\mathrm{geo}}$	$b_{\mathrm{min}} - b_{\mathrm{max}}$	$\langle N_{\mathrm{part}} \rangle$	N_{ch} cut	MC cut	
				40 AGeV	80 AGeV	158 AGeV
1	15-19%	5.8-6.5	202	100-164	< 1525	< 1375
2	10-15%	4.7-5.8	236	164-201	1525-1725	1375-1575
3	5-10%	3.3-4.7	287	201-238	1725-2000	1575-1825
4	$< 5\%$	< 3.3	347	> 238	> 2000	> 1825

Table 7.1: Definition of centrality bins for the analyzed energies.

7.2 Track Selection

For the construction of the correlation function only tracks which passed certain quality cuts are used. A momentum dependent cut on the energy loss $\mathrm{d}E/\mathrm{d}x$ in the TPC was utilized to enrich the pion sample by rejecting part of the electron and proton contamination. Another criteria applied for tracks was their length, expressed by their number of hits. Only tracks with 14 or more hits were considered. Figure 7.4 shows the track length distribution for all beam energies. The loss of long tracks at 40 *A*GeV reflects the problems of the at that time not properly working readout electronics, resulting in the fact that most tracks could not be detected in all of the 20 planes of the TPC. Due to the preliminary status of the calibration of the data samples at 80 *A*GeV and

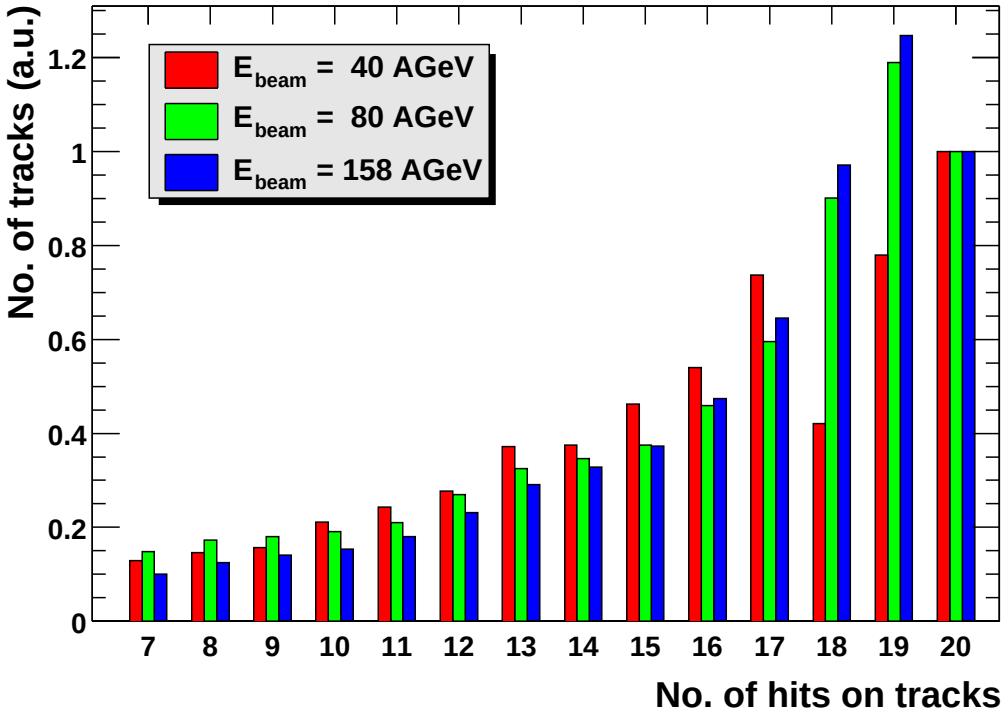

Figure 7.4: Distribution of track lengths, measured in number of hits. The distributions for the different beam energies are arbitrarily normalized to 1 at a track length of 20 hits.

158 *A*GeV no further cuts on the track quality were applied. For the reanalyzed data at 40 *A*GeV beam energy the calibration was much more advanced and done on a run-by-run basis. To suppress non-target tracks, a cut on the track offset r_0 at the target was used. Only tracks with $|r_0| < 4$ cm were accepted. Figure 7.5 shows the corresponding distributions.

Due to the finite granularity of the TPC trajectories with a very small distance between them can not be resolved. This results in a dependence of the reconstruction efficiency on the two-track separation. The two-track distance on the other hand is correlated with the difference in momentum of the two tracks and therefore the reconstruction efficiency depends on the momentum difference, generally leading to smaller efficiencies for small momentum differences, which may affect the HBT analysis.

The two-particle correlation function is experimentally defined as the ratio of the *signal* momentum difference distribution to the *background* momentum difference distribution. The signal distribution is obtained by combining like-sign particles from the same event, the background distribution by mixing particles from different events. Due to the dependence of the reconstruction efficiency on the track separation, the signal distribution is strongly influenced at small distances/momenta while the background distribution is not. This leads to distortions of the correlation function. To avoid this effect, pairs with small opening angles (synonymic with a small distance) are rejected in the signal and background distribution.

Figure 7.6 shows the reconstruction efficiency as a function of the opening angle between the

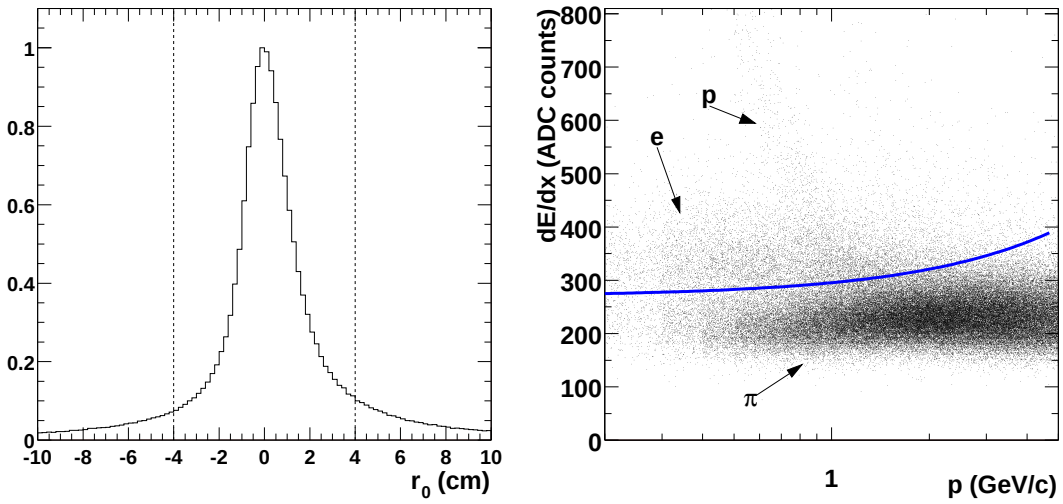

Figure 7.5: Track selection cuts for $E_{\text{beam}} = 40\,A\text{GeV}$. Left: track offset r_0 at target. Right: energy loss $\mathrm{d}E/\mathrm{d}x$. The applied cut are indicated by the lines.

two particles of a pair. The efficiency is obtained by dividing the opening angle distribution of pairs from the same event by a reference distribution, created by mixing pairs of different events. The flat part of the resulting distribution at large opening angles is used to normalize it to unity. For comparison, Figure 7.6 shows the two-track reconstruction efficiencies obtained by using the track angles measured in the TPC and the resolution obtained after matching track segments in the silicon detectors with TPC track segments and using the angles measured by the silicon detectors. The peak at zero for the SDD-TPC tracks is an effect of the track matching procedure. During matching, each track segment in the TPC is associated with the closest track segment in the silicon detectors. Because the angular resolution of the TPC is better due to its larger distance from the target and its higher granularity (360 anodes on the circumference of the silicon drift detectors compared to 768 pads in one plane of the TPC) it can happen that two or more TPC segments are combined with the same SDD segment. The reconstruction efficiency for the TPC is almost flat down to opening angles of 8 mrad whereas the efficiency for the SDD already starts to deviate from unity at 10 mrad. Again, this difference is an effect of the two different granularities of both detectors.

Since for all three analyzed beam energies only track angles measured with the TPC are used, only pairs with opening angles larger than 8 mrad were used for the signal and the background.

7.3 The Experimental Correlation Function

7.3.1 Construction of the Correlation Function

The two-particle correlation function C_2 of identical particles is defined as the probability to find a particle pair with momenta $\vec{p}_1$ and $\vec{p}_2$ divided by the product of the probabilities to find single particles with the same momenta (see Eq. (2.10)). Experimentally, this is given by the ratio of a

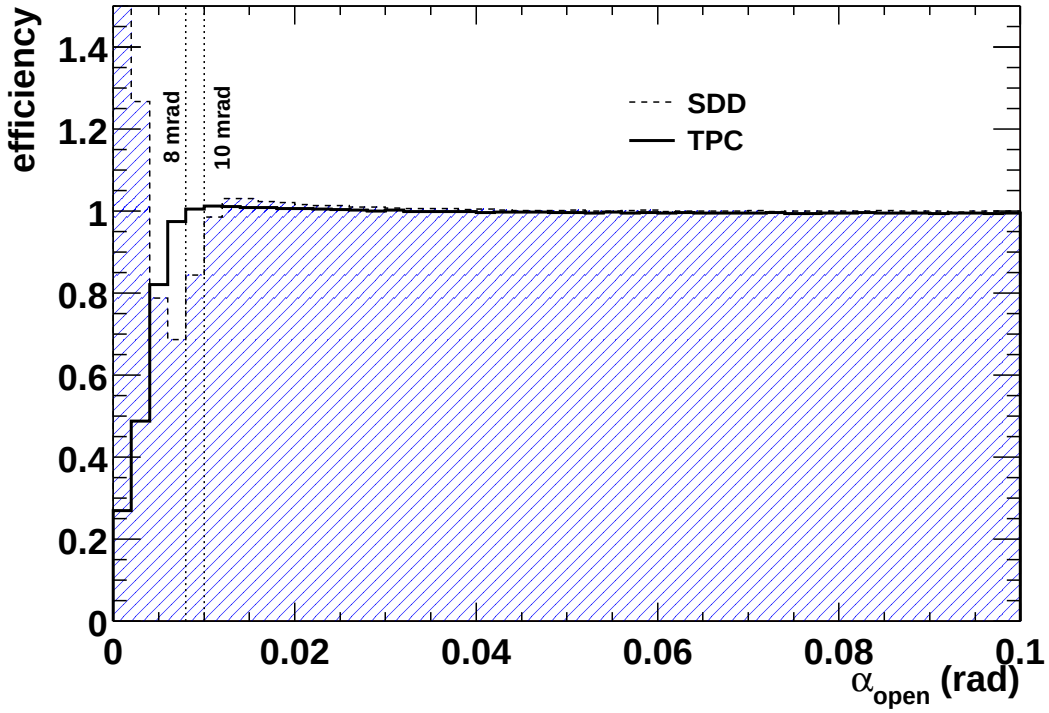

Figure 7.6: Two-track resolution of the TPC and the SDD as a function of opening angle.

so-called signal distribution S and a background distribution B:

$$C_2 = \frac{S}{B}. \tag{7.11}$$

S and B are three-dimensional distributions, according to the q_l-q_s-q_o components of the momentum difference of the pair (see Section 2.4). While the signal distribution is obtained by combining particles of the same event, the background distribution is constructed by combining particles of different events. The background distribution obtained in this way is free of Bose-Einstein or other correlations at small momentum differences[1] and determined only by the single particle phase-space distributions. It represents a uncorrelated reference distribution. The correlation function given by (7.11) is unnormalized since the background distribution is usually evaluated for a much larger sample. The normalization to unity at large relative momenta of the pair is included in the fit of the Bertsch-Pratt parameterization (see below).

In order to explore the dynamical behavior of the particle emitting source the HBT analysis has been performed in well defined bins of pair rapidity $y_{\pi\pi}$ and mean transverse pair momentum $|\vec{k}_\perp|$ as defined by (1.7) and (1.8). Figure 7.7 shows the $y_{\pi\pi} - p_\perp$ distribution of all reconstructed particle pairs assuming the pion mass for evaluating E_i. Also shown are the bins in $k_\perp$ and the values of midrapidity for the three different beam energies. The analyzed rapidity regions are:

[1] This depends on the details how the background sample is created. Residual correlations in the background are small and will not be discussed here.

E_{beam}	$y_{\pi\pi}$ range
40	-0.25< $(y_{\pi\pi} - y_{\text{mid}})$ <0.25
80	-0.5< $(y_{\pi\pi} - y_{\text{mid}})$ <0
158	-1.0< $(y_{\pi\pi} - y_{\text{mid}})$ <-0.5

$k_\perp$-bin	bin 1	bin 2	bin 3	bin 4	bin 5
$k_\perp$ (GeV/c)	0-0.15	0.15-0.25	0.25-0.35	0.35-0.45	>0.45
$\overline{k_\perp}$ (GeV/c)	0.128	0.197	0.293	0.392	0.548

Table 7.2: The different $k_\perp$ intervals used in the analysis and their mean value.

For each $k_\perp$ bin the mean value $\overline{k_\perp}$ was determined by projecting the $k_\perp - y_{\pi\pi}$ distribution of pairs with $q_{\text{inv}} < 60$ MeV on the $k_\perp$ axis and calculating the mean value of each $k_\perp$-bin. The resulting values, shown in Table 7.2, are used for the representation of the HBT parametes vs. $k_\perp$ in the following chapters.

For each particle pair the components q_l, q_s, and q_o of the momentum difference are calculated and filled into a three-dimensional array with a binning of 10 MeV/c. In a second three-dimensional array of same granularity the momentum difference q is stored. This information allows to determine the average q for each of the q_l, q_s, q_o bins and is used during the fit of the correlation function to account for the final state Coulomb interaction.

7.3.2 Extracting Source Parameters from the Two-Particle Correlation Function

To obtain the HBT radii for each bin in $k_\perp$ and $y_{\pi\pi}$ the three-dimensional correlation function C_2 has to be fitted with the Bertsch-Pratt parameterization (2.38) discussed in Chapter 2:

$$C_2(q_s, q_o, q_l) = N \cdot \left(1 + \lambda \cdot \exp\left(-q_s^2 R_s^2 - q_o^2 R_o^2 - q_l^2 R_l^2 - 2 q_o q_l R_{ol}^2\right)\right), \tag{7.12}$$

with N as a normalization factor. The additional parameter λ (the so-called chaoticity parameter) was introduced to describe the coherence of the particle source. Only for a totally chaotic particle emission the value of this parameter is unity [81]. Experimentally, the λ parameter is also influenced by the decay of long-living resonances (which can usually not be resolved), by the momentum resolution, and by the contamination of the signal distribution with particle pairs in which at least one particle is not a (primary) pion.

As explained in Section 2.5, the two-particle correlation function has to be corrected for final state interactions of which the Coulomb interaction is the most important one. Correlations among like-sign charged pions occur not only due to Bose-Einstein statistics, but also because of final state Coulomb repulsion. Traditionally, Coulomb repulsion has been accounted for by applying weights to the background pairs according to a q_{inv}-dependent description of the Coulomb correlation. The correlation function C_2 which has been corrected in this way was then fitted by a Gaussian parameterization which contained only the pure Bose-Einstein correlation. In this work, a different approach was chosen: the correlation function itself was not corrected for Coulomb repulsion, instead a q_{inv}-dependent term accounting for the Coulomb interaction was introduced

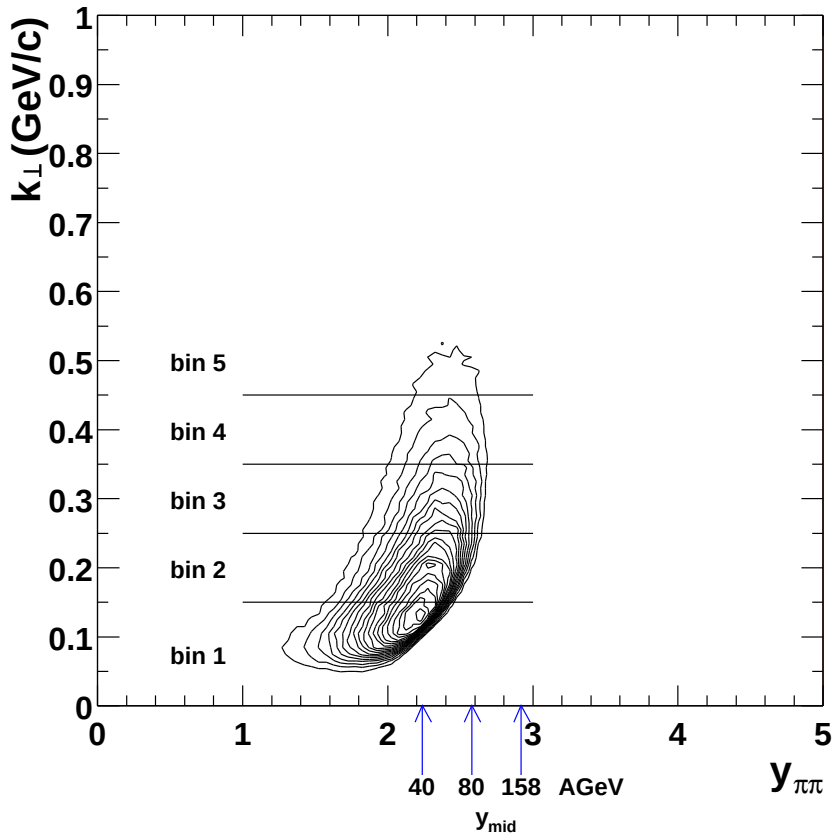

Figure 7.7: Acceptance for $\pi\pi$-pairs. Midrapidity for the three beam energies are indicated by the arrows. The bins in $k_\perp$ are indicated by the horizontal lines.

in the fit function. This strategy allows for a large flexibility to test different assumptions about the underlying Coulomb correlation and to account for non-pionic contaminations of the correlation function, which reduce the correlation signal. Assuming that the purity of the pion sample is reflected in the correlation strength parameter λ the following fit function has been applied to the data:

$$C_2^{\mathrm{cor}}(q_s,q_o,q_l) = N\left[\lambda\cdot\left(\left(1+\exp\left(-q_s^2R_s^2-q_o^2R_o^2-q_l^2R_l^2-2q_oq_lR_{ol}^2\right)\right)\cdot\left(w(k_\perp)(F(q_{\mathrm{inv}})-1)+1\right)-1\right)+1\right]. \tag{7.13}$$

The Coulomb term is coupled with λ to avoid over-correction of the correlation function. An additional $k_\perp$-dependent correction factor $w(k_\perp)$ was derived from Monte-Carlo simulations and accounts for the depletion of the λ parameter due to finite momentum resolution. It ranges from from 1.18 in the first $k_\perp$-bin to 1.81 in the highest $k_\perp$-bin. $F(q_{\mathrm{qinv}})$ is a parameterization which describes the results of quantum mechanical calculations as well as measured correlations of unlike-sign pairs very well (see Eq. (2.60)). As discussed in Section 2.5.3, the inverse of the correction

function obtained for unlike-sign pairs can be used to correct like-sign pairs (see Eq. (2.61)).

Figure 7.8 shows one-dimensional projections of the three-dimensional correlation function. The projection of each component is done over an interval of $|q| < 40$ MeV/c in the other two components. The data points are well described by the modified Gaussian (7.13), shown by the solid line. For comparison, the parameterization (7.13) without considering the Coulomb correlations are shown by the dashed lines. The difference between the two lines reflects the effect of the Coulomb correlations on the whole correlation function C_2 which is due to a combination of Bose-Einstein correlations and Coulomb correlations.

7.3.3 Correction for Momentum Resolution

The finite momentum resolution of the TPC has a significant influence on the HBT radii. The reason for this is that the ideal correlation function $C_2(q_{\text{inv}})$ (*ideal* in terms of infinitely good momentum resolution) has to be folded with the resolution of the detector. The result of this operation is always a distribution which is wider than the original one. The broadening of the distribution in momentum space has a inverse effect in coordinate space — the radii become smaller.

The effect of finite momentum resolution on the obtained HBT radii was studied with a Monte-Carlo simulation. With a simple event generator realistic phase-space distributions of pions were generated and the momenta of the single particles were smeared according to the momentum resolution obtained in section 6.4.2. Also the ϕ and θ angles of the trajectories were smeared, using the angular resolution obtained in 1999 [82]. Then the pions were combined to pairs and the *long*-, *side*-, and *out*-components of the relative momentum were calculated. As a reference, the corresponding components from the unmodified momenta were calculated. For each component the differences between the smeared and the reference momentum-differences were fitted with a Gaussian. The width of the fit function is used as a measure for the momentum-difference resolution. The results are illustrated in Figure 7.9. Shown are the resolutions of the three Cartesian components together with the resolution of q_{inv} as a function of the mean transverse pair momentum $k_\perp$. Obviously, the resolution for q_o is significantly worse than the resolution for the other two components. For small opening angles q_o is given in first order by the difference in the length of the momentum vectors of both particles. Because the absolute momentum resolution is $\Delta p \propto p^2$, the momentum resolution becomes worse for increasing $k_\perp$, strongly influencing the resolution of q_o. On the other hand, q_s is mostly determined by the opening angle of the particle pair. Therefore, the influence of the single track momentum resolution on the resolution of q_s is strongly reduced. For q_l the better resolution can be explained by the boost into the LCMS[2]. In this reference frame the longitudinal momentum of the particle pair is zero and q_l is given by the difference in the longitudinal momentum components of the single particles. Assuming $\gamma\beta \approx 5$, this component, and thus its resolution, is much reduced by boosting from the lab reference frame into the LCMS.

The influence of the finite momentum resolution on the reconstructed HBT radii was studied by extracting the HBT radii from simulated two-particle correlation functions. These correlation functions have been constructed by filling the generated pion pairs according to their smeared momentum components q_l, q_s, and q_o into a three-dimensional histogram. Each entry was weighted with a factor given by Eq. (7.12), evaluated with the true momentum components. The resulting

[2] **L**ongitudinally **C**o **M**oving **S**ystem

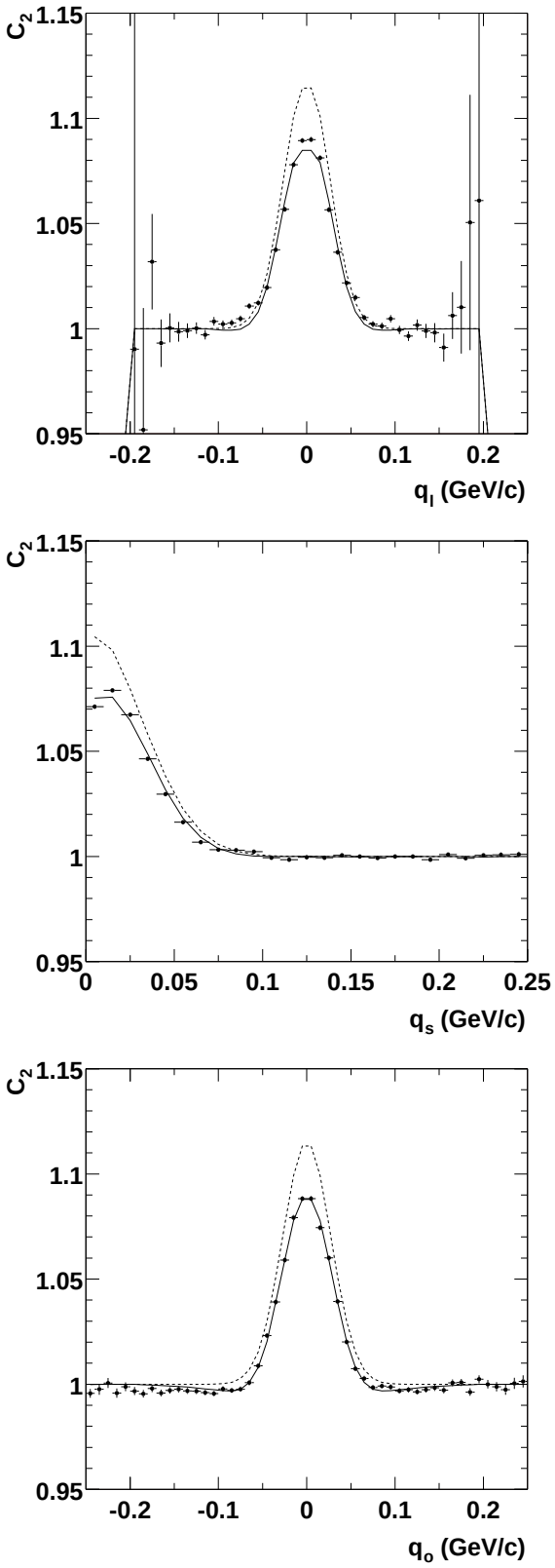

Figure 7.8: One-dimensional projections of the three-dimensional correlation function C_2 in the Bertsch-Pratt parameterization. The solid lines show the fit of (7.13) to the data points. For comparison also the parameterization (7.13) without Coulomb correlations are shown by the dashed lines.
The projections are done over an interval of $|q| < 40\,\mathrm{MeV}/c$ in the other components.

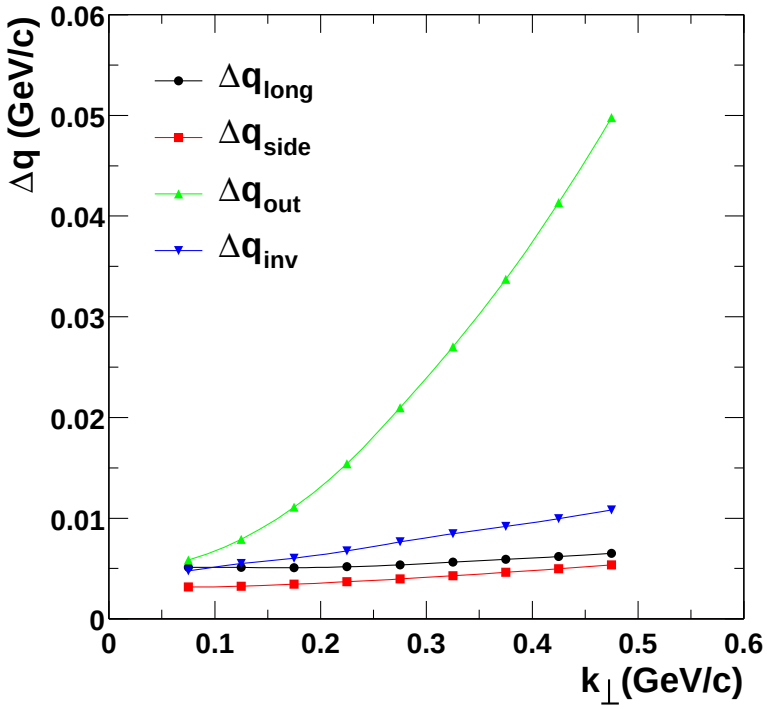

Figure 7.9: Resolution of the *long*-, *side*-, *out*-components of the momentum difference as a function of the mean transverse pair momentum $k_\perp$.

correlation function was fitted with Eq. (7.12), leading to the simulated *measured* radii R_{meas}. This procedure was repeated assuming different input source radii. The simulated *measured* radii as a function of the true radii are shown in Figure 7.10 for different $k_\perp$-bins. The dependency R_{meas} vs. R_{real} was parameterized with a polynomial of second order and used to correct all radii shown in Chapter 8. For R_l and R_s the correction factors are close to unity but R_o is much more affected which is a consequence of the poorer momentum-difference resolution in this component.

As an example, Figure 7.11 shows the effect of the correction for $E_{\mathrm{beam}} = 158$ AGeV. As already discussed in connection with the correction factors, the influence is nearly invisible for R_l and R_s and becomes large for R_o at large $k_\perp$.

7.4 Correlation Function with Positive and Negative Particles

The correlation functions have been studied separately for pairs of positive and negative particles. As shown in Figure 7.12 no significant differences between the two different data sets have been observed. In order to increase the statistical significance of the extracted HBT radii, the signal and background distributions of both charges have been added before fitting the three-dimensional correlation function.

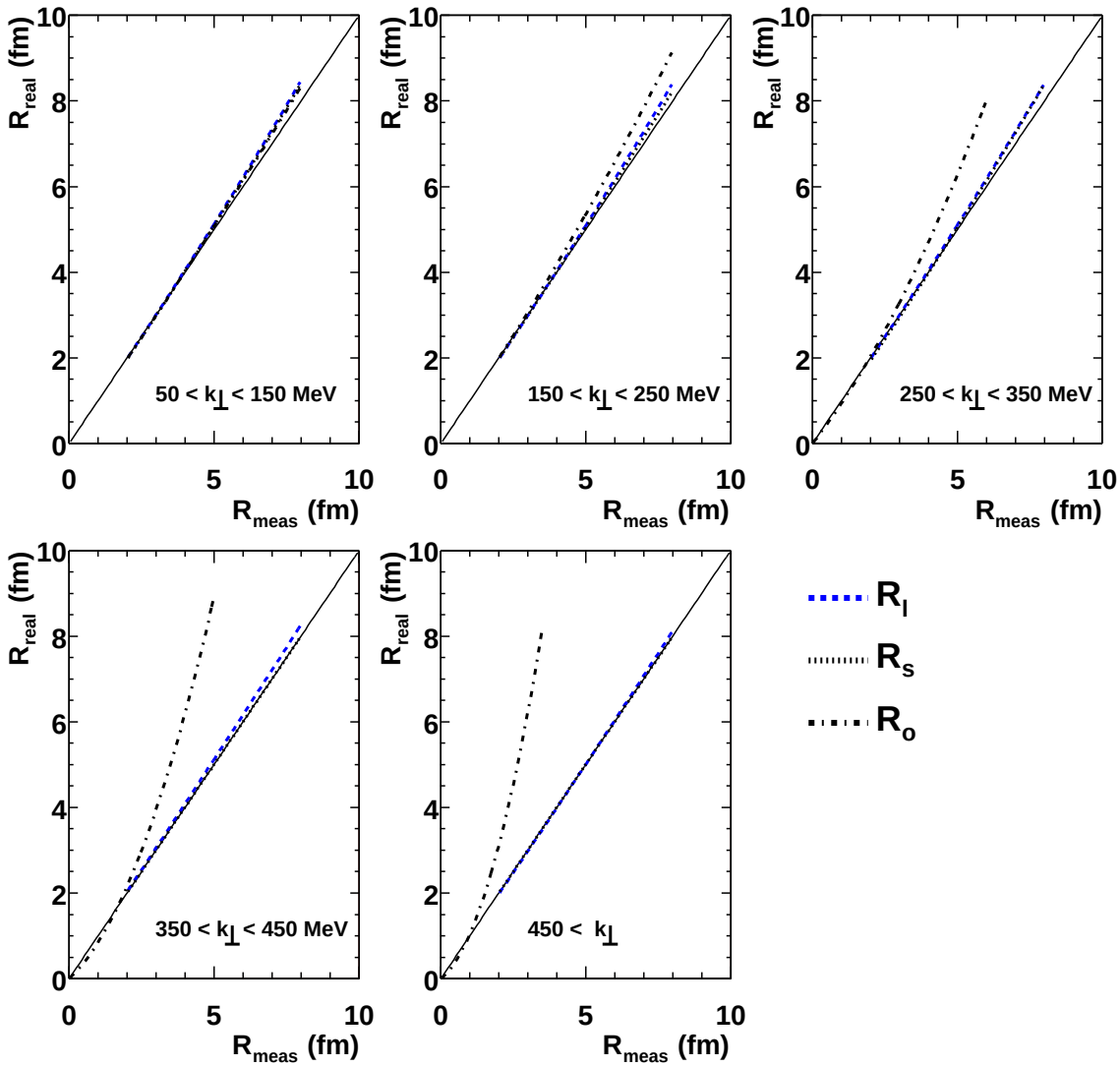

Figure 7.10: Deviation of the reconstructed radii R_{meas} from the real radii R_{real} due to the finite momentum resolution of the TPC.

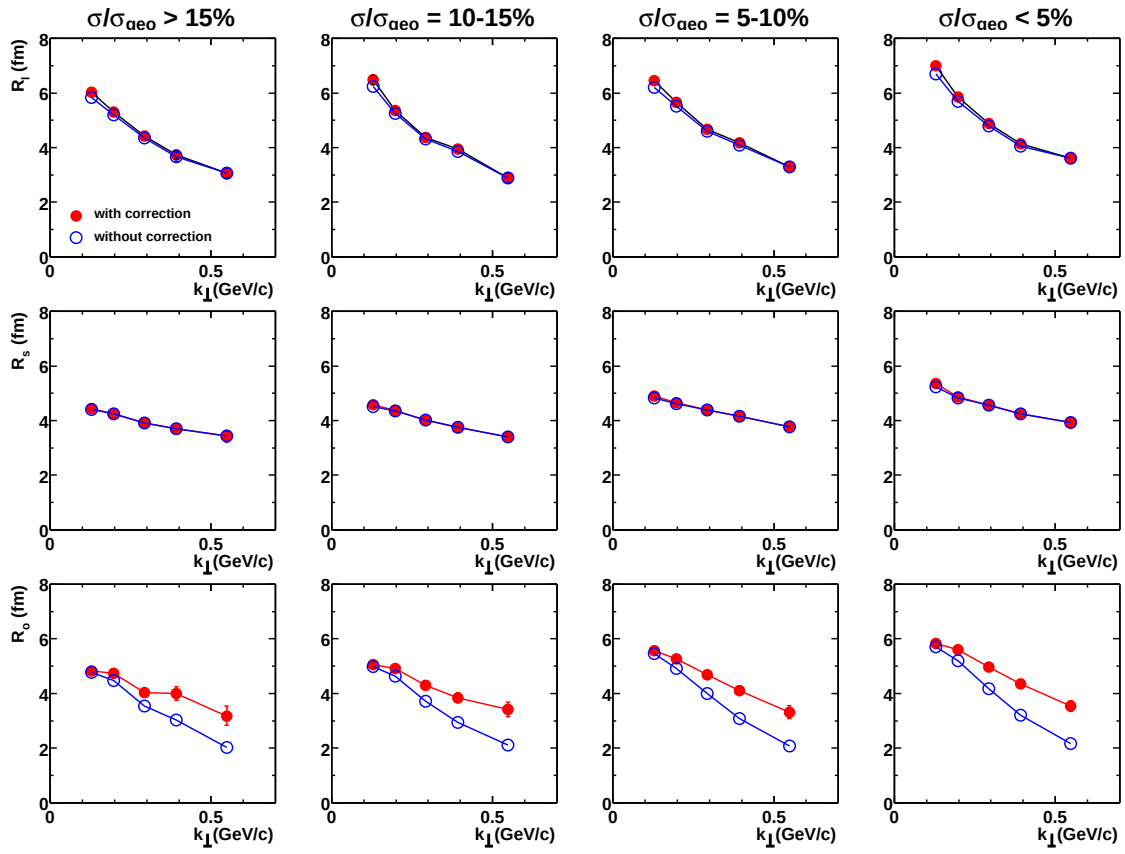

Figure 7.11: Comparison of uncorrected and corrected HBT radii for $E_{\text{beam}} = 158$ *A*GeV.

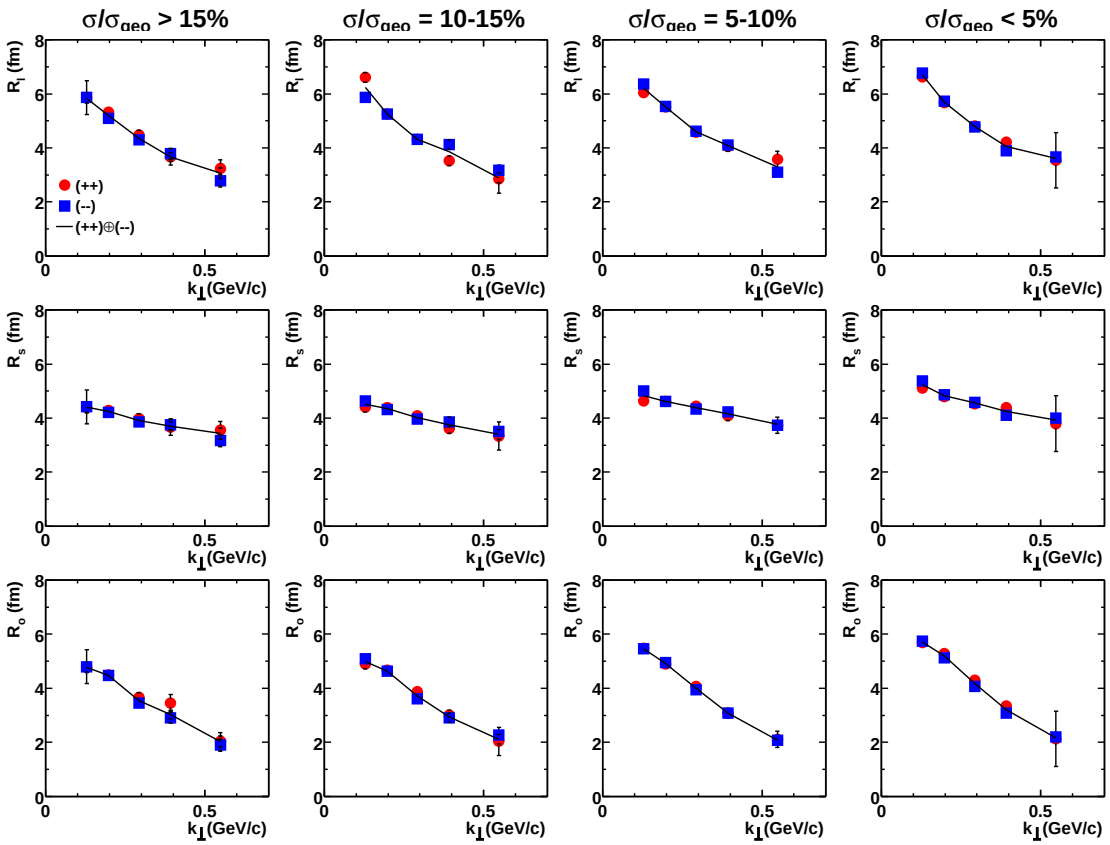

Figure 7.12: R_l, R_s, and R_o for $(++)$ and $(--)$ particle pairs for $E_{\text{beam}} = 158\,A\text{GeV}$. Also shown are the results for a combined analysis of both charges. All radii are not corrected for momentum resolution.

8 HBT Results

In this chapter the results of a differential analysis of Bose-Einstein correlations at beam energies of 40, 80, and 158 *A*GeV are presented. The extracted HBT radius values, depending on the mean transverse pair momentum $k_\perp$, are used to gain information about the spatial expansion of the pion emitting source as well as its temporal evolution, e. g. the lifetime of the system and the duration of particle emission. Furthermore, the comparison of the different beam energies allows to deduce the conditions for thermal freeze-out.

8.1 HBT Radii as Lengths of Homogeneity

A qualitative study of the physical origin of the pair-momentum dependence of the HBT parameters of the Bertsch-Pratt parameterization for an infinitely long source with boost-invariant longitudinal expansion was done by Makhlin and Sinyukov [38]. They used the model-independent expressions in terms of space-time variances for the HBT parameter and evaluated them approximately analytically. They could show that the longitudinal HBT radius R_l is finite and determined by the inverse of the longitudinal velocity gradient, noting for the first time that R_l has the property of a *longitudinal length of homogeneity* in the source rather than being related to the longitudinal geometric size of the entire source. The analytical determination of the space-time variances is based on the method of saddle-point integration of the emission function $S(\mathbf{x},\mathbf{K})$. It turned out [83, 84] that not all of the important qualitative features of the $k_\perp$ dependence of the HBT parameters can be obtained from the leading term in the saddle-point approximation and for a quantitative comparison with data a full numerical evaluation of the integrals for the variances must be done.

For a longitudinally finite ($L = \tau_f \Delta\eta$) source of the type as described by (2.22) in the limit $\Delta\tau = 0$ the transverse and longitudinal *dynamical lengths of homogeneity* are given in the LCMS by [83]:

$$\text{transversal:} \qquad R_H(m_\perp) = \frac{R}{\eta_f}\sqrt{\frac{T}{m_\perp}} = \frac{1}{\partial\eta_t(r)/\partial r}\sqrt{\frac{T}{m_\perp}}, \tag{8.1}$$

$$\text{longitudinal:} \qquad L_H(m_\perp) = \tau_f\sqrt{\frac{T}{m_\perp}} = \frac{1}{\partial\cdot u_l}\sqrt{\frac{T}{m_\perp}}, \tag{8.2}$$

with R being the transverse geometrical source radius, $u_l = (\cosh\eta_l, 0, 0, \sinh\eta_l)$ the longitudinal flow 4-velocity, η_f the transverse flow rapidity, and τ_f the duration of the expansion.

The HBT radii are not only determined by the Gaussian widths in Eq. (2.22). In addition, the radii are dynamically affected through the *dynamical lengths of homogeneity* R_H and L_H. These lengths are inversely proportional to the gradients of the expansion velocity field in the respective direction, but smeared by a thermal factor $\sqrt{T/m_\perp}$ which is a result of the thermal motion of

the particles around the collective flow velocity. Bose-Einstein correlations occur only between particles which are close in phase-space. Collective expansion tends to reduce the size of the regions within which particles can develop such correlations. Thermal motion as described by the thermal velocity about $\sqrt{T/m_\perp}$ smears out the flow velocity gradients and thus acts in the opposite direction [39, 38]. This leads to a characteristic dependence of the homogeneity length on the transverse mass $m_\perp$ of the correlated pairs. The HBT radii are determined by the smaller of the two (geometric or dynamic) lengths scales. In the limit $T \to 0$ any velocity gradient in the system leads to a vanishing dynamical length of homogeneity and therefore to vanishing HBT radii. At finite T, the dynamical smearing decreases with increasing transverse mass $m_\perp$, leading to a decrease of the HBT radii at large $m_\perp$, i. e. large $k_\perp$.

A differential HBT analysis as a function of the mean transverse pair momentum $k_\perp$ thus reveals information about the dynamical behavior of the source. For the scenario of a boost-invariant expansion in longitudinal direction of the particle emitting source the dependence of R_l on $k_\perp$ was given as [38]:

$$R_l = \frac{\tau_f}{\cosh(y_{\pi\pi} - y_{\text{obs}})} \sqrt{\frac{T}{m_\perp}}, \tag{8.3}$$

with $m_\perp = \sqrt{m_\pi^2 + k_\perp^2}$ being the transverse mass of the pion pair. T is the freeze-out temperature of the system and τ_f the freeze-out time. In the LCMS reference frame the pair rapidity $y_{\pi\pi}$ is equal to the rapidity y_{obs} of the observer frame and (8.3) simplifies for boost-invariant expansion of the sources to Eq. (2.26).

The dependency of R_s on $k_\perp$ is strongly determined by transverse flow and is independent of $k_\perp$ without transverse flow. The transverse size of the particle source is controlled by the transverse flow velocity $\langle v_\perp \rangle$ and approximately given by [35, 36, 85]:

$$R_s^2 \approx \frac{R_{\text{geo}}^2}{1 + \frac{\eta_f^2}{T_f} m_\perp}. \tag{8.4}$$

η_f is a model-dependent factor (see page 103) which describes the transverse flow (see below) and R_{geo} characterizes the geometric transverse size of the fireball at freeze-out.

In addition to the freeze-out time τ_f the duration of particle emission $\Delta\tau$ is of interest. Theoretical studies predict a long duration of emission for the case of a phase transition or the existence of a mixed hadronic–QGP phase. The reason for this is the big entropy difference of both phases, leading to a large latent heat. A long emission time could be observable in a significant difference between R_o and R_s because the space-time correlation of the emission process leads to an increasing effective source size in R_o [86, 87, 41]. An expression for the emission duration, also valid for systems with no boost invariance, was given by [44]

$$\Delta\tau^2 = \frac{1}{\beta_\perp^2 \gamma_{\text{YKP}}^2} (R_o^2 - R_s^2) - \beta_{\text{YKP}} R_\parallel^2, \tag{8.5}$$

with $\gamma_{\text{YKP}}^2 = (1 - \beta_{\text{YKP}}^2)^{-1}$. If the radii R_l and R_s were measured in the rest frame of the source element ($\beta_{\text{YKP}} = 0$) Eq. (8.5) simplifies to

$$\Delta\tau^2 = \frac{1}{\beta_\perp^2} (R_o^2 - R_s^2). \tag{8.6}$$

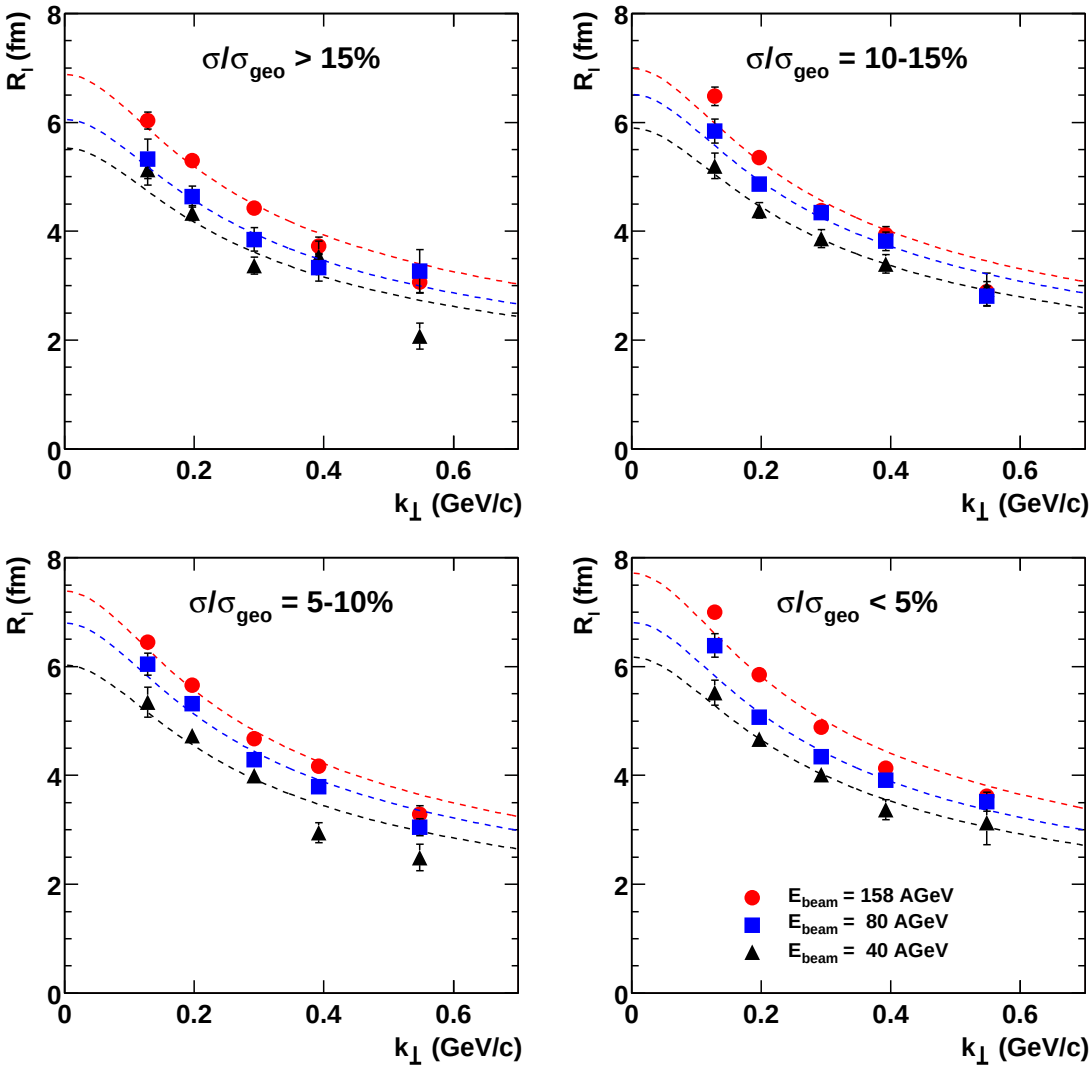

Figure 8.1: R_l for different values of E_{beam} and different centralities as a function of the mean transverse pair momentum $k_\perp$.

A detailed discussion of the HBT radius parameter as a function of $k_\perp$, beam energy, and centrality is given in the following subsections.

8.1.1 The Longitudinal Radius Parameter R_l

Figure 8.1 shows the HBT radius R_l as a function of $k_\perp$ for all three analyzed beam energies in four different bins of centrality. The radii decrease with increasing transverse momentum from about 5.5-6.5 fm to 3-4 fm and increase with beam energy and slightly with multiplicity. The dashed lines are the results of fitting function (8.3) to the data points, assuming a temperature $T = 120$ MeV. The chosen temperature is consistent with results of previous analyses, e. g. [50].

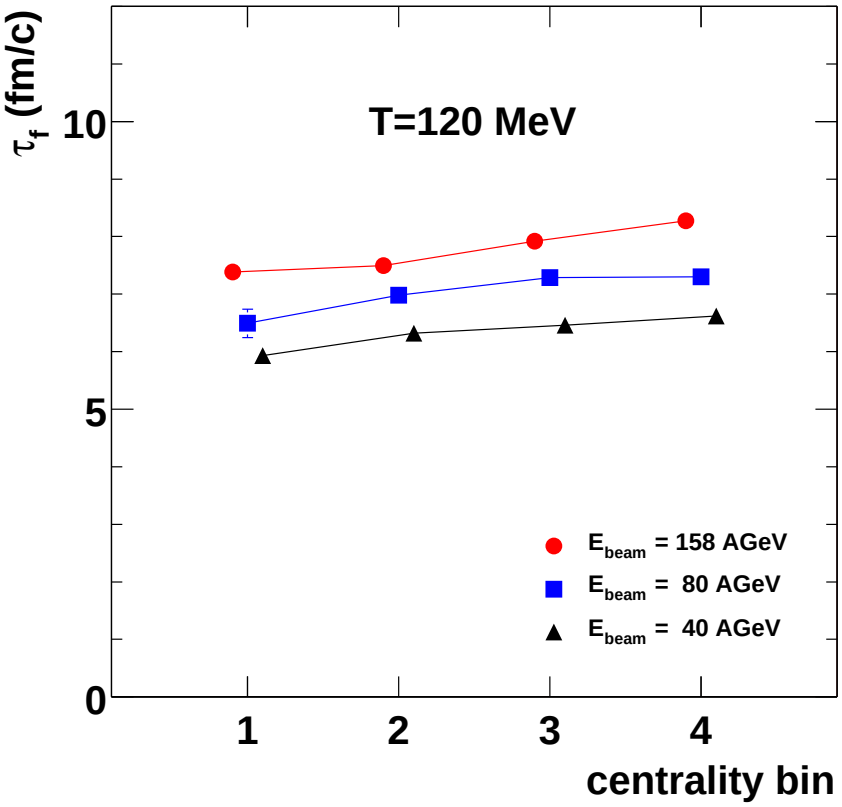

Figure 8.2: Freeze-out time τ_f as a function of centrality of the collision.

The fits describe the data very well, consistent with the presence of longitudinal boost-invariant expansion (at least over some rapidity and z-interval) and allowing the extraction of the freeze-out time according to Eq. (8.3). The lifetime obtained by fitting this function to the data is shown in Figure 8.2. The longitudinal radius parameters R_l, and with it τ_f, increase with centrality and E_{beam}. This result is not very surprising and can be explained by simple considerations of the collision dynamics. The energy deposited in the collision region increases with increasing energy of the colliding nuclei and the centrality of the collision. Therefore, the expanding system needs more time until it reaches the critical condition for the freeze-out.

8.1.2 The Transverse Radius Parameter R_s

The results for R_s are shown in Figure 8.3, again for all beam energies as a function of $k_\perp$. The absolute values as well as the slopes of R_s for beam energies of 80 and 158 AGeV are very similar, increasing only slightly with centrality. This increase is given by the geometry of the collision. As the collisions become more central, the overlap between the two nuclei increases, leading to a larger reaction volume. The radii for $E_{\text{beam}} = 40$ AGeV do not follow the systematics of the two other energies. The $k_\perp$ dependence is much steeper and R_s is larger at small values of $k_\perp$. The

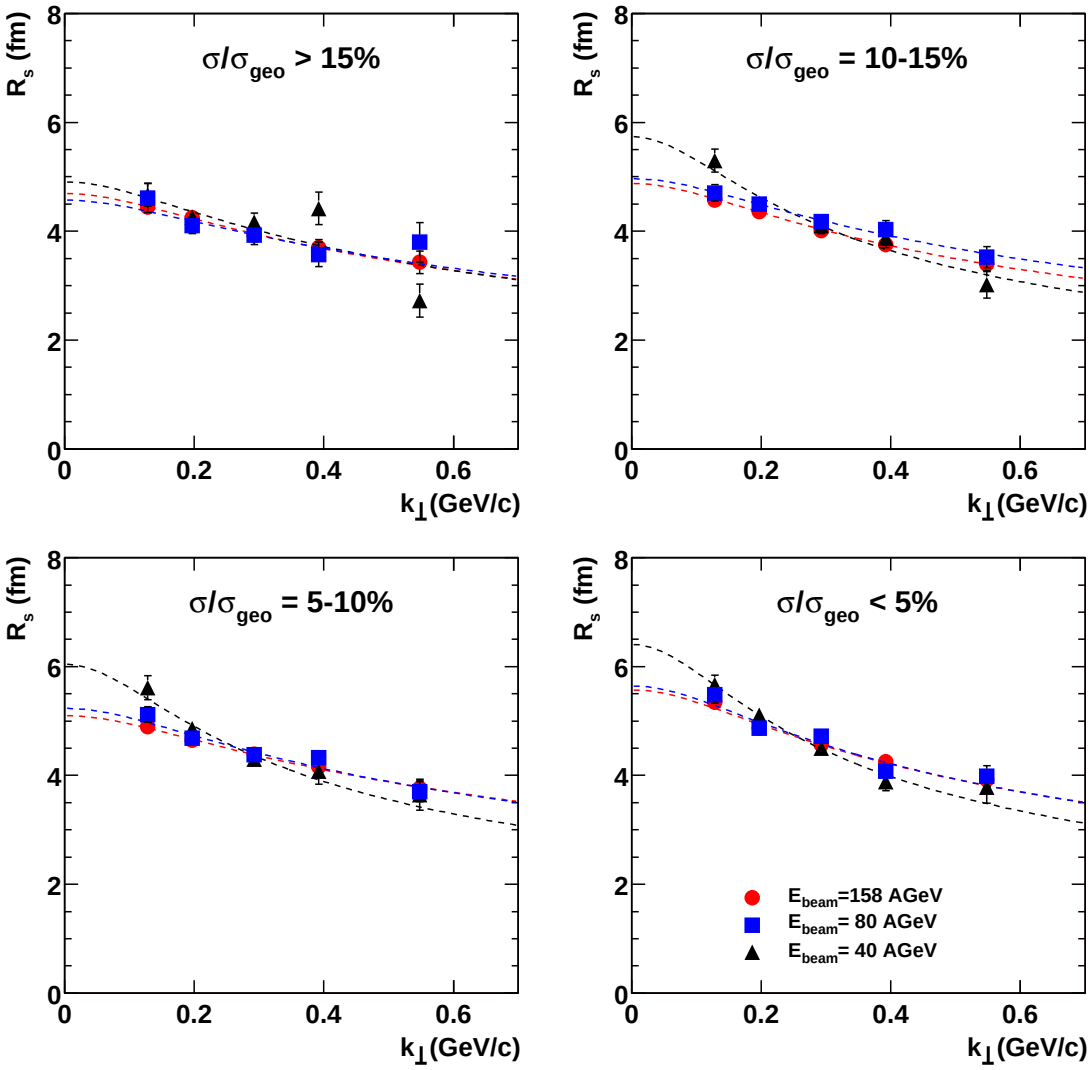

Figure 8.3: R_s as a function of $k_\perp$ for the three beam energies and the different multiplicity bins.

dashed lines show the fit of Eq. (8.4) to the data, providing an estimate for the geometric transverse source radius R_{geo} and the transverse flow rapidity η_f (see Section 8.1.5).

8.1.3 The Radius Parameter R_o

The duration of particle emission is given by the difference between R_o and R_s according to Eq. (8.6):

$$\Delta\tau^2 = \frac{1}{\beta_\perp^2}(R_o^2 - R_s^2),$$

where $\beta_\perp$ is the mean transverse velocity of the particle pair given by $\beta_\perp = k_\perp/\sqrt{m_\pi^2 + k_\perp^2}$. Figure 8.4 shows R_o (data points represented by symbols) together with R_s (solid lines). While for

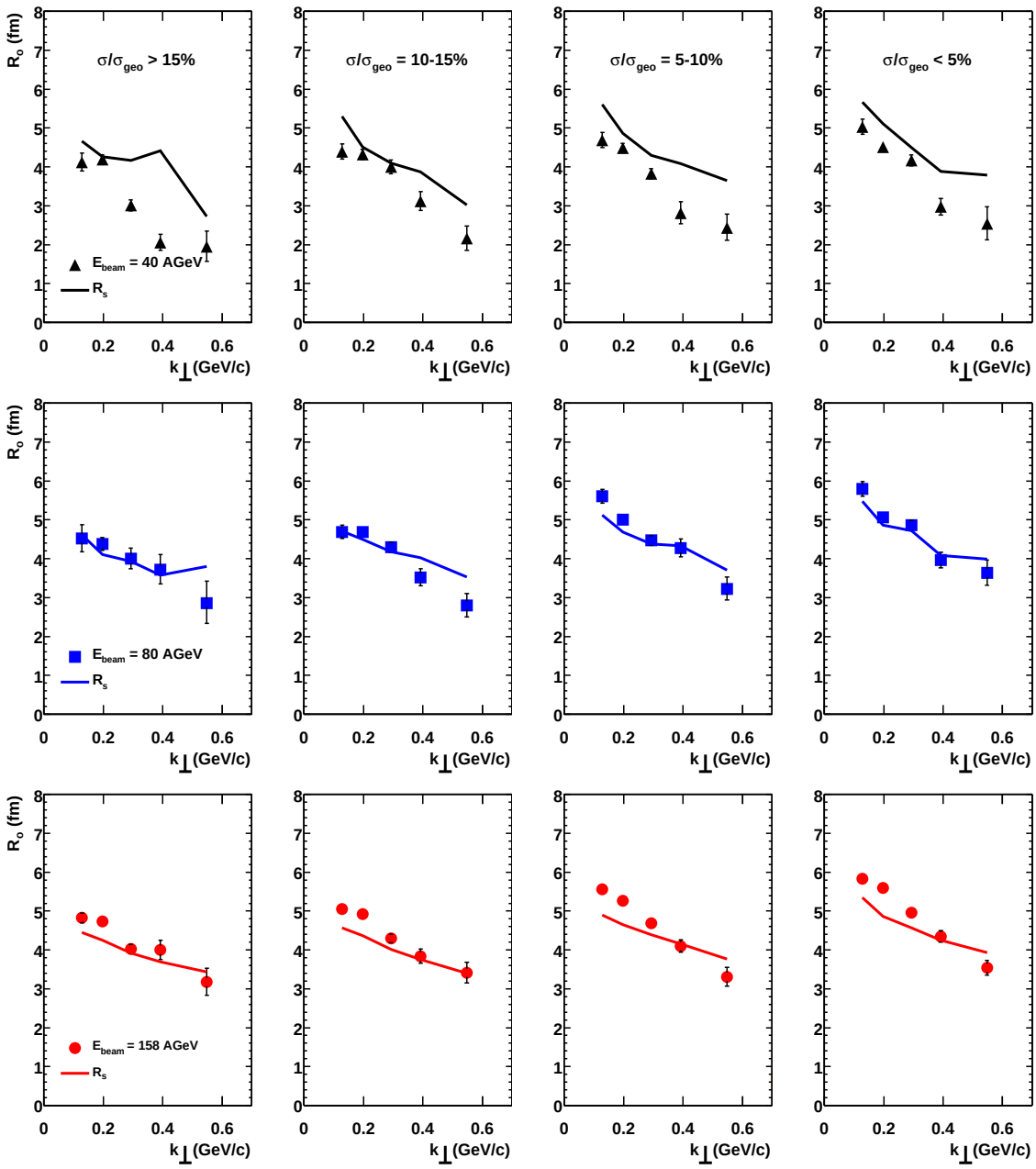

Figure 8.4: R_o for 40, 80, and 158 *A*GeV beam energy (from top to lower panel). The radii are shown vs. $k_\perp$ for different centralities. The lines show the results of R_s for comparison.

the beam energies of 40 and 80 *A*GeV R_o is smaller or comparable to R_s, it is larger than R_s for $E_{\text{beam}} = 158$ *A*GeV, at least in the first $k_\perp$ bins. This indicates a small but finite duration of particle emission. However, the larger systematic errors on R_o, especially for large $k_\perp$, do not allow to exclude an emission duration compatible with zero.

The calculated duration of the emission process $\Delta\tau$ at 158 *A*GeV is shown in Figure 8.5. $\Delta\tau$

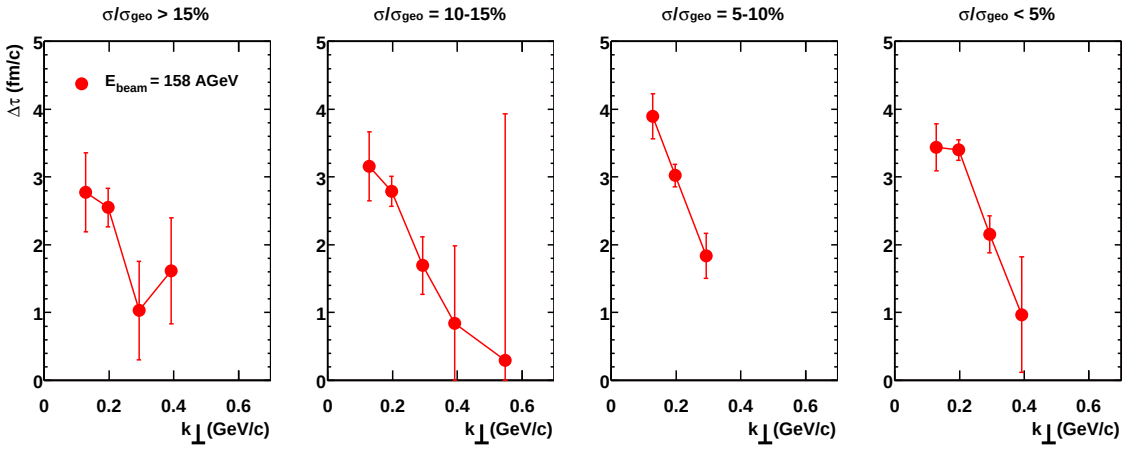

Figure 8.5: Duration of particle emission $\Delta\tau$ for beam energy of 158 *A*GeV.

is of the order 2–4 fm/c. In addition to the duration of the emission of the source, $\Delta\tau$ contains a contribution which has nothing to do with the duration of the emission but is a relativistic effect and should be observable even for $\Delta\tau = 0$. Since the two-particle correlation function is sensitive to particle pairs emitted from a longitudinal region of homogeneity of size $R_l = l^*$, it probes emission from different points z at different times $t = \sqrt{\tau_f^2 + z^2}$ along the proper-time hyperbola $\tau = \tau_f$. The maximal range of this region is $-l^* \lesssim z \lesssim l^*$. Thus, even for instantaneous freeze-out at constant proper time the correlator sees a non-vanishing emission duration in the fixed observer frame. Since l^* is a decreasing function of $k_\perp$, $\Delta\tau$ approaches the limit of the real emission duration for large $k_\perp$.

8.1.4 The Cross-Term R_{ol}^2

The existence of the cross-term R_{ol}^2 was proposed for the first time by Chapman, Scotto, and Heinz [88] and experimentally verified by Alber [89]. This parameter is the result of space-time correlations which occur if the observer frame does not coincide with the rest frame of the source element. The cross-term vanishes in the LCMS for longitudinally boost-invariant systems or in symmetric collisions as midrapidity. This follows from the corresponding space-time variance (2.42) which vanishes in the LCMS if the source is symmetric under $\tilde{z} \to -\tilde{z}$. However, in the forward and backward rapidity region this reflection symmetry is broken for systems with finite longitudinal extension.

Figure 8.6 shows the $k_\perp$ dependence of R_{ol}^2 for the different multiplicity bins and the three analyzed beam energies. For all energies and multiplicities, R_{ol}^2 is very small.

For high $k_\perp$ values the cross-term converges to zero because in that case the longitudinal radius parameter R_l decrease to zero for the case of a strongly expanding source. With vanishing R_l also the correlations between q_l and q_o vanish as well. The observed weak dependence on E_{beam} can be understood in terms of the slight shift of the rapidity acceptance away from midrapidity with increasing beam energy. For $E_{\text{beam}} = 40$ *A*GeV the experimentally accessible rapidity interval is closest to midrapidity and therefore R_{ol}^2 is smallest for this beam energy.

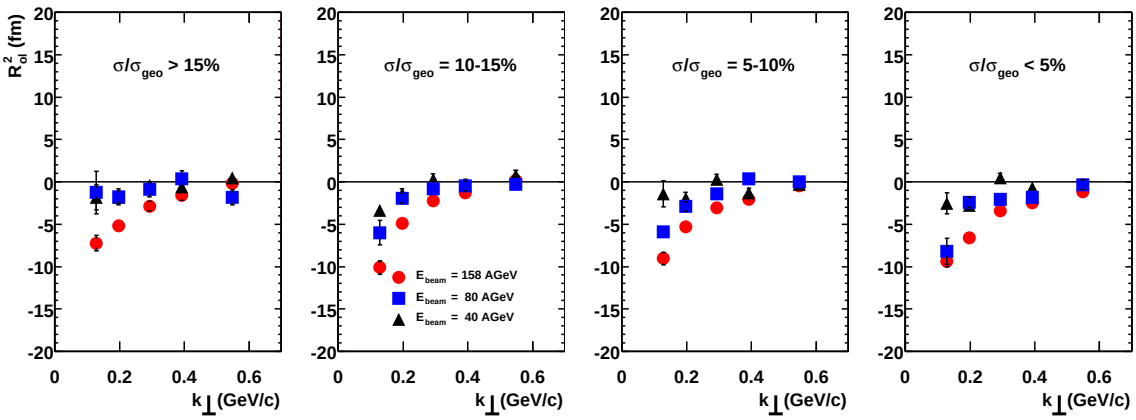

Figure 8.6: The cross-term R^2_{ol}.

8.1.5 Transverse Flow

One of the main motivations for HBT analysis is its capability to disentangle random and collective dynamical components in the expansion of the fireball. The random components are an effect of the temperature of the system while the collective components are due to hydrodynamic pressure which results from intense rescattering among the constituents of the fireball. Knowledge of the magnitude of the transverse flow is crucial for a dynamical picture of the transverse expansion of the collision system and for a dynamical back-extrapolation into the hot and dense early stage of the collision.

The normalization of measured hadron spectra (the yields and abundance ratios) provide information about the chemical composition of the fireball at the *chemical* freeze-out. In addition, the hadronic momentum spectra provide information about thermalization of the momentum distributions and collective flow. If rescattering among the fireball constituents results in thermalization and collective flow, the shapes of hadronic $m_\perp$ spectra are characterized by the temperature T_f and the mean transverse flow velocity $\langle v_\perp \rangle$ at freeze-out. The single-particle spectra are determined by an effective blue-shifted temperature from which temperature and flow effects cannot be separated unambiguously [90]. In contrast, the $m_\perp$ dependence of the transverse HBT-radii increase with transverse flow but decrease with stronger thermal smearing [39]. The combination of both observables allows to remove the ambiguity between temperature and flow.

The interpretation of flow in the longitudinal direction is difficult due to partial transparency of the colliding nuclei. The observed longitudinal flow is only partly generated by hydrodynamic pressure and superimposed to an initial longitudinal expansion as the result of incomplete stopping of the two nuclei. In contrast, transverse flow is created only after impact and is reflected in the spectra of transverse mass $m_\perp = \sqrt{m^2 + p_\perp^2}$.

In the relativistic limit ($m_\perp \gg m_0$) the rest mass can be neglected. The effect of flow on the spectra is given by the simple blue-shift formula [91]

$$T_{\text{slope}} = T \sqrt{\frac{1+\langle v_\perp \rangle}{1-\langle v_\perp \rangle}}. \tag{8.7}$$

At large $m_\perp$ all hadron spectra should have the same inverse slope $T_{\rm slope}$ but the measurement of the inverse slopes does not allow for a separation of thermal from collective motion. On the other hand, flow couples to the rest mass in the nonrelativistic region. For a linear transverse flow velocity profile and a Gaussian transverse density profile one finds exactly [36, 92, 85]:

$$T_{\rm slope} = T_f + \frac{1}{2} m_0 \langle v_\perp \rangle^2. \tag{8.8}$$

Such an approximately linear rest mass dependence is indeed observed [93]. For protons for example an inverse slope of about 300 MeV was seen which can obviously not be interpreted as a hadronic temperature but shows clearly that the spectra contain a collective flow component. A very accurate determination of $\langle v_\perp \rangle$ from the measured mass dependence of the inverse slope alone is not possible. Studying the effect of transverse flow on two-particle correlations can help to separate the effects of random thermal and collective motion.

Equation (8.4) alone does not allow to separate T_f from $\langle v_\perp \rangle$ either. But the correlation between the two parameters in (8.4) is exactly opposite to that provided by the spectral slopes in (8.8). Combining them in a simultaneous analysis of spectra and correlations allows for a rather accurate separation of directed collective and random thermal motion.

A combined analysis was done in [50, 78, 94], based on a full model parameter scan with χ^2 confidence levels for the two-particle spectra. The model analysis assumed an emission function of type (2.22). Within this model the transverse geometry is specified by a distribution $G(r)$ which was assumed to be Gaussian

$$G(r) = \exp\left(-\frac{r^2}{2R_G^2}\right) \tag{8.9}$$

or box-shaped

$$G(r) = \theta(R_B - r). \tag{8.10}$$

The transverse expansion is parameterized by the transverse flow rapidity $\eta_t(x)$ which is assumed to increase linearly with the distance from the collision axis:

$$\eta_t(x) = \eta_f \frac{r}{r_{\rm rms}}. \tag{8.11}$$

The scaling factor η_f specifies the value of the transverse flow rapidity at the transverse rms radius, given by

$$r_{\rm rms} = \sqrt{2} R_G \tag{8.12}$$

for the Gaussian transverse distribution and by

$$r_{\rm rms} = \frac{R_B}{\sqrt{2}} \tag{8.13}$$

for the box-shaped one. With the transverse profiles $G(r)$ the average transverse expansion velocity $\langle v_\perp \rangle$ is given by

$$\langle v_\perp \rangle = \frac{\int_0^\infty r\,{\rm d}r\, \tanh \eta_t(r) G(r)}{\int_0^\infty r\,{\rm d}r\, G(r)}. \tag{8.14}$$

In this thesis no analysis of single-particle spectra was done. Rather the determination of the transverse flow velocity was based on the results of the HBT analysis only. Fitting Eq. (8.4) to R_s

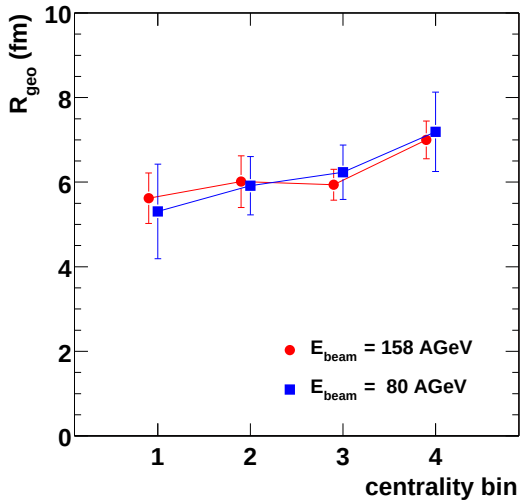

Figure 8.7: Transverse mean geometric source radius R_{geo} as a function of the centrality bin.

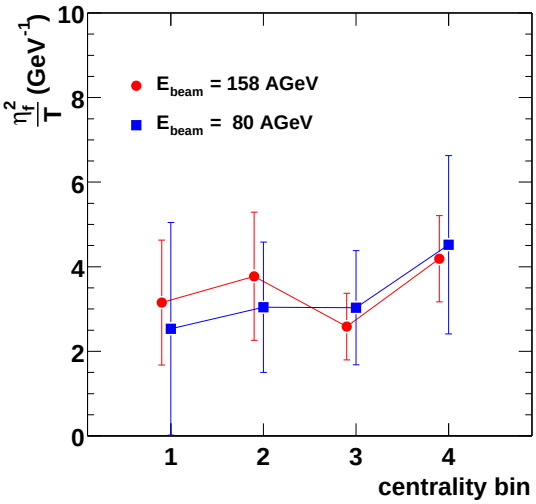

Figure 8.8: The fit parameter η_f^2/T_f for the different centrality bins.

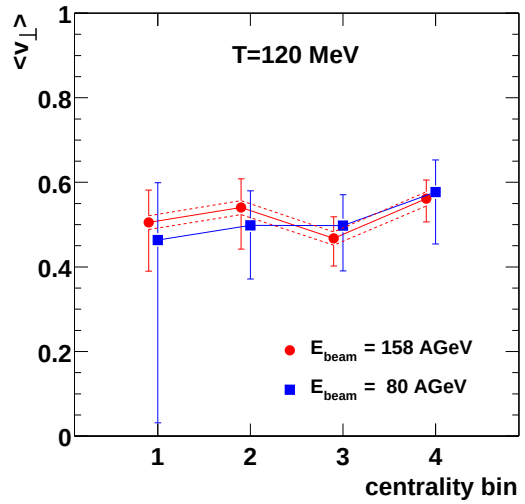

Figure 8.9: The mean transverse expansion velocity $\langle v_\perp \rangle$.

provides the geometrical radius R_{geo} and the ratio η_f^2/T. Employing the model described above, the transverse expansion velocity is extracted assuming a temperature $T = 120$ MeV and a box-shaped transverse profile (in [94] it is shown that the box-shaped density profile reproduces the data with better χ^2).

The fit parameters R_{geo} and η_f^2/T for the beam energies 80 and 158 *A*GeV are shown in Figures 8.7 and 8.8. The results of $\langle v_\perp \rangle$ are shown in Figure 8.9. The dashed lines in Fig. 8.9 show the influence of the temperature on the transverse expansion velocity. They are determined

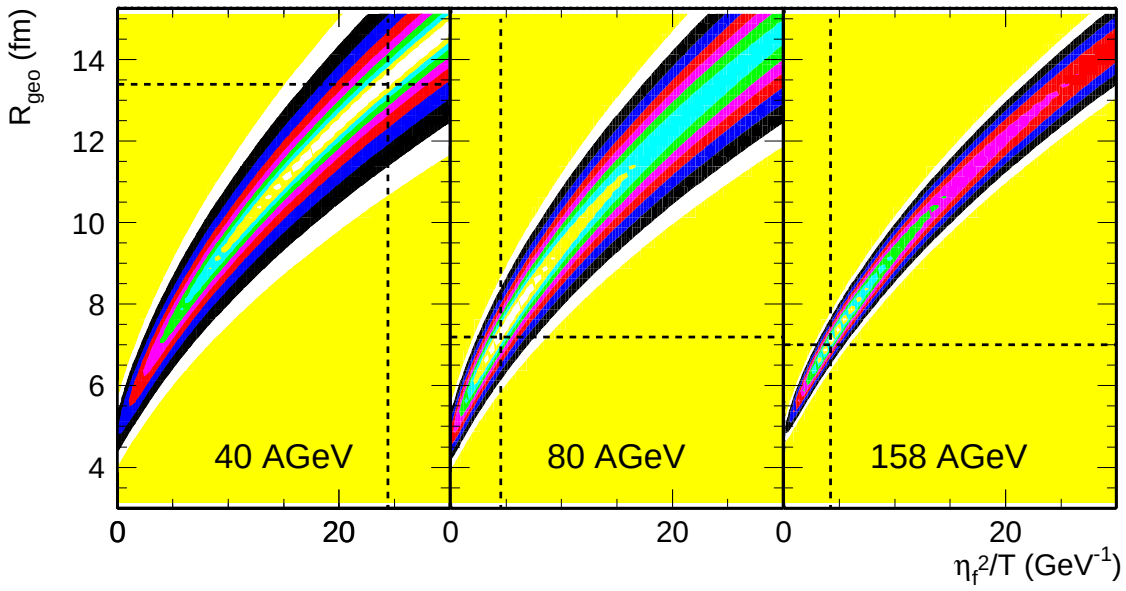

Figure 8.10: Contour plot of χ^2, obtained by fitting (8.4) to R_s.

by assuming a temperature of 110 MeV and 130 MeV, respectively. A temperature variation of ± 10 MeV leads to a change of the expansion velocity in the order of $\pm 5\%$.

While the fit of Eq. (8.4) delivers reasonable results for these energies (geometric radii between 5 and 6 fm with expansion velocities between $0.3c$ and $0.5c$) it fails for $E_{\text{beam}} = 40$ AGeV. The geometric radius reaches values of 12 fm and above while the expansion velocities are close to $0.8c$. Both parameters with very large error bars. The reason for the failure of fitting R_s at 40 AGeV is shown in Fig. 8.10. The Figure shows contour plots of χ^2 as a function of the fit parameters R_{geo} and η_f^2/T for all three beam energies at the most central multiplicity. The results of the fits, the parameter combinations with minimal χ^2, are indicated by the dashed lines. While for $E_{\text{beam}} = 158$ AGeV the minimum is clearly pronounced it becomes more elongated for $E_{\text{beam}} = 80$ AGeV. For 40 AGeV no minimum is visible and the χ^2 distribution stays flat even for large values of R_{geo} and η_f^2/T, leading to the large values and error bars for this parameter. This clearly indicates strong problems of the approximation (8.4).

8.2 Beam Energy Dependence

Figure 8.11 [97] shows the $k_\perp$ dependencies of R_l, R_s, and R_o for different beam energies. The data at AGS and RHIC energies are from [95, 96]. At first glance, all three radii show a rather weak and smooth energy dependence. However, a more detailed inspection displays some interesting features.

R_l is approximately constant from AGS to the lower SPS energies. Starting with the SPS energies towards RHIC, R_l increases significantly, indicating a smooth increase of the lifetime of the system. In contrast, R_s is decreasing at small $k_\perp$ up to top SPS energies, connected with a

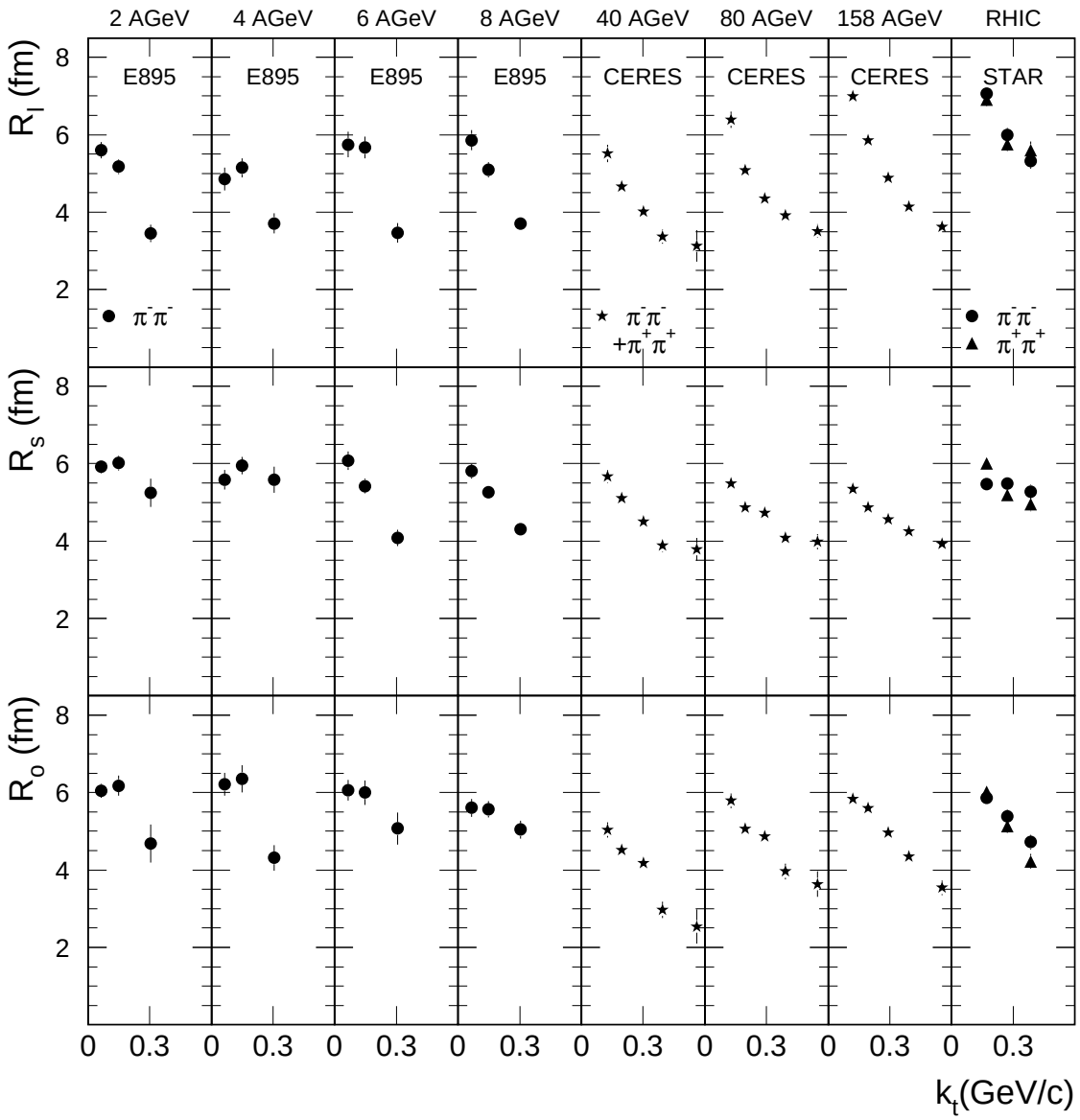

Figure 8.11: $k_\perp$ dependence of HBT radii in central Pb-Pb, Au-Au, and Pb-Au (CERES) collisions at different beam energies. RHIC and AGS data are taken from [95, 96].

continuous flattening of the $k_\perp$ dependence. Going to RHIC energies, R_s becomes again larger than at SPS energies with a somehow flat $k_\perp$ dependence (at least for the $\pi^-\pi^-$ sample). According to Eq. (8.4) the flattening indicates a decrease of the radial flow velocity as a function of the beam energy. This would be in contradiction to the present understanding [98], where a continuously increasing flow velocity was deduced from the analysis of single-particle spectra.

R_o shows a rather structureless beam energy dependence, possibly indicating a shallow minimum at the lower SPS energy.

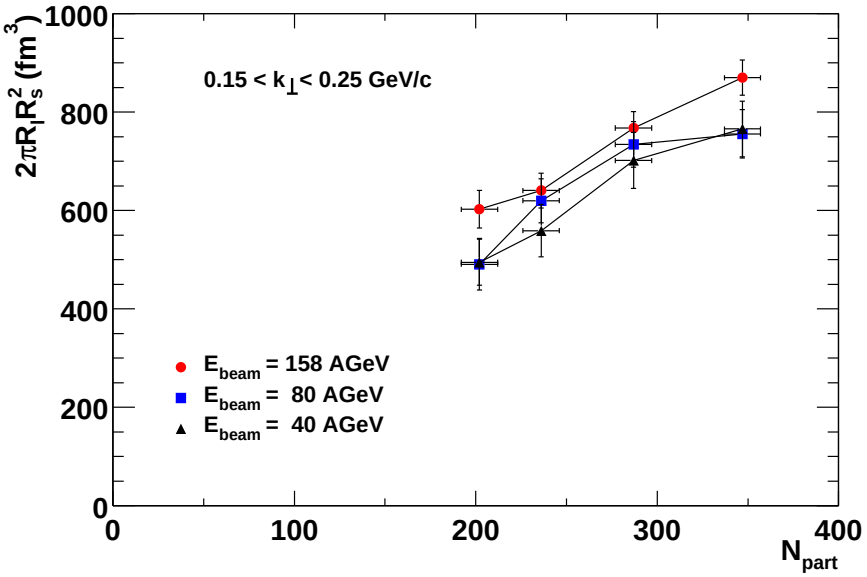

Figure 8.12: The effective volume V_{eff} as a function of N_{part} for different beam energies.

8.3 The Freeze-out Volume

The HBT analysis probes the state of the system at thermal freeze-out, i. e. the time when the last elastic interaction between the constituents of the expanding fireball occurs. According to Pomeranchuk [99], this point in time should be characterized by a certain critical particle density. While the energy or particle yields can be measured using the single-particle spectra of all emitted particles, HBT analysis provides the tools to determine a volume-like quantity.

A detailed study of the freeze-out properties can be done by combining the measured source parameters into an effective freeze-out volume $V_{\text{eff}} = 2\pi R_l R_s^2$ [97], assuming a Gaussian shape in transverse direction and a longitudinal length of R_l. Since the HBT radii R_s and R_l do not reflect the physical dimensions of the source this quantity can not be identified as the total source volume. However, since no statements about absolute densities or freeze-out volumes are made the effective freeze-out volume V_{eff} can still be used to compare results at different beam energies and centralities. If freeze-out happens at constant density as proposed in [99], V_{eff} is expected to scale linearly with the charged particle multiplicity. Figure 8.12 shows V_{eff} as a function of the number of participants for the three beam energies 40, 80, and 158 AGeV and for the second $k_\perp$ bin $0.15 < k_\perp < 0.25$ GeV/c. Indeed, an approximately linear scaling with N_{part} is observed at all three energies. This is consistent with the assumption of constant freeze-out density since the number of charged particles was found to scale close to linear with N_{part} at SPS [100, 101].

However, the beam energy dependence of V_{eff} as shown in Fig. 8.12 is surprising: the increase of pion multiplicity by about 50% from 40 AGeV to 158 AGeV is not reflected in a corresponding beam energy dependence of V_{eff}. Obviously, the freeze-out volume scales with multiplicity if multiplicity is controlled via centrality, but it does not scale as multiplicity changes with beam energy. Comparing the freeze-out volumes at different beam energies from AGS to RHIC clarifies the

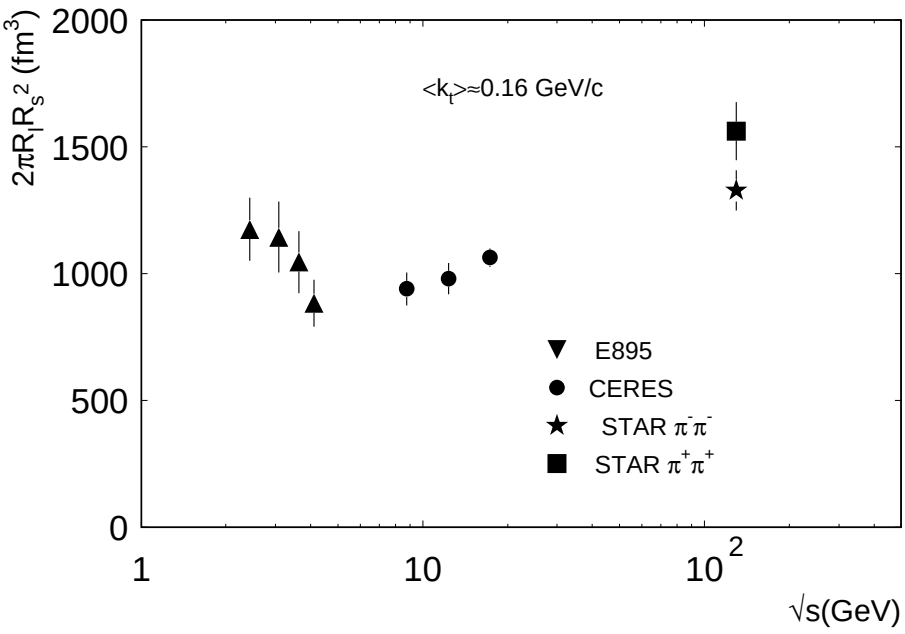

Figure 8.13: The effective volume V_{eff} as a function of $\sqrt{s}$. The data points from the experiment E895 are at a mean transverse pair momentum $\langle k_\perp \rangle = 0.15$ GeV/c [95], STAR is at $\langle k_\perp \rangle = 0.17$ GeV/c [96], and the CERES points are the average of the $k_\perp$ bins at $\langle k_\perp \rangle = 0.12$ GeV/c and $\langle k_\perp \rangle = 0.2$ GeV/c.

situation. As shown in Figure 8.13, the freeze-out volume V_{eff} is gradually decreasing within the AGS energy range, possibly reaching a minimum between AGS and SPS energies, and increases again towards RHIC. This behavior can not be explained by a simple relation between multiplicity and freeze-out volume. The minimum between AGS and SPS energies may indicate the transition from *nucleon dominated* to *pion dominated* freeze-out.

The condition for pion freeze-out is not well understood. Whether it occurs at constant particle density (as proposed by Pomeranchuk [99]) or if the mean free path $\lambda_{\pi\pi}$ is of the same order as the size of the hadronic system (proposed by Stock [102]) is not clear. In the latter case, the freeze-out density explicitely depends on the size of the system and is given as $\rho_f \propto 1/R_f$ while in the former case it does not.

Pion freeze-out determines the point in time at which the last interactions between pions and other particles in the fireball happen. Of course, this condition is influenced by the absolute number of particles in the fireball and the cross section of pions with these particles. For simplicity, only nucleons and pions are considered as constituents of the fireball. To get an estimate for the number of particles, the midrapidity yield of negatively charged pions [103, 104, 105, 106] and protons [71, 107, 108, 109, 110, 111] in central Pb(Au)+Pb(Au) collisions are used. Results for $\mathrm{d}N/\mathrm{d}y_{\text{mid}}$ as a function of $\sqrt{s}$ are shown in Figure 8.14.

At low beam energies, the colliding nuclei are stopped to a high degree, leading to a baryon rich region around midrapidity. With increasing collision energies the colliding nuclei become more transparent, resulting in an almost net-baryon free region around midrapidity (see the yield

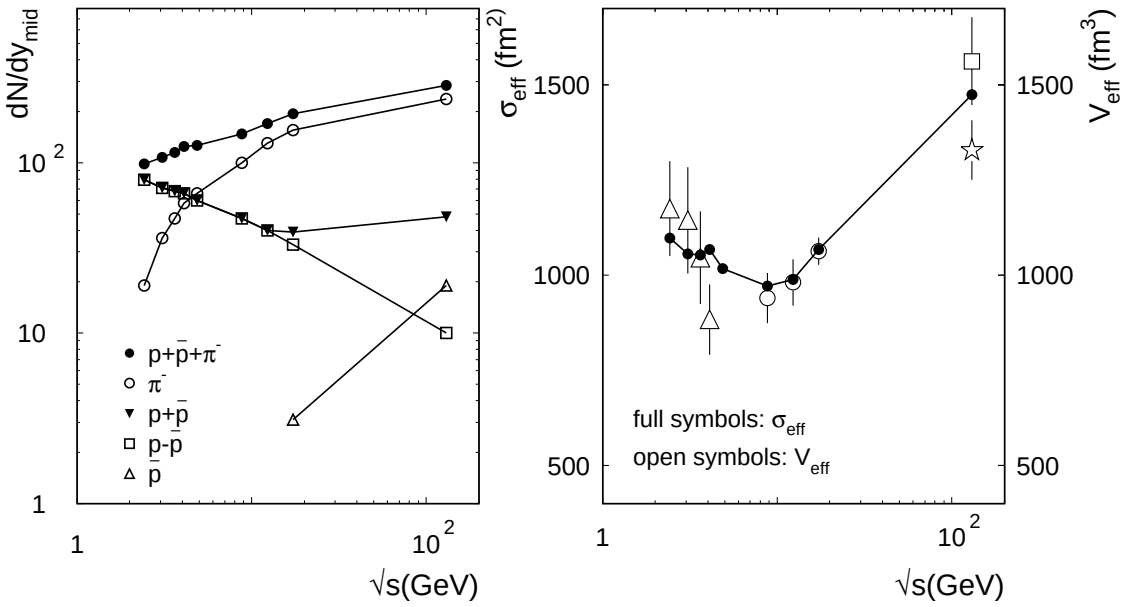

Figure 8.14: Left: Midrapidity yields of protons, anti-protons and negative pions as a function of $\sqrt{s}$. Right: Effective particle number σ_{eff} and effective volume V_{eff} vs. $\sqrt{s}$.

for p-$\bar{\text{p}}$ in Fig. 8.14). However, production of baryons and anti-baryons is rising steeply ($\bar{\text{p}}$ in Fig. 8.14). The total proton yield (p+$\bar{\text{p}}$) at midrapidity drops from AGS to SPS and stays approximately constant between SPS and RHIC because the decreasing number of net protons is compensated by p$\bar{\text{p}}$ production. The pion yield increases monotonically with beam energy. The sum of pions and protons is still a monotonic function of $\sqrt{s}$ and does not reflect the observed minimum in V_{eff}. At this point, the cross sections $\sigma_{\pi\pi}$ and $\sigma_{\pi N}$ have to be considered. To account for the neutrons the number of protons is multiplied by a factor of 2. This factor is correct only for the highest beam energies. For lower beam energies it is used as an approximation. Also the role of light fragments and other produced particles is neglected. The density of negative pions is weighted by a factor of 3 to take the neutral and positive pions into consideration. The cross section weighted sum of pions and nucleons σ_{eff} defined in this way is given by

$$\sigma_{\text{eff}} = 2 \cdot N_{\text{p+}\bar{\text{p}}} \cdot \sigma_{\pi N} + 3 \cdot N_{\pi^-} \cdot \sigma_{\pi\pi} \tag{8.15}$$

and shown in Figure 8.14 in the right panel. For the cross section $\sigma_{\pi\pi} = 12$ mb and $\sigma_{\pi N} = 65$ mb [112] are assumed, neglecting the energy dependence of the cross section. The resulting effective cross section σ_{eff} shows a minimum around lower SPS energies. Consequently, the ratio $V_{\text{eff}}/\sigma_{\text{eff}}$, which has the dimension of a length, is approximately constant (see Fig. 8.14). This results suggests $V_{\text{eff}}/\sigma_{\text{eff}} \approx 1$ fm as a universal freeze-out condition.

With these simple assumptions, the relatively weak beam energy dependence of the HBT radii can be understood as an interplay between the decreasing (and eventually saturating) nucleon plus anti-nucleon yield and the increasing pion multiplicity at midrapidity if the different cross sections with pions are taken into account.

The observed large radii R_s at low beam energies and their steep dependence on $k_\perp$ could be

explained by a more detailed consideration of the pion-nucleon cross section. At low beam energies, where the protons are most important, the strong momentum dependence of $\sigma_{\pi N}$ may affect the $k_\perp$-dependence of R_s. While pions with large momentum (leading to pion pairs with large $k_\perp$) only have a relatively small probability to interact with nucleons, pions with small momentum (small $k_\perp$) are expected to interact with nucleons many times. This may lead to large scattering angles of the pions as they leave the freeze-out volume, leading to correlations between particles emitted from distant regions.

8.4 Summary and Conclusion

The results presented in the context of this thesis allow for a systematic comparison of the transverse momentum dependence of HBT parameters as a function of centrality and beam energy at SPS. The analyzed data have been taken from Pb-Au collisions at the CERN SPS at beam energies of 40, 80, and 158 *A*GeV and were processed in a consistent way, allowing for a direct comparison of the results.

Figure 8.15 compares the results of this thesis with the results obtained by the NA49 experiment for the most central bin. For beam energies of 40 and 80 *A*GeV the radii agree within the errors. Only at 158 *A*GeV the differences in the radii are more pronounced, especially at hight $k_\perp$.

For all three energies an increase of the lifetime τ_f, extracted from the measured longitudinal HBT parameter R_l, with centrality was observed. Furthermore, R_l and with it τ_f increases with beam energy. These results are not very surprising. With increasing beam energy and increasing centrality the energy density deposited in the reaction zone increases as well and the expanding system needs a longer time to reach the condition for freeze-out.

The systematics of R_s are unexpected. Compared to the higher beam energies, $R_s(k_\perp)$ at $E_{\text{beam}} = 40$ *A*GeV is much steeper. The determined transverse source size R_{geo} and the transverse flow velocity $\langle v_\perp \rangle$ for beam energies 80 and 158 *A*GeV show a smooth increase with centrality and only a very weak dependence on the beam energy. R_{geo} at freeze-out is in the order of 5–7 fm, the transverse expansion velocity, obtained with the model described in [78] and assuming a box-shaped transverse source profile and a temperature of $T = 120$ MeV, is between $0.3c$ and $0.6c$. The approximation Eq. (8.4) does not work for the beam energy of 40 *A*GeV. The obtained transverse geometrical radii R_{geo} are between 6 and 12 fm with large error bars. The transverse flow velocity $\langle v_\perp \rangle$ reaches unrealistic large values of up to $0.8c$ at 40 *A*GeV, also with very large error bars. The results could be explained by Fig. 8.10. The χ^2 distribution obtained by fitting parameterization (8.4) to the data shows no pronounced minimum, allowing for large values of R_{geo} and η_f^2/T.

The radius parameter R_o shows a strong decrease with $k_\perp$ at all centralities and beam energies. However, the influence of the momentum resolution of the TPC on R_o is significant , leading to large correction factors and error bars, especially at large values of $k_\perp$. It has been proposed that the existence of a strong first order phase transition and an accordingly long living mixed phase would be observable by a large outward radius R_o compared to R_s, indicating a long duration of pion emission $\Delta\tau$. The analyzed data do not support such a scenario at SPS. All observed HBT radii R_o are similar to R_s at all beam energies and centralities. At 159 *A*GeV the data are consistent with a short but finite emission duration of about 2–3 fm/c.

Studying the freeze-out volume of the collision system leads to some surprising results. At

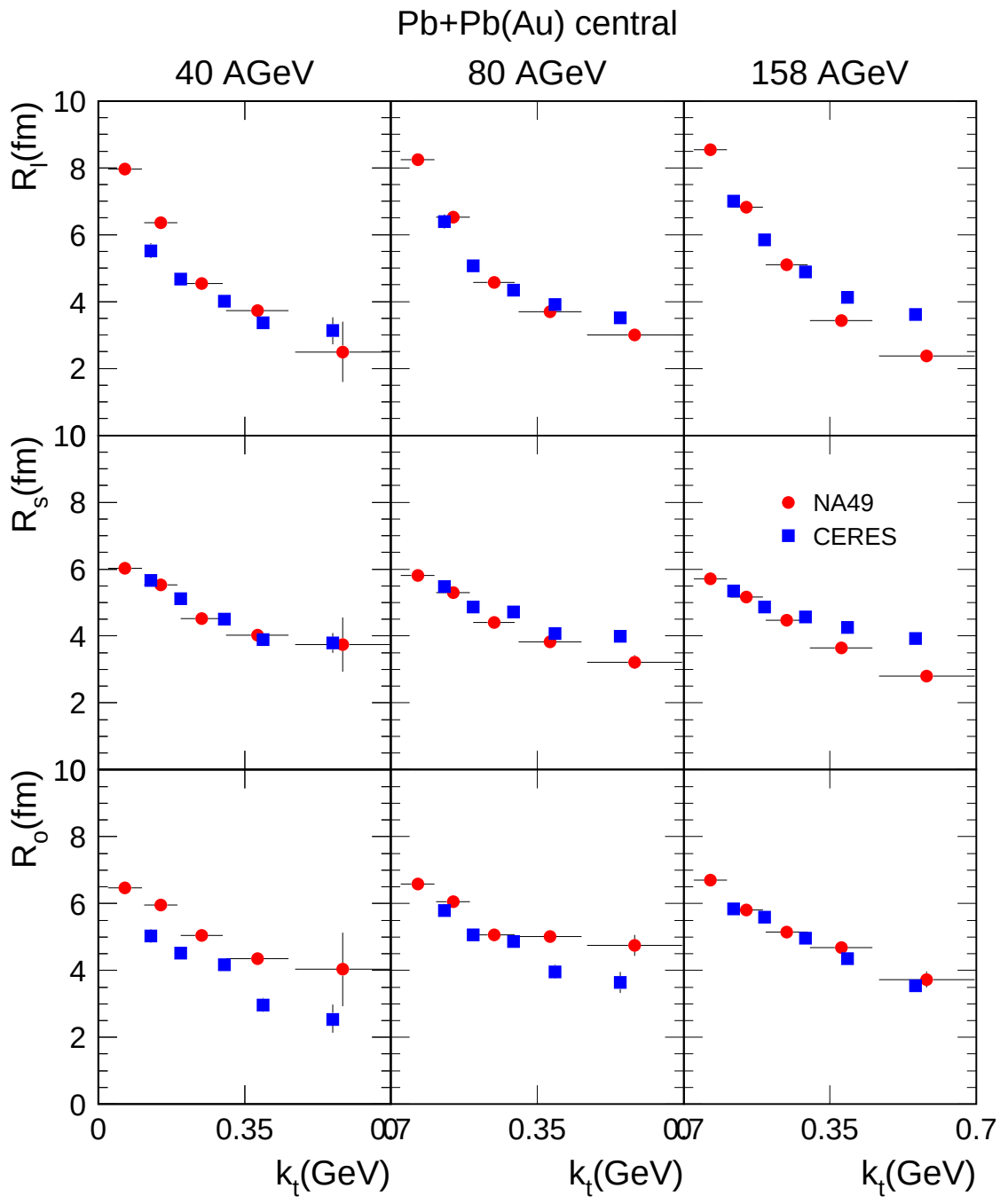

Figure 8.15: Comparison of HBT radii with results from NA49.

all three energies a linear scaling of the volume V_{eff} with N_{part} was observed, consistent with the assumption of a constant freeze-out density. However, no clear beam energy dependence could be observed although the multiplicity increases by about 50% as going from 40 *A*GeV to 158 *A*GeV. The smallest V_{eff} are observed at 40 *A*GeV. This minimum in V_{eff} at lower SPS energies could be

explained by a transition from nucleon to pion dominated freeze-out. As a *universal freeze-out condition* the ratio $V_{\text{eff}}/\sigma_{\text{eff}} \approx 1$ fm (with σ_{eff} being the cross section weighted sum of pions and nucleons) has been identified.

The presented results for $E_{\text{beam}} = 158$ *A*GeV are obtained with a limited sub-sample of the recorded data. The production of these data was done using a preliminary calibration of the detectors. At the beginning of 2002, the effort on improving the resolution of the TPC and the calibration of the detectors was going on with big success. As soon as the work on the detector calibration has converged and the production of the whole data set is done the statistics for the beam energy 158 *A*GeV can be improved substantially. The improved momentum resolution will result in smaller correction factors, thus reducing the systematic errors at large values of $k_{\perp}$.

Bibliography

[1] U. W. Heinz and M. Jacob, *Evidence for a new state of matter: An assessment of the results from the CERN lead beam programme* (2000), nucl-th/0002042.

[2] M. G. Alford, J. Berges, and K. Rajagopal, *Magnetic fields within color superconducting neutron star cores*. Nucl. Phys. **B571**(2000) 269, hep-ph/9910254.

[3] H. Heiselberg, S. Jeon, L. D. McLerran, and H. B. Tang, *Hot Neutron Stars as a Source for Gamma Ray Bursts at Cosmological Distance Scales* (1997), astro-ph/9711169.

[4] T. Maruyama and S. Chiba, *Equation of state of neutron-star matter and the isovector nucleon optical model potential*. J. Phys. **G25**(1999) 2361.

[5] P. Braun-Munzinger and J. Stachel, *Probing the phase boundary between hadronic matter and the quark-gluon-plasma in relativistic heavy ion collisions*. Nucl. Phys. **A606**(1996) 320, nucl-th/9606017.

[6] J. Stachel, *Towards the quark-gluon plasma*. Nucl. Phys. **A654**(1999) 119c, nucl-ex/9903007.

[7] P. Braun-Munzinger, *Towards the quark-gluon plasma*. Nucl. Phys. **A663**(2000) 183, nucl-ex/9909014.

[8] F. Karsch, *Lattice results on QCD thermodynamics*. Nucl. Phys. **A698**(2002) 199, hep-ph/0103314.

[9] F. Karsch, *Lattice QCD at finite temperature and density*. Nucl. Phys. Proc. Suppl. **83**(2000) 14, hep-lat/9909006.

[10] F. Karsch, E. Laermann, and A. Peikert, *The pressure in 2, 2+1 and 3 flavour QCD*. Phys. Lett. **B478**(2000) 447, hep-lat/0002003.

[11] F. Karsch, *Lattice QCD at high temperature and density* (2001), hep-lat/0106019.

[12] W. Busza and A. S. Goldhaber, *Nuclear stopping power*. Phys. Lett. **B139**(1984) 235.

[13] J. D. Bjorken, *Highly relativistic nucleus-nucleus collisions: The central rapidity region*. Phys. Rev. **D27**(1983) 140.

[14] S. Weinberg, *The First Three Minutes*. Basic Books, New York, 1977.

[15] J. Wambach and R. Rapp, *Theoretical interpretations of low-mass dileptons*. Nucl. Phys. **A638**(1998) 171c, nucl-th/9802001.

[16] T. Hatsuda and S. H. Lee, *QCD sum rules for vector mesons in nuclear medium*. Phys. Rev. **C46**(1992) 34.

[17] R. Rapp and J. Wambach, *Chiral symmetry restoration and dileptons in relativistic heavy-ion collisions*. Adv. Nucl. Phys. **25**(2000) 1, hep-ph/9909229.

[18] G. Agakichiev et al. (CERES/NA45), *Enhanced production of low mass electron pairs in 200 GeV/u S - Au collisions at the CERN SPS*. Phys. Rev. Lett. **75**(1995) 1272.

[19] G. Agakichiev et al. (CERES/NA45), *Low-mass e^+e^- pair production in 158 AGeV Pb Au collisions at the CERN SPS, its dependence on multiplicity and transverse momentum*. Phys. Lett. **B422**(1998) 405, nucl-ex/9712008.

[20] B. Lenkeit et al. (CERES/NA45), *Recent results from Pb-Au collisions at 158 GeV/c per nucleon obtained with the CERES spectrometer*. Nucl. Phys. **A661**(1999) 23, nucl-ex/9910015.

[21] G. Agakichiev et al., *Systematic study of low-mass electron pair production in p Be and p Au collisions at 450 GeV/c*. Eur. Phys. J. **C4**(1998) 231.

[22] S. Damjanovic and K. Filimonov (CERES/NA45), *Low-mass lepton pair production in Pb-Au collisions at 40 AGeV* (2001), nucl-ex/0111009.

[23] G. E. Brown and M. Rho, *On the manifestation of chiral symmetry in nuclei and dense nuclear matter* (2001), hep-ph/0103102.

[24] R. Rapp, G. Chanfray, and J. Wambach, *Rho meson propagation and dilepton enhancement in hot hadronic matter*. Nucl. Phys. **A617**(1997) 472, hep-ph/9702210.

[25] W. Schmitz, Λ *Produktion in Pb–Au–Kollisionen bei 40 AGeV*. Ph.D. thesis, Universität Heidelberg, 2001.

[26] D. Groom et al., *Review of Particle Physics*. Eur. Phys. J. **C15**(2000) 1, URL http://pdg.lbl.gov.

[27] R. Hanbury Brown, R. C. Jenson, and M. K. Das Gupta. Nature **170**(1952) 1061.

[28] R. Hanbury Brown and R. Q. Twiss, *Correlations between photons in two coherent beams of light*. Nature **177**(1956) 27.

[29] R. Hanbury Brown and R. Q. Twiss, *A test of a new type of stellar interferometer on Sirius*. Nature **178**(1956) 1046.

[30] E. Purcell. Nature **178**(1956) 1449.

[31] R. J. Glauber (Editor), *Quantum Optics and Electronics*, Les Houches Lecture Notes 1964, Gordon and Breach, 1965.

[32] G. Goldhaber, S. Goldhaber, W.-Y. Lee, and A. Pais, *Influence of Bose-Einstein statistics on the antiproton proton annihilation process*. Phys. Rev. **120**(1960) 300.

[33] U. W. Heinz, *Hanbury-Brown/Twiss interferometry for relativistic heavy- ion collisions: Theoretical aspects* (1996), nucl-th/9609029.

[34] F. B. Yano and S. E. Koonin, *Determining pion source parameters in relativistic heavy ion collisions*. Phys. Lett. **B78**(1978) 556.

[35] S. Chapman, J. R. Nix, and U. W. Heinz, *Extracting source parameters from Gaussian fits to two particle correlations*. Phys. Rev. **C52**(1995) 2694, nucl-th/9505032.

[36] T. Csörgő and B. Lörstad, *Bose-Einstein correlations for expanding finite systems*. Nucl. Phys. **A590**(1995) 465c, hep-ph/9503494.

[37] U. A. Wiedemann and U. W. Heinz, *Particle interferometry for relativistic heavy-ion collisions*. Phys. Rept. **319**(1999) 145, nucl-th/9901094.

[38] A. N. Makhlin and Y. M. Sinyukov, *The hydrodynamics of hadron matter under a pion interferometric microscope*. Z. Phys. **C39**(1988) 69.

[39] Y. M. Sinyukov, *Hanbury Brown/Twiss correlations for expanding hadron and quark-gluon matter*. Nucl. Phys. **A498**(1989) 151c.

[40] G. F. Bertsch, *Pion interferometry as a probe of the plasma*. Nucl. Phys. **A498**(1989) 173c.

[41] S. Pratt, *Pion interferometry of quark - gluon plasma*. Phys. Rev. **D33**(1986) 1314.

[42] M. Podgoretski. Yad. Fiz. **37**(1983) 272.

[43] Y. F. Wu, U. W. Heinz, B. Tomasik, and U. A. Wiedemann, *Yano-Koonin-Podgoretskii parametrisation of the HBT correlator: A numerical study*. Eur. Phys. J. **C1**(1998) 599, nucl-th/9607044.

[44] U. W. Heinz, B. Tomasik, U. A. Wiedemann, and Y. F. Wu, *Lifetimes and Sizes from Two-Particle Correlation Functions*. Phys. Lett. **B382**(1996) 181, nucl-th/9603011.

[45] M. G. Bowler, *Extended sources, final state interactions and Bose-Einstein correlations*. Z. Phys. **C39**(1988) 81.

[46] G. Baym and P. Braun-Munzinger, *Physics of Coulomb corrections in Hanbury-Brown-Twiss interferometry in ultrarelativistic heavy ion collisions*. Nucl. Phys. **A610**(1996) 286c, nucl-th/9606055.

[47] M. Gyulassy and S. K. Kauffmann, *Coulomb Effects in Relativistic Nuclear Collisions*. Nucl. Phys. **A362**(1981) 503.

[48] D. A. Brown and P. Danielewicz, *Optimized Discretization of Sources Imaged in Heavy-Ion Reactions*. Phys. Rev. **C57**(1998) 2474, nucl-th/9712066.

[49] G. Baym, *The physics of Hanbury Brown-Twiss intensity interferometry: From stars to nuclear collisions*. Acta Phys. Polon. **B29**(1998) 1839, nucl-th/9804026.

[50] H. Appelshäuser et al. (NA49), *Hadronic expansion dynamics in central Pb+Pb collisions at 158 GeV per nucleon*. Eur. Phys. J. **C2**(1998) 661, hep-ex/9711024.

[51] T. Alber et al. (NA35), *A new Coulomb correction method for Bose-Einstein correlations, based on the $\pi + \pi$-correlation measurements*. Z. Phys. **C73**(1997) 443.

[52] P. Braun-Munzinger, private communication.

[53] H. Appelshäuser, *Zweiteilchenkorrelationen in zentralen Blei-Blei-Reaktionen bei 158 GeV pro Nukleon*. Ph.D. thesis, Universität Frankfurt am Main, 1997.

[54] E. Gatti and P. Rehak, *Semiconductor drift chamber - an application of a novel charge transport scheme*. Nucl. Instrum. Meth. **A225**(1984) 608.

[55] O. Nix, *Einsatz und Lasertest von 4" Siliziumdriftdetektoren*. Diploma thesis, Universität Heidelberg, 1996.

[56] J. Seguinot and T. Ypsilantis. Nucl. Instr. and Methods (1977), 142.

[57] D. R. Nygren and J. N. Marx, *The time projection chamber*. Phys. Today **31N10**(1978) 46.

[58] G. Agakichiev et al., *Study of electron pair and photon production in Pb-Au collisions at the CERN SPS; Addendum to proposal SPSLC/P280.*. CERN/SPSLC **96-35**(1996).

[59] G. Agakichiev et al., *Technical Note on the NA45/CERES Upgrade*. CERN/SPSLC **96-50**(1996).

[60] F. Sauli, *Principles of operation of multiwire proportional and drift chambers*. CERN 77-09, 1977.

[61] K. Kleinknecht, *Detektoren für Teilchenstrahlung*. Teubner Studienbücher, Stuttgart, 1992.

[62] M. Huk, P. Igo-Kemenes, and A. Wagner, *Electron Attachment to Oxygen, Water, and Methanol, in Various Drift Chamber Gas Mixtures*. Nucl. Instrum. Meth. **A267**(1988) 107.

[63] B. Yu et al., *Investigation of chevron cathode pads for position encoding in very high rate, gas proportional chambers*. IEEE Trans. Nuc. Sc. **38**(1991), 2 454.

[64] W. Schmitz, *Cathode pad design for the CERES-TPC*. CERES internal note (1998).

[65] W. Blum and W. Rolandi, *Particle Detection with Drift Chambers*. Springer-Verlag, Heidelberg, 1994.

[66] P. Braun-Munzinger, D. Miskowiec, and P. Zimmermann, *Laser calibration system for the CERES TPC*. In *GSI Scientific Report*, Gesellschaft für Schwerionenforschung (GSI), 1998, page 192.

[67] P. Fischer, *Die Padauslese des CERES-Experiments*. Ph.D. thesis, Universität Heidelberg, 1992.

[68] R. Baur, P. Ernst, G. Gramegna, and M. Richter, *Front-end electronics for the CERES TPC-detector*. Nucl. Instrum. Meth. **A409**(1998) 278.

[69] S. Klein et al. In *Proc. of the First Workshop on Electronics for LHC Experiments*, 1995, page 93.

[70] L. Musa et al., *Front-End Electronics for the ALICE TPC-Detector*. In *Proc. of the 4th Workshop on Electronics for LHC Experiments*, Rome, 1998.

[71] D. Adamova et al. (CERES/NA45), *New results from CERES*. Nucl. Phys. **A698**(2002) 253c.

[72] J. P. Baud et al., *User Guide for CASTOR*. http://cern.ch/it-div-ds/HSM/CASTOR/DOCUMENTATION/USERGUIDE/userguide.html, 2002, european Laboratory for Particle Physics (CERN).

[73] W. Ludolphs. Ph.D. thesis, Universität Heidelberg, in preparation.

[74] S. Iourevich. Ph.D. thesis, Universität Heidelberg, in preparation.

[75] CERN, Geneva, *GEANT manual*. 1993, CERN Program library long writeup W5013.

[76] R. K. Bock et al., *Data Analysis Techniques for High-Energy Physics Experiments*. Cambridge University Press, Cambridge, 1995.

[77] R. L. Gluckstern, *Uncertainties in track momentum and direction, due to multiple scattering and measurement errors*. Nucl. Instrum. Meth. **24**(1963) 381.

[78] B. Tomasik, U. A. Wiedemann, and U. W. Heinz, *Reconstructing the freeze-out state in Pb+Pb collisions at 158 AGeV/c* (1999), `nucl-th/9907096`.

[79] D. Miskowiec and H. Sako, private communication.

[80] K. J. Eskola, R. Vogt, and X. N. Wang, *Nuclear Overlap Functions*. Int. J. Mod. Phys. **A10**(1995) 3087.

[81] M. Deutschmann et al. (Aachen-Berlin-Bonn-CERN-Cracow-London-Vienna-Warsaw), *A study of second-order interference for pions produced in various hadronic interactions*. Nucl. Phys. **B204**(1982) 333.

[82] H. Appelshäuser, private communication.

[83] S. Chapman, P. Scotto, and U. W. Heinz, *Model independent features of the two-particle correlation function*. Heavy Ion Phys. **1**(1995) 1, `hep-ph/9409349`.

[84] U. A. Wiedemann, P. Scotto, and U. W. Heinz, *Transverse momentum dependence of Hanbury-Brown-Twiss correlation radii*. Phys. Rev. **C53**(1996) 918, `nucl-th/9508040`.

[85] R. Scheibl and U. W. Heinz, *Coalescence and flow in ultra-relativistic heavy ion collisions*. Phys. Rev. **C59**(1999) 1585, `nucl-th/9809092`.

[86] G. Bertsch, M. Gong, and M. Tohyama, *Pion interferometry in ultrarelativistic heavy ion collisions*. Phys. Rev. **C37**(1988) 1896.

[87] D. Kusnezov and G. Bertsch, *Transverse hydrodynamics of collective pion flow*. Phys. Rev. **C40**(1989) 2075.

[88] S. Chapman, P. Scotto, and U. W. Heinz, *A new cross term in the two particle HBT correlation function*. Phys. Rev. Lett. **74**(1995) 4400, `hep-ph/9408207`.

[89] T. Alber. Ph.D. thesis, Universität München, 1995.

[90] E. Schnedermann, J. Sollfrank, and U. W. Heinz, *Thermal phenomenology of hadrons from 200 A/GeV S+S collisions*. Phys. Rev. **C48**(1993) 2462, `nucl-th/9307020`.

[91] K. S. Lee, U. W. Heinz, and E. Schnedermann, *Search for collective transverse flow using particle transverse momentum spectra in relativistic heavy ion collisions*. Z. Phys. **C48**(1990) 525.

[92] T. Csörgő and B. Lörstad, *Bose-Einstein Correlations for Three-Dimensionally Expanding, Cylindrically Symmetric, Finite Systems*. Phys. Rev. **C54**(1996) 1390, `hep-ph/9509213`.

[93] N. Xu et al. (NA44), *Hadron distributions: Recent results from the CERN experiment NA44*. Nucl. Phys. **A610**(1996) 175c.

[94] U. A. Wiedemann, *Space-time analysis: HBT at SPS and RHIC*. Nucl. Phys. **A661**(1999) 65c, `nucl-th/9907048`.

[95] M. A. Lisa et al. (E895). Phys. Rev. Lett. **84**(2000) 2798.

[96] C. Adler et al. (STAR), *Pion interferometry of* $\sqrt{s(NN)} = 130$ *gev Au+Au collisions at RHIC*. Phys. Rev. Lett. **87**(2001) 082301, `nucl-ex/0107008`.

[97] H. Appelshäuser, *Pion interferometry: Recent results from SPS*. In *International Workshop on Gross Properties of Nuclei and Nuclear Excitation: Ultrarelativistic Heavy Ion Collisions*, Hirschegg, 2002, page 188, `hep-ph/0204159`.

[98] N. Xu and M. Kaneta, *Hadron freeze-out conditions in high energy nuclear collisions*. Nucl. Phys. **A698**(2002) 306, `nucl-ex/0104021`.

[99] I. Pomeranchuk. Dokl. Akad. Nauk SSSR **78**(1951) 884.

[100] M. M. Aggarwal et al. (WA98), *Scaling of particle and transverse energy production in* $^{208}Pb+^{208}Pb$ *collisions at 158 AGeV*. Eur. Phys. J. **C18**(2001) 651, `nucl-ex/0008004`.

[101] D. Miskowiec (CERES/NA45), *New results from CERES*. Proceedings to CIPPQG Palaiseau (2001).

[102] R. Stock, *Pion interferometry in high-energy hadron and nuclear collisions: Radial expansion and freezeout*. Annalen der Physik **48**(1991) 195.

[103] M. Gazdzicki. In *International Workshop XXX on Gross Properties of Nuclei and Nuclear Excitations*, Hirschegg, 2002.

[104] J. L. Klay et al., publication in preparation.

[105] C. Adler et al. (STAR), *Multiplicity distribution and spectra of negatively charged hadrons in Au + Au collisions at* $\sqrt{s(NN)} = 130$ *GeV*. Phys. Rev. Lett. **87**(2001) 112303, nucl-ex/0106004.

[106] C. Adler et al. (STAR), *Results from the STAR experiment*. Nucl. Phys. **A698**(2002) 64.

[107] B. B. Back et al. (E917), *Baryon rapidity loss in relativistic Au+Au collisions*. Phys. Rev. Lett. **86**(2001) 1970, nucl-ex/0003007.

[108] H. Appelshäuser et al. (NA49), *Baryon stopping and charged particle distributions in central Pb+Pb collisions at 158 GeV per nucleon*. Phys. Rev. Lett. **82**(1999) 2471, nucl-ex/9810014.

[109] G. I. Veres (NA49), *Antiproton production in nuclear collisions at 158 AGeV/c*. Nucl. Phys. **A661**(1999) 383.

[110] C. Adler (STAR), *Mid-rapidity anti-proton to proton ratio from Au+Au collisions at* $\sqrt{s(NN)} = 130$ *GeV*. Phys. Rev. Lett. **86**(2001) 4778, nucl-ex/0104022.

[111] J. L. Klay et al. (E895), *Longitudinal Flow of Protons from 2-8 AGeV Central Au+Au Collisions*. Phys. Rev. Lett. **88**(2002) 102301.

[112] J. Stachel et al. (E814), *Particle spectra and correlations from experiment 814*. Nucl. Phys. **A566**(1994) 183c.

Danksagung

An dieser Stelle möchte ich die Gelegenheit nutzen, mich bei den vielen Menschen, die zum Gelingen dieser Arbeit beigetragen haben, zu bedanken.

An erster Stelle bedanke ich mich bei Frau Prof. Johanna Stachel für die Betreuung der Arbeit. Sie ermöglichte mir vielfältige Einblicke in das weite Feld der Schwerionenphysik, angefangen bei der Entwicklung der Ausleseelektronik der TPC, bis hin zur Analyse der Daten. Auch für ihr Vertrauen, das sie vor allem während der Vorbereitung der Strahlzeit im Jahr 2000 mir entgegengebracht hat, möchte ich ihr danken.

Herrn Prof. Knöpfle danke ich, dass er sich als Zweitgutachter zur Verfügung stellte.

Eine ganz wesentlicher Beitrag zu dieser Arbeit kam von Dr. Harald Appelshäuser. Er hatte immer die richtigen Ideen zur richtigen Zeit. Er hat mich dadurch immer wieder vorangebracht, auch wenn es manchmal sehr hoffnungslos aussah.

Dr. Hannes Wessels danke ich für das Korrekturlesen der Arbeit und für die stetige Hilfe beim Kampf mit den Computern. Dank gebührt auch Prof. Peter Glässel und Dr. Ana Marin, die immer ein offenes Ohr für mich hatten und auf deren Hilfe ich stets bauen konnte.

Für das anregende Arbeitsklima und die vielen aufmunternden Worte möchte ich mich auch bei meinen Kolleginnen und Kollegen Hans-Kristian Soltveit, Wolfgang Schmitz, Jana Slivova, Gunar Hering, Sanja Damjanovic, Serguei Yurevich, Jovan Milosevic, Voitech Petracek, Wilrid Ludolphs, Markus Merschmeyer und Marc Stockmeier bedanken. Michael Richter und Wolfgang Seipp danke ich für die Einweihung in die Geheimnisse der Ausleseelektronik.

Auch den Kollegen der GSI und allen anderen Kollaborationsmitglieder, besonders Dariusz Miskowiec, mit dem ich eine interessante und lehrreiche Zeit am CERN verbringen durfte, bin ich dankbar verbunden.

Schließlich möchte ich mich auch bei meiner Freundin Maria bedanken. Ich bin sicher, sie freut sich mindestens genauso wie ich über die Fertigstellung der Arbeit.

Zu guter letzt bedanke ich mich ganz herzlich bei meinen Eltern dafür, dass sie mir durch ihre Unterstützung über viele Jahre hinweg meine Ausbildung erst ermöglicht haben.

The CERES Collaboration

P. Rehak
Brookhaven National Laboratory, Upton, USA

B. Lenkeit, A. Pfeiffer, J. Schukraft
CERN, Geneva, Switzerland

G. Agakichiev, P. Braun-Munzinger, C. Garabatos, G. Hering, J. Holeczek, A. Maas, A. Marin, D. Miskowiec, J. Rak, H. Sako, S. Sedykh
GSI, Darmstadt, Germany

V. Belaga, K. Fomenko, Y. Panebrattsev, O. Petchenova, S. Shimansky, V. Yurevich
JINR, Dubna, Russia

J. P. Wurm
Max-Planck-Institut für Kernphysik, Heidelberg, Germany

H. Appelshäuser, S. Damjanovic, T. Dietel, L. Dietrich, S. I. Esumi, K. Filimonov, P. Glässel, W. Ludolphs, J. Milosevic, V. Petracek, M. Richter, W. Schmitz, W. Seipp, J. Slivova, H. J. Specht, J. Stachel, H. Tilsner, J. P. Wessels, T. Wienold, B. Windelband, S. Yurevich
Universität Heidelberg, Germany

D. Adamova, V. Kushpil, M. Sumbera
NPI/ASCR, Rez, Czech Republic

A. Drees, F. Ceretto
Department for Physics and Astronomy, SUNY Stony Brook, USA

A. Cherlin, Z. Fraenkel, A. Gnaenski, A. Milov, I. Ravinovich, I. Tserruya, W. Xie
Weizmann Institute, Rehovot, Israel